Image Processing Algorithms for Improved Medical Diagnosis

A Thesis

Submitted for the Degree of

Doctor of Philosophy

in the Faculty of Engineering

by

K. N. Bhanu Prakash

Department of Electrical Engineering
Indian Institute of Science
Bangalore – 560 012

JULY 2001

Dedicated

to the magnanimous,

who enrich others' lives

and go unrecognized.

अजीब दास्तां है ये
कहाँ शुरू कहाँ खतम
ये मन्ज़िलें है कौन सी
न वो समझ सके न हम

– Shailendra

Yet all experience is an arch wherethro'
gleams that untravelled world whose margin fades
for ever and ever when I move.

– Tennyson

Acknowledgments

I wish to express my sincere gratitude to my research supervisor, Dr. A. G. Ramakrishnan, whose helping hand was present at every step in this endeavour. His unbounded enthusiasm for work was infectious and enabled me to undertake and complete the work that entailed. Many a discussion, conducted in a friendly informal manner not only clarified the subject-matter but also made working on this thesis a pleasure.

I am deeply indebted to Dr. S. Suresh, Director, Mediscan Systems, Chennai and Dr Teresa Chow of University hospital of Malaya, Kuala Lumpur, Malaysia, who have helped us in the acquisition of fetal image data and analysis of the results. Dr Suresh and his team have extended unstinted support during the entire study.

My sincere thanks are due to Prof. P. N. Jayakumar, Head of Interventional Radiology, NIMHANS, Bangalore, for the MRI data. His valuable suggestions and guidance, given with warmth and love, has helped me throughout the study. In spite of his busy schedule, he was always available for us and his commitment to society's welfare was a source of inspiration in our endeavour.

I would like to acknowledge Mrs.G. Sita for her moral support and encouragement during my course of stay. Her valuable suggestions helped me understand the realities of life. My discussions with her were always beneficial.

My profound thanks to The Principal, SJCE, and Staff of Department of Instrumentation Technology, for their support and co-operation during the entire period of my study. I would like to thank Prof. M. L. Dwarakanath, Head of E&C, for his encouragement.

I express my sincere thanks to Prof. Madhukar Pandit, University of Kaiserslautern, Germany for his support during my stay at Germany. My friend M. N. Ramesh has helped me in many walks of life. My loving thanks to him and his family members.

My heartfelt thanks to Prof. M. N. Narasimhamurthy, Prof. Sathiya Keerthi, Dr R. Sathyanarayana, Dr Ashok Rao, Dr T. N. Nagabhushan, Dr Narendranath Udupa, Dr Suresh and Dr Pandian, for their help and support. My stay here was rendered more meaningful and enjoyable by G. K. Purushothama, Peeta Basa Pati, K. A. Radhakrishna Rao, Dr. D. Ravi and N. Rishikesh. Their constant support and encouragement enabled me complete

my endeavour.

I will be failing in my duty if I don't acknowledge the support extended by my young friends Dhanya, Harishri, Venkatesh, Raju, Vijaykrishna, Muralishankar, Jayavardhana Rama, Aparna, Prathiba, Aruna, Meera and Harish. The environment created by them in the lab was electrifying.

Sincere thanks are due to Dr B. N. Gangadhar for his help in data collection and to Dr Subbakrishna of NIMHANS for his suggestions and guidance in statistical analysis.

Words cannot adequately convey the support extended by my family members at all the stages of my study. Very special thanks to all of them for their love and encouragement which empowered me to come out of difficult times.

K. N. Bhanu Prakash

Abstract

The thesis addresses two different issues in medical image processing:

1. Study of sonogram textural features for fetal lung maturity prediction.

2. Enhancement and Segmentation of Magnetic Resonance Brain Images.

The assessment of fetal lung maturity is of great value in perinatal management. Currently used methods involving biochemical tests are invasive and on occasions, contraindicated. The other methods based on physical measurements have varying degrees of success. However, it is reasonable to assume that both morphological and biochemical changes alter the ultrasound propagation properties and diffuse scattering of fetal lung. This may in turn change the textural appearance of sonogram. The above reasons motivated us to conduct a pilot study to investigate the feasibility of predicting the fetal lung maturity using the textural features of the sonograms.

Data were collected from 350 pregnant women at intervals of 2 weeks from the gestation age (GA) of 24 to 38 weeks. Images were acquired from two clinical centers under similar settings. Only the data corresponding to normal pregnancies, which led to babies with normal pulmonary functions, were included in our analysis.

A region of interest of 64×64 pixels was analyzed from the fetal lung and liver images. The images were first normalized. Various textural features of these images were then computed, using co-occurrence matrix, gray level difference matrix, Laws' textural masks and fractal analysis. The ratios of lung to liver feature values were investigated as possible indices for classifying the images into those from mature (reduced pulmonary risk) and immature (possible pulmonary risk) lung. Each feature was evaluated for its

computational complexity and correlation with respect to GA. The features selected to be used for the actual classification were: fractal dimension, lacunarity and features derived from the histograms of the images. A number of classifiers were independently used to classify the images as belonging to mature or immature class: Nearest-Neighbour (NN), k-Nearest Neighbour (k-NN), Weighted k-NN, Multilayer Perceptron, Radial basis function network and Support Vector Machines. The obtained classification accuracy of 73% to 96% is encouraging. To the best of author's knowledge, this is the first ever attempt to assess pulmonary risk using textural features of the ultrasound.

Magnetic Resonance Imaging (MRI) is extensively used in the study of brain. Segmentation of MRI brain images is necessary for a number of clinical investigations of varying complexity. Manual segmentation is tedious, time consuming and subjective. Hence, we have addressed the issue of automated segmentation of the MR brain images. More than 150 T1- and T2-weighted, spin echo images were taken from the routine scans of a national medical institute. Some of the images were of low contrast. We enhanced them using two different approaches. In the first approach, we made use of the entropy relations proposed by Shannon and Renyi. In the second approach, where a 3^{rd} degree polynomial was used for enhancement, the range of gray scale to be enhanced could be selected. The polynomial based enhancement has given very good results for both T1- and T2-weighted images without the need for manual parameter tuning. Results of initial experiments on some sample x-ray CT images have shown the promise of the proposed enhancement techniques also for other medical imaging modalities.

Combinations of the above enhancement methods with different segmentation techniques were tried. A 3-Gaussian mixture model was used to represent white matter, gray matter and cerebrospinal fluid. The model parameters were estimated using the Expectation - Maximization algorithm (EM). Convergence of the EM algorithm was enhanced by selecting the initial parameters using Vector Quantization, k-means and Fuzzy c-means, instead of adopting random selection. Polynomial enhancement has led to good results with all the segmentation methods used. Results of segmentation have been validated by the neuroradiologists.

Contents

List of Figures

List of Tables

Chapter 1

Introduction

Image processing is a rapidly evolving field with a broad spectrum of applications, such as remote sensing, image transmission, medical image processing, RADAR, SONAR, and automated inspection of industrial parts. Computer processing and analysis of medical images covers a number of areas including acquisition, image formation/reconstruction, enhancement, compression and storage, analysis and image-based visualization. The development of medical image analysis over the last 20 years can be studied in four time frames [34]:

- pre-1980 to 1984, which could be termed as the era of 2D image analysis,
- 1985-1991, when knowledge-based strategies came to the forefront and the advent of Magnetic Resonance Imaging changed the landscape,
- 1992-1998, when the analysis of 3D images became a key goal and more mathematical-model-driven approaches became computationally feasible, and
- 1999 and beyond, where advanced imaging and computing technology is facilitating work in image guided procedures and more realistic visualizations.

In pre-1980 to 1984 era, the term *medical image analysis* was not very commonly used. There were works reported in 1) enhancement and reconstruction, 2) development of specialized image processing hardware, and 3) image segmentation, feature extraction and

structural/statistical pattern recognition. Efforts on segmentation in this time frame were aimed at detecting contrast edges from 2D image datasets. In terms of image matching or registration, the most prominent application area was digital subtraction angiography.

The mid-to-late 1980s was a transition time for the field. During this phase, prominent areas in which work was carried out are 1) computer aided diagnosis, 2) image segmentation, 3) image registration/matching, and 4) motion analysis. Issues related to both general and object-specific segmentation continued to be studied during this time. Boundary finding and intensity-based region growing were considered. The popular areas were cardiac image analysis, MR image segmentation and ultrasound image analysis, including motion analysis of echocardiographic image sequences.

The types of problems addressed in the early part of the 1990s were influenced by the explosion of accessible image data. The developmental areas were 1) integration of functional and anatomical information from a variety of sources (e.g., MRI and SPECT/PET), 2) pooling data within patient groups and 3) comparing information across different subject populations. Many of these problems required segmentation of subtle structures. Robust, context-based decision making, in the presence of constraints, was the key information processing problem solved during this period.

In the fourth time phase, medical image analysis is still an active area of research with many encouraging results, but also with a number of difficult problems yet to be addressed. A variety of commercial medical imaging equipment comes loaded with simple forms of image processing and analysis algorithms. These range from basic thresholding to semiautomated forms of active contour algorithms.

The focus of the present day studies is in terms of addressing the practical needs of the user community (physicians and biomedical scientists). The work in general must be developed and clearly motivated from the underlying biological problems that are being addressed. Many of these problems require the analysis of not only normal structure and function, but also different abnormal, pathological or disease states. The analysis and processing strategies that are proposed must be put more in touch with image acquisition strategies. MRI research is the most likely candidate for this. One of the challenges

for the field of medical image analysis is the development of appropriate validation and evaluation approaches. This is a critical issue in terms of all practical and theoretical development.

In our work, we have addressed two different issues in medical image processing:

1. An investigation into the feasibility of fetal lung maturity prediction using sonogram textural features.

2. Enhancement and segmentation of magnetic resonance brain images.

The first topic is aimed at developing a method to quantitatively assess echo-texture and exploring the relationship between the change in textural properties and the gestation age. The lung maturity is currently evaluated by various invasive and non-invasive methods. Though a variety of methods are available, amniocentesis, an invasive biochemical procedure, is widely used. In our work, we have computed a set of textural features from the sonogram images of fetal lung and liver, and used it to classify the fetal lung as belonging to one of different pulmonary risk groups.

In the second part of the thesis, we address the problem of enhancement of low contrast magnetic resonance (MR) images. This improves their visual quality and aids in diagnosis. Further, we have also dealt with the problem of segmentation of MR images of the brain into different tissue regions. This helps neuroradiologists to automatically segment the brain image for quantitative assessment of different tissues, avoiding the tedious, subjective and time consuming manual segmentation.

In both the issues, our concern was to provide the medical community with tools that help them in diagnosis. The nature of work and the kind of images we have handled have been constrained by the availability with, and the clinical needs of our medical collaborators.

1.1 Organization of the Thesis

Chapter-2 gives a brief introduction to fetal lung development, literature survey in the area of fetal lung maturity analysis and the motivation for our work.

In chapter-3, we present various textural features based on co-occurrence matrix, gray level difference matrix, Laws' textural masks, fractal theory and histogram. These features are used in our work to quantitatively characterize the fetal lung and liver tissues. A brief discussion on the classifiers used, such as, nearest-neighbour, k-nearest neighbour, weighted k-nearest neighbour, multilayer perceptron, radial basis function and support vector machine is presented.

Details of fetal image data collection, evaluation of textural features, and their classification into high risk, transition and low pulmonary risk groups are given. A detailed discussion on results and analysis is presented at the end of the chapter. The chapter concludes with our contributions and suggestions for future work.

Chapter-4 presents an introduction to magnetic resonance imaging, basics of image segmentation, medical image segmentation, literature survey and motivation for our work. Since we have aimed at enhancement and segmentation, we do not cover the literature in the areas of active contour modeling, RF inhomogeneity correction, feature selection and feature extraction.

We have proposed three methods for enhancing MR images, based on entropy measures and polynomial transformation in chapter-5. Results obtained using the proposed methods and their evaluation by radiologists are also presented. Chapter 5 also discusses the issues in automatic segmentation of brain images and the methods used in our work. A gaussian mixture model (GMM) was used to model the different tissues in the brain. The model parameters were evaluated using the expectation-maximization algorithm (EMA). Using the model, brain tissue was grouped into 3 classes, gray, white matter and cerebrospinal fluid. The EMA was modified to achieve faster convergence. The results of GMM based segmentation were compared with those obtained by fuzzy c-means. Segmentation was attempted on the enhanced images also. Segmentation of the polynomial enhanced images has led to better results than with the other methods.

Chapter-6 gives a comprehensive report on the contributions of the thesis, and gives pointers towards possible future work in the areas addressed.

Chapter 2

Fetal Lung Maturity and its Analysis

2.1 Introduction to Ultrasound Imaging

Medical Ultrasound has become an important and widely accepted means for non-invasive imaging of the human body. Studies in a wide range of clinical settings have shown it to be an accurate and versatile technique yielding cross-sectional tomographic images with little risk or discomfort to the subject and with reasonable resolution. The important features of this modality are its ability to produce real-time images of moving structures, low or no discomfort and low cost.

An A-mode display or A-scan, is one in which the deflection on the screen is proportional to the acoustic energy reflected at tissue interfaces and at inhomogeneities. The amount of reflected energy at any interface depends on the mismatch in acoustic impedances and on the size and shape of the reflecting structures. The reflected echoes are received by the transducer and they are converted to an electrical signal which is called Radio-Frequency (RF) signal. The amplitude of the signal, obtained by demodulation of the RF signal, can be plotted against time. If the speed of sound is assumed to be constant, the time axis corresponds to the depth of penetration of the sound wave. In this way, an one-dimensional A(mplitude)- mode image is created where the positions and the echo strengths of the reflecting structures are imaged along the axis of the transducer.

B-mode imaging, also known as B(rightness)- mode, solves the disadvantage of A-mode

imaging; it does not present a geometric overview of the investigated body structures. Here, the echo amplitudes are used to modulate the image intensity. A two dimensional image is created by linearly translating the transducer in a direction perpendicular to the direction of the acoustical wave (i.e. in lateral direction), and displaying the successive scan lines in parallel. Each scan line corresponds to one position of the sound beam and one acoustic pulse of the transducer. The received RF signal's envelope is detected and its amplitude is represented as the pixel's intensity.

The wavelengths of ultrasound in biological tissues are in the sub-millimeter range. The consequence of this wavelength range is that echos are not only caused by pure specular reflections, but also by diffuse scattering. Besides the anatomical outlining of larger organs and other structures, the images will also contain information about the fine structure of the parenchymal tissues. Diffuse scattering is responsible for the gray shaded texture observed in solid tissues or semi-solid structures. Specular reflections are responsible for the bright boundary interfaces between structures.

Ultrasonic Tissue Characterization : Ultrasonic tissue characterization is defined as the collection of all techniques that extract the medically significant features from an interrogating ultrasonic wave and display tissue signatures appropriate for a differential diagnosis or some other medical purpose. To be useful, such ultrasonic signatures or measures must be related to tissue pathology or physiology.

Tissue characterization is broad in scope and in certain cases, can include aspects of both qualitative and quantitative imaging. Tissue characterization merely involves a re-display or recombination of pulse-echo image information in a way that is more pathology specific.

Qualitative Imaging : Conventional pulse-echo imaging maps, at least to some degree, the location of the scattering structure and the reflecting interfaces. However, it provides little or no information concerning the nature of the reflector. The typical pulse echo image is an intensity map, devoid of phase or spectral information, with brightness related only very crudely to scatter strength.

All conventional ultrasound systems are qualitative in nature. However, many non-conventional techniques are qualitative too, because they also produce a non-quantitative image based on an information content other than the echo intensity. Such qualitative imaging schemes include

- methods that incorporate spectral information into a B-Mode format, such as spectracolor ultrasonography and the so-called dual-frequency scanning.
- methods that incorporate phase information into a B-Mode format.
- various novel techniques for interrogating tissue and receiving the echo waveform.

All these methods, regardless of their information content or display technique, produce qualitative images, that is, images in which no single parameter is recorded in a quantitative fashion.

Quantitative Imaging : Quantitative imaging refers to those techniques that map the distribution and strength of a single ultrasound/tissue interaction parameter in a truly quantitative way. These methods are largely experimental. Two major approaches to quantitative imaging are transmission imaging and scatter imaging.

Ultrasound computerized tomography utilizes the transmitted ultrasound waveform, and generates both attenuation and velocity maps of tissue. The velocity images are produced by using time-of-flight measurements in the reconstruction process, while attenuation images are produced by utilizing measurements of the amplitude of the transmitted signal. The scatter imaging employs the scattered signal to produce quantitative maps of tissue interaction parameters. All scatter-imaging methods are related to classical inverse scattering techniques. Some of these are diffraction tomography, impediography and wave extrapolation imaging.

A large number of features characterizing the tissue can be calculated from the analysis of both the ultrasound signal and the image produced by the detection and display of the signal. The methods of analysis can be divided into three categories: (1) Methods which analyze the image data (2) Methods which attempt to estimate ultrasonic properties of tissue such as sound speed or acoustic attenuation and (3) methods which use ultrasound

to detect a non-acoustic physical property of tissue, such as hardness. Image analysis methods typically use statistics calculated from pixel gray values or from intensity values calculated from the envelope detected radio frequency signal. These statistics typically describe the spatial variation in signal intensity or the average signal intensity from a region of interest.

Methods based on the acoustic properties are entirely concerned with estimating a single acoustic property from the backscattered ultrasound by eliminating system effects and effects of other interactions. Examples of specific acoustic properties include frequency - dependent backscatter coefficients, acoustic attenuation and speed of sound.

Techniques that employ non-acoustic tissue properties focus on estimation of tissue elasticity from the motion of tissues in response to externally applied vibrations or to internal motion such as cardiac pulsations. Abnormal tissue is often stiff and non-elastic, causing it to move differently in response to external pressure when compared to normal elastic tissue.

2.2 Significance of Prenatal Diagnosis

Prenatal diagnosis employs a variety of techniques to determine the health of an unborn fetus. Lack of prenatal knowledge may lead to an untoward outcome for the fetus or the mother or both. Congenital anamolies account for $20 - 25\%$ of perinatal deaths. Specifically, prenatal diagnosis is helpful for:

- Managing the remaining weeks of the pregnancy
- Determining the outcome of the pregnancy
- Planning for possible complications associated with the birth process
- Planning for problems that may occur in the newborn infant
- Deciding whether to continue the pregnancy
- Finding conditions that may affect future pregnancies.

There is a variety of non-invasive and invasive techniques available for prenatal diagnosis. Each of them can be applied only during specific time periods during the pregnancy for greatest utility. The techniques employed for prenatal diagnosis are:

- Ultrasonography
- Amniocentesis
- Chorionic villus sampling (CVS)
- Fetal blood cells in maternal blood
- Maternal serum alpha-fetoprotein (MSAFP)
- Maternal serum beta - HCG
- Maternal serum estriol

2.3 Need for Prediction of Fetal Lung Maturity

Prediction of lung maturity is important in the management of high-risk pregnancies, premature labor, hemolytic disease of the newborn, premature rupture of membranes and any other situation in which early delivery of the fetus would be considered. If the lungs are mature enough to sustain the newborn with no respiratory support, then prolonging of pregnancy is not required. However, if they are immature, then the risks and costs of prolonging pregnancy may be justified, especially in settings with limited neonatal support.

Despite many recent advances in perinatal and neonatal care, respiratory distress syndrome (RDS) remains the major cause for morbidity and mortality. As a consequence of obstetric problems leading to preterm delivery, a large number of newborns in India and about 50,000 in USA are at risk for complications of prematurity every year. A newborn with RDS has physiologically immature lungs, which cannot support adequate gas exchange without medical intervention. Therefore, assessment of fetal lung maturity

is an invaluable adjunct to modern perinatal management. RDS syndrome occurs when surface-active compounds are not present in sufficient amounts for alveoli to remain open at the end of expiration. The lung collapses and can only be opened for further gas exchange by the application of high positive pressure. Normal lung remains open at the end of expiration because surfactants lower the surface tension on the alveolar surfaces and allow residual air to remain in the individual alveoli.

2.4 Development of Fetal Lung

The development of fetal lung involves two aspects: biochemical aspect of fetal lung maturation is surfactant production and anatomic aspect is the development of airways and alveoli with fibroelastic components. Structural development of lung progresses through three stages [16]. During the *glandular stage* (first 16 weeks), the lobes of the lungs become well demarcated and bronchi and bronchiole airway divisions develop. The cells lining the airways are thick and columnar proximally and change to cuboidal structure peripherally. During the *canalicular stage* (from 16 to 24 weeks), distal airway development occurs in the form of branching of respiratory bronchioles and vascular proliferation at the end of airways. The cells in these distal airways change from cuboidal proximally to thinner flattened epithelial cells distally. At this stage, the lungs are not yet capable of respiratory function. During the *alveolar stage* (24 weeks to term), respiratory tissue begins to appear at the ends of the respiratory bronchioles as alveolar sacs and eventually, small alveoli. During this stage, respiration can occur in a premature newborn, if surfactant production is sufficient to lower the surface tension and maintain open airspace. Anatomic development of fetal lung seems to be closely related to *gestational age* (**GA**) as shown in Fig. 2.1.

2.5 Biochemical Tests in Maturity Analysis

The relationship between fetal lung maturity and gestational age can be attributed to the two enzyme systems responsible for the production of surface active compounds [41].

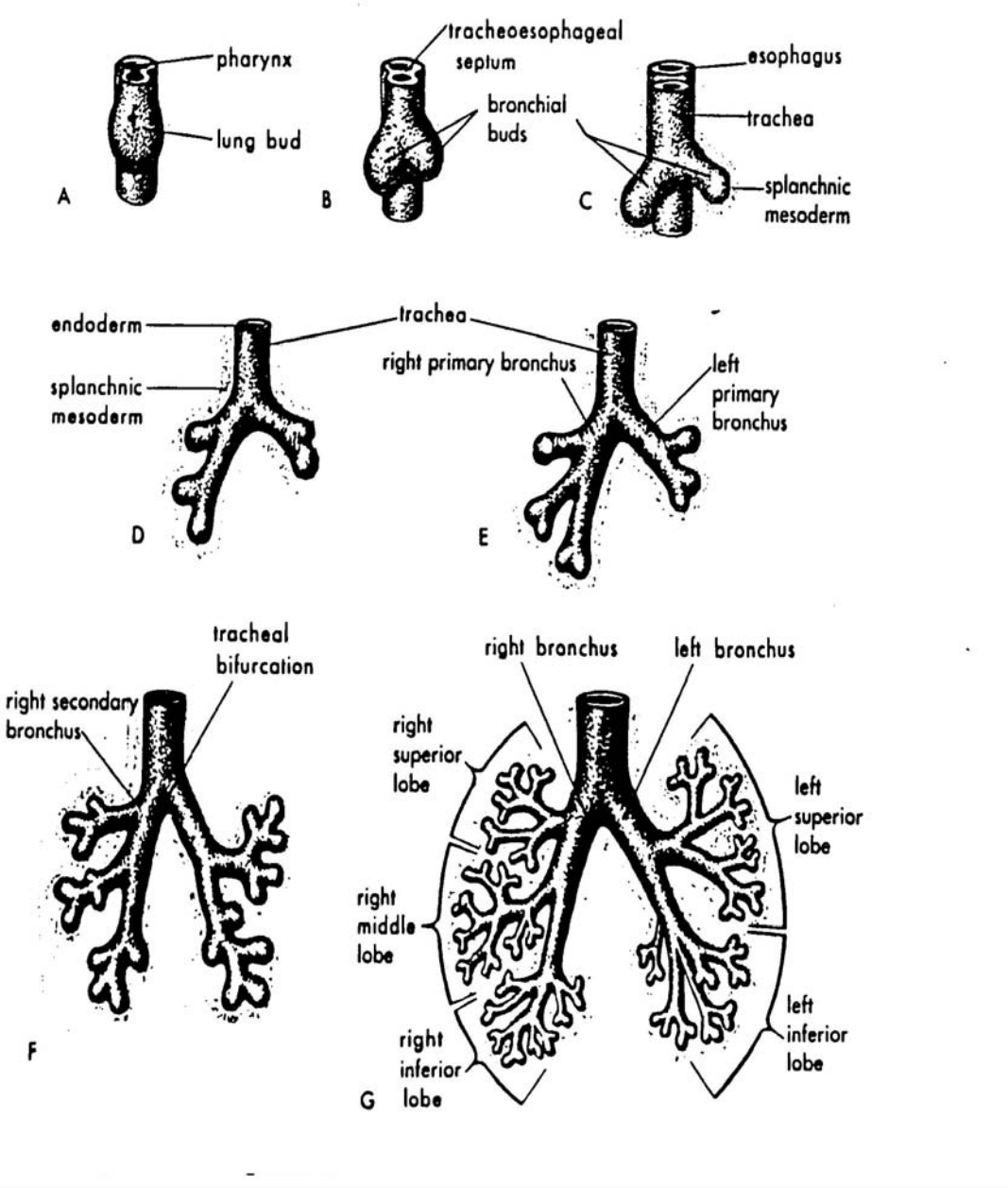

Figure 2.1: Successive stages in the development of bronchi and lungs, A to C: Four weeks, D & E: Five weeks, F: Six weeks and G: Eight weeks

The methyl transferase enzyme system begins to function at about 24 weeks and makes it possible for a prematurely born infant to sustain respiration. However, this system is not very robust and is adversely affected by the conditions associated with prematurity. At about 35 weeks, the more important phosphocline transferase enzyme system appears. Its development is very similar to the maturation of the respiratory portion of the lung.

The biochemical maturity can occur as early as 28 weeks or as late as term. Pulmonary surfactant is rich in disaturated phosphatidylcholine (Lecithin). As the lung matures, Lecithin synthesis in the lung increases dramatically. The amount of amniotic fluid and the concentration of material in it varies across pregnancies. Lecithin level is specified as ratio against sphingomyelin, a non-pulmonary lipid whose concentration is relatively constant in amniotic fluid. Thus the Lecithin level is generally expressed as a Lecithin-Sphingomyelin ratio or L/S ratio. A value of L/S ratio of greater than 2 is rarely associated with RDS, except in complicated pregnancies (Diabetes mellitus, premature rupture of membranes, etc.). L/S ratios less than 2 indicate increased risk of RDS; however, the majority of those neonates still do not develop RDS. Phosphatidylglycerol(PG) is a second lipid that shows a similar time course. It is undetectable in amniotic fluid until just prior to birth. The risk of RDS is only about 2% if PG is present.

2.6 Ultrasound for Maturity Analysis

In conventional Ultrasonography, the fetal lung maturity is analyzed by estimating the fetal size, gestational age and the condition of placenta. Physical measurements of the fetus, such as biparietal diameter, head circumference, abdominal circumference and femur length are used to estimate fetal weight. Unfortunately, these parameters are poor predictors of fetal lung maturity.

Biochemical tests, study the properties of surfactants in the amniotic fluid. This necessitates amniocentesis, an invasive procedure. L/S ratio remains the golden standard among the various biochemical tests. Despite its benefits, the invasive test is less than ideal. A positive test is highly predictive of mature lungs; however, a negative test is frequently obtained even when the lungs are mature. Many a time, sufficient amniotic

fluid may not be present to carry out amniocentesis. Further, conducting amniocentesis on high risk pregnancy subjects could lead to untoward incidences for both the mother and the child.

Ultrasound can neither measure any of the biochemical parameters of fetal lung maturity, nor provide direct histological information about fetal lung development. However, it is reasonable to assume that both morphological and biochemical changes alter the diffuse scattering and other ultrasound propagation properties of fetal lung. These changes might be detectable by conventional or specially modified pulse - echo ultrasound systems. As the fetal lung matures, the developing alveolus can be viewed as a sphere of tissue with a central cavity. During the transition from thick cuboidal epithelium to flat type I and type II epithelium, the wall of the sphere becomes thinner. The initially solid tissue volume changes to a fluid-filled space, whose diameter is about $0.05mm$. Since the wavelength of clinically useful ultrasound varies from about $1.5mm$ at $1MHz$ to about $0.15mm$ at $10MHz$, these 24 million fluid-filled alveoli should act as Rayleigh scatterers. The diffuse scattering properties should change as the fluid-content to tissue-content ratio changes. The macroaggregate effect of these morphologic changes should produce detectable changes in echogenicity and/or attenuation of fetal lung [100]. Alteration of structural changes in lung over a period of time could possibly produce different backscatter properties. This may change the textural appearance of the sonogram.

2.7 Earlier Work

In 1978, Michael Johnson suggested that ultrasound might be able to detect fetal lung maturity. Around the same time, Carson observed that alveolar bud structures are large enough to be resolved by frequency dependent scattering at the highest diagnostically useful frequencies and maturation changes might alter the sonographic appearance [14]. Carson performed experiments to study the sonographic features of fetal lung during maturation. He chose the fetal lamb as an experimental model, since it had been used extensively in pulmonary physiology research and further, lamb lung progresses through the same stages of development as the human lung. Also the fetal lamb is similar in size

to the human fetus at various stages of development. Thieme et al [100] observed that the reflectivity of lung is greater than or equal to that of liver during mid–gestation and is equal to it at term.

The first experiment to observe the sonographic features of human fetal lung during maturation was initiated in 1980. It was observed that the reflectivity of lung is equal to or less than that of liver throughout most of pregnancy but gets reversed in late gestation [39]. This is a pattern opposite to that observed in lamb studies. Another study in 1983 reported a strong relationship between a high lung-liver echogenicity ratio and subsequent absence of hyaline membrane disease in the newborn [81]. In 1984, another human study confirmed the above results by observing a group of 48 patients, where 32 had complicating factors such as diabetes, hypertension and intrauterine growth retardation.

In 1983, Benson et al [3] attempted to establish a physical basis for the development of an accurate non-invasive technique to differentiate between mature and immature fetal tissues, particularly the lung and placenta. They used RF waveform for analysis. They observed a pronounced shifting of the spectra from higher to lower frequency content for signals corresponding to mature lung and placenta, compared to those of the corresponding immature tissues. There was an increased slope of the frequency-dependent attenuation curve for these two tissues associated with the maturation processes. In contrast to the lung and placenta, the liver tissue showed very little shifting of the frequency spectra between the two states.

A study by Cayea et al [15] in 1985 compared fetal lung/liver images obtained at the time of amniocentesis to the L/S ratio and phosphatidylcholine (PC) values of the amniotic fluid. Great care was taken during imaging to eliminate artifact effects from ribs and other overlying structures. An L/S ratio greater than or equal to 2 and/or the presence of PC were defined as mature. Three ultrasound parameters were examined: (1) Lung/Liver echogenicity, (2) Lung texture and (3) Sound transmission through lung. The authors concluded that there is no statistically significant correlation between the studied sonographic features and biochemical fetal lung maturity indices.

A study reported by Fried et al [36] in 1985 compared fetal lung/liver images to

gestational age for 185 cases and to L/S ratio and PG of amniotic fluid for 37 cases. Lung echogenicity was described as hypodense, isodense, slightly hyperdense and hyperdense with respect to liver. The authors could not demonstrate any correlation between lung echogenicity and gestation age. There was no statistically significant correlation between lung echogenicity and L/S and PG determinations either. Similar to Cayea et al, the authors concluded that sonographic features of fetal lung are of no predictive value with regard to fetal lung maturity.

Crawford et al. [27] in 1985 examined the placentas of 84 antenatal patients throughout pregnancy (14 - 40 weeks of gestation). The coefficient of variation of echo-peak amplitude distributions obtained from placental images was used to characterize the placentas in different groups. Placentas of smokers had higher values of coefficient of variation throughout pregnancy. Placental texture index was significantly lower for non-smoking mothers of low-birth-weight babies after 30 weeks of gestation. They concluded that quantitative analysis of placental appearance may be of clinical value in selecting non-smoking women at risk for low-birth weight babies during third trimester.

Feingold et al. [35] in 1987 examined 23 patients who underwent simultaneous ultrasound and amniocentesis to determine whether the ratio of densitometrically determined tissue densities of fetal lung and liver correlate with L/S, OD 650 or Phosphatidylglycerol levels. They did not find any statistically significant correlation between lung/liver > 1 and any maturity parameter tested nor was there any correlation with the absence of pulmonary maturity. They inferred that this test cannot be reliably used to predict L/S, OD 650 or PG levels.

Podobnik et al. [82] in 1996 studied fetal lung maturity in normal pregnancies and pregnancies with preclampsia. They attempted to establish a relationship between gestational age and the quantitative assessment of ultrasonic signs of placental tissue, fetal lung and liver tissue. Ultrasound examinations were carried out in 240 normal and 60 preclamptic pregnancies at 30-41 weeks gestation. All patients underwent ultrasonically guided amniocentesis to obtain L/S ratio. They observed that the placental and fetal lung tissue of preclamptic patients tended to have higher coefficient of variation throughout

pregnancy. There were no significant differences in fetal liver tissue between normotensive and preclamptic groups.

Petrucha et al. [78] ultrasonically examined the placenta and found Grade III placenta patterns to be predictors of pulmonary maturity. They investigated whether biparietal diameter (BPD) and placental grade are good predictors of pulmonary maturity. They observed about 150 subjects on the above two parameters without conducting amniocentesis. The outcome of the pregnancy was normal and no child developed RDS. Their inference was that BPD of greater than or equal to 9.2 cm and Grade III placenta is at least as sensitive as the L/S ratio in predicting pulmonary maturity. Hence, this measurement can eliminate invasive test to determine lung maturity [79].

Fetal lung maturation involves a number of separate developmental processes. Initially, the fetal lungs are stiff. Compressibility typically starts after 36 weeks of gestational age. Brinholz et al. [10] studied compressibility of lung as a measure of maturity. They came to a conclusion that a study of fetal lung compressibility can be used to evaluate fetal lung development, possibly independent of gestational age and of conventionally measured lecithin/sphingomyelin values in amniotic fluid.

Sohn et al. [96, 97, 98] used fetal liver as the reference-organ to standardize the fetal lung changes depending on the age of gestation. They examined 104 patients between 27 and 41 weeks. They measured the registered frequencies in A-mode for both organs. Q-mean, a quotient of fetal lung and liver frequencies was computed. They found quotient of f-mean lower than 1.1 hinted of lung maturity, while values over 1.1 pointed to immaturity. In order to validate their results with more subjects, in 1995, they studied 428 subjects between 29 to 40 weeks of gestation and recorded the A-mode frequencies for both liver and lungs. Mean, maximal and minimal frequencies were determined. This study confirmed their earlier observations.

Christie [19] explored determination of fetal lung development by ultrasound image analysis in 1992. He analyzed similarly sized sample areas of liver and lung from the same image. He reported that the increase in pulmonary surfactant and the later development of pulmonary capillary structures can be assessed by a non-invasive technique.

There has been extensive debate for and against the use of sonographic features for analyzing fetal lung maturity. From the literature survey, we understand that there is still no conclusive report on whether ultrasound features can be used with confidence in analyzing pulmonary maturity. In most of the studies, correlation between pulmonary maturity and biochemical components are investigated. In some, placental grade and its relation to pulmonary maturity have been studied. A large number of studies have used mean echogenicity as a measure of pulmonary maturity. No work has been reported with textural features in the analysis of lung maturity.

2.8 Motivation for our Work

Our pilot study was motivated based on the earlier studies in evaluation of pulmonary maturity using ultrasound, and need for a non-invasive method to evaluate pulmonary maturity. As amniocentesis is invasive and on occasions is contraindicated, and ultrasound being harmless for both mother and fetus, we decided to look at the possible changes in the sonogram texture as a function of the gestation age. Here we have attempted quantitative texture assessment, rather than qualitative (which could be subjective).

Ultrasound echo texture has been used as a measure for quantifying the condition of adult liver by many researchers. There is a significant success in the differential diagnosis of various liver pathologies using textural parameters [107, 84, 52, 38, 44, 51]. On the other hand, we did not find much work being carried out in fetal pulmonary maturity evaluation using ultrasound echo texture. Hence, we have made an attempt in this direction to investigate the feasibility of pulmonary maturity estimation using sonogram textural features.

Chapter 3

Texture Analysis of the Sonogram for Pulmonary Risk Assessment

3.1 Acquisition of Fetal Image Data

Ultrasound examinations were performed both at Mediscan Systems, Chennai, India and at the University Hospital in Kuala Lumpur, Malaysia. Data was collected in both places using the real time ATL Apogee 800 plus scanner with a 3.5 MHz curvilinear, broad bandwidth transducer probe with the dynamic range set at 55 dB. Adequate care was taken to ensure that imaging was performed in a similar way at both locations. Scanning was performed with tissue specific presets at both centers. The tissue specific presets were similar on both equipments and same presets were used across all subjects. Only the gain was changed during scan. The overall gain was set at an optimal value to get uniform visibility. Longitudinal and transverse sections of the fetal thorax and upper abdomen were imaged. The fetal lung and liver were identified in the thoracic and upper abdominal sections, respectively. Care was taken to avoid obvious vascular structures in the liver and shadowing from the ribs. Care was also taken to have uniform plane of section in all fetuses. When fetal movement was encountered, sectioning was avoided till the fetus was at rest. This ensured uniformity of section throughout the study. Motion artifacts were avoided. A constant zoom factor was used to facilitate obtaining sufficient sample size.

Abnormally obese patients were avoided to maintain reasonable uniformity in the depth and also to avoid increased attenuation in subcutaneous fat which can occur in obese patients. Subjects chosen had normal volume of amniotic fluid, as it was considered to be important to maintain reasonable uniformity in depth and attenuation. The machine settings were optimized to obtain a uniform echo texture. The post-processing curves were unchanged. The focal zone was adjusted so that the area of interest was always in the focal zone.

Data was collected from the subjects at GAs from 24 to 38 weeks, at regular intervals of 2 weeks. Since most deliveries after 34 weeks can be effectively handled with medical support, and in most Asian races the pregnancy ends around 38 weeks, data was collected only up to 38 weeks. Images were acquired from more than 350 subjects over a period of 18 months. The subjects were rigorously followed up throughout the pregnancy and also after delivery. Only the data corresponding to normal pregnancies, also leading to babies with normal pulmonary functions, are included in our analysis. Subjects were considered as normal based on the following criteria.

- Gestation age as assessed by fetal measurements corresponded with age calculated from the menstrual history.
- Fetal growth was within the normal limits for the population and growth disorders like growth restriction and macrosomia were excluded.
- There was no maternal complications like diabeteus mellitus, hypertension or albuminuria.
- The maternal weight gain was appropriate.

The purpose of our pilot study was to obtain the trend of the textural features of the normal fetal lung as a function of the GA. A cross- sectional study of normal fetuses have shown that the overall size of a fetus at each GA falls within a range of 5^{th} to 95^{th} centile. Hence, in our study, since normal subjects are chosen, large variations in depth were not encountered. The lung and the liver areas taken for analysis were contiguous and

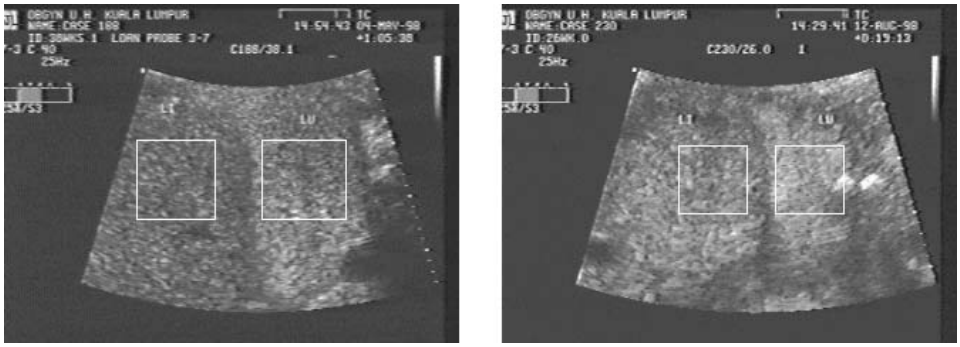

Figure 3.1: Samples of fetal echogram with lung and liver regions and ROI

at the same depth for each fetus. The appropriate section of each image was frozen and then transferred to a videotape. The images were then digitized using the Creative video grabber card. The size of the digitized image is 320×240 pixels with a resolution of 29 pixels per cm. Histogram was linearly stretched to occupy the entire range of gray values. A ROI of 64×64 pixels was used for extracting a number of quantitative parameters related to texture. Figure 3.1 shows samples of fetal echogram, with the ROI selected from both the liver and lung regions. The lung to liver ratio of various feature values were studied as possible indices of maturity.

3.2 Introduction to Texture Analysis

Texture refers to properties that represent the surface or structure of an object. Texture consists of texture **primitives** or texture **elements**, called **texels**. Texture can be described as **fine, coarse, grained, smooth,** etc. Texture analysis is one of the most important techniques used in analysis and classification of images having repetition or quasi-repetition of fundamental image elements. It is widely used in interpretation and classification of terrain images, microscopic cell images, medical images and many other domains of pattern recognition.

To discriminate images, with different textural characteristics, it is essential to extract texture features which completely embody information about the spatial distribution of

intensity variations in each image. Two main texture description approaches exist - **Statistical** and **Syntactic** [46]. The textural features are extracted either directly from the image statistics or from the spatial frequency domain.

Statistical methods describe textures in a form suitable for statistical pattern recognition. Syntactic and hybrid methods are not as widely used as statistical approaches. Syntactic texture description is based on an analogy between the spatial relations of the texture primitive and the structure of a formal language. Descriptions of textures from one class form a language that can be represented by its grammar. A grammar is inferred from a training set of words of the language during the training phase. One grammar is constructed for each texture class present in the training set. The recognition process is then a syntactic analysis of the texture description word.

Statistical texture measures include:

- descriptors based on spatial frequencies.
- Co-occurrence Matrices.
- Edge Frequency.
- Primitive length.
- Laws' Textural energy measures.
- Fractal Texture descriptions.
- Texture Transform.

The simplest form of image data analysis is that of the histogram, which is a display of the frequency of occurrence of gray levels in a region or along a line in the image. This information has been described by Julesz as first-order texture statistics (i.e. giving information about gray level frequencies but not about spatial location). The first-order image features include mean gray level, variance, skewness, kurtosis and percentiles of the gray level distribution. This analysis has been implemented on several ultrasound scanners and usually allows calculation of the mean intensity value and variance of the

pixels along a given line of interest or from within a region of interest. Histogram analysis has been little used since mean pixel gray level is strongly dependent on the gain settings used in the ultrasound equipment.

Several research groups have supplemented the gray level histogram with higher order statistical features. Second-order statistical features provide not only occurrence frequencies [46] of gray levels but also spatial interdependencies between the image elements. Reath et al. [84] analyzed ultrasound images for focal and diffuse liver diseases using first and second order statistics.

Additional textural features can be obtained from gray level run-length histogram, which is a count of the number of gray level runs by length and gray level range. A run is a set of vertically and horizontally contiguous pixels displaying nearly identical gray levels[26]. Extensive work has been carried out in analysis, synthesis and recognition of textures by various research groups.

A number of approaches to the texture classification problem have been developed over the years. The most commonly used texture features that have been applied successfully to real-world textures are:

- Spatial gray level dependence matrix or co-occurrence matrix (SGLDM)
- Gray level difference matrix (GLDM)
- Fourier power spectrum (FPS)
- Laws' texture energy measures (TEM)
- Gray level run length method (GLRLM)
- Fractal measure analysis (FM)

3.3 Textural Features used in our Study

In our study, we have used first-order statistics, SGLDM, GLDM, TEM and FM for exploring the variation with gestation age in textural features of fetal lung and liver.

These features are explained in detail in the following subsections.

3.3.1 First Order Textural Statistics

The first order image features used in image processing are

- Mean
- Variance
- Standard Deviation
- Coefficient of Variation
- Skewness
- Kurtosis

These features can be computed either from the image or from the histogram of the image. *Mean* gives information of the average gray value of an image. *Variance* and *standard deviation* characterize the spread of gray values in the image. *Coefficient of variation* is defined as the ratio of standard deviation to the mean of the distribution, which also characterizes the range of gray values present in an image. The measure of asymmetry of a distribution is *skewness*; it gives information regarding the shape of the histogram around the mean. This is equivalent to the third central moment divided by the third power of standard deviation. Positive skewness indicates a distribution with a long right tail (skewed to the left), Negative skewness indicates a long left tail (skewed to the right). *Kurtosis* is the fourth central moment divided by the square of the variance. A value of $Kurtosis > 3$ indicates a distribution that is more peaked and has heavier tails than a normal distribution with the same variance. A value < 3 indicates a distribution that is flatter or has heavier flanks than the normal.

3.3.2 Spatial Gray Level Dependence Matrices (SGLDM)

The spatial gray level dependence matrix (SGLDM) or co-occurrence matrix method of texture description is based on the repeated occurrence of specific gray-level configurations in the texture. This configuration varies rapidly with distance in fine textures and slowly in coarse textures [46]. Consider a $M \times N$ image, which is to be analyzed. An occurrence of some gray-level configuration may be described by a matrix of relative frequencies $P_{\phi,d}(a,b)$, describing how frequently two pixels with gray-levels a, b appear in any window separated by a distance d in direction ϕ.

The SGLDM are based on the estimation of second order joint conditional probability density functions, $f_{\phi,d}(a,b)$. Here $f_{\phi,d}(a,b)$ is the probability that a pair of pixels separated by a distance d at an angle ϕ have gray levels a and b. The angles are quantized to 45^o intervals. The estimated probability density functions, denoted by, $P_{\phi,d}(a,b)$ are defined as,

$$\begin{aligned} P_{0^o,d}(a,b) &= |\{[(k,l),(m,n)] \in D : \\ &\quad k-m=0, |l-n|=d, f(k,l)=a, f(m,n)=b\}| \end{aligned} \tag{3.1}$$

$$\begin{aligned} P_{45^o,d}(a,b) &= |\{[(k,l),(m,n)] \in D : \\ &\quad (k-m=d, l-n=-d) \;\; OR \;\; (k-m=-d, l-n=d), \\ &\quad f(k,l)=a, f(m,n)=b\}| \end{aligned} \tag{3.2}$$

$$\begin{aligned} P_{90^o,d}(a,b) &= |\{[(k,l),(m,n)] \in D : \\ &\quad |k-m|=d, |l-n|=0, f(k,l)=a, f(m,n)=b\}| \end{aligned} \tag{3.3}$$

$$\begin{aligned} P_{135^o,d}(a,b) &= |\{[(k,l),(m,n)] \in D : \\ &\quad (k-m=d, l-n=d) \;\; OR \;\; (k-m=-d, l-n=-d), \\ &\quad f(k,l)=a, f(m,n)=b\}| \end{aligned} \tag{3.4}$$

where $|\{....\}|$ refers to set cardinality and $D = (M \times N) \times (M \times N)$. If a texture is coarse and d is small compared to the sizes of the texture elements, the pairs of points at the separation distance d will usually have similar gray values. Conversely, for fine structures the gray levels of points separated by d will often be quite different. Haralick [6] proposed 14 texture measures that can be extracted from the $P_{\phi,d}(a,b)$ matrices. In our study, only the following five texture features [7] are computed.

$$Energy = \sum_{a=0}^{N_G-1} \sum_{b=0}^{N_G-1} [P_{\phi,d}(a,b)]^2 \tag{3.5}$$

$$Entropy = -\sum_{a=0}^{N_G-1} \sum_{b=0}^{N_G-1} P_{\phi,d}(a,b) log\ P_{\phi,d}(a,b) \tag{3.6}$$

$$Inertia = \sum_{a=0}^{N_G-1} \sum_{b=0}^{N_G-1} (a-b)^2 P_{\phi,d}(a,b) \tag{3.7}$$

$$Local\ \ Homogeneity = \sum_{a=0}^{N_G-1} \sum_{b=0}^{N_G-1} \frac{1}{1+(a-b)^2} P_{\phi,d}(a,b) \tag{3.8}$$

$$Correlation = \frac{1}{\sigma_x \sigma_y} \sum_{a=0}^{N_G-1} \sum_{b=0}^{N_G-1} (a-\mu_x)(b-\mu_y) P_{\phi,d}(a,b) \tag{3.9}$$

where N_G is the number of gray levels in the image and

$$\mu_x = \sum_{a=0}^{N_G-1} a \sum_{b=0}^{N_G-1} P_{\phi,d}(a,b)$$

$$\mu_y = \sum_{b=0}^{N_G-1} b \sum_{a=0}^{N_G-1} P_{\phi,d}(a,b)$$

$$\sigma_x^2 = \sum_{a=0}^{N_G-1} (a-\mu_x)^2 \sum_{b=0}^{N_G-1} P_{\phi,d}(a,b)$$

$$\sigma_y^2 = \sum_{b=0}^{N_G-1} (b-\mu_y)^2 \sum_{a=0}^{N_G-1} P_{\phi,d}(a,b)$$

Each measure is evaluated for $d = 1$ and $\phi = 0^o, 45^o, 90^o$ and 135^o

The contrast is a measure of how many large gray level differences are present in the

region of interest. Entropy is a measure of the uniformity of matrix values; it increases with increasing coarseness of the image texture. Local homogeneity is a measure of the degree of clustering of co-occurrence matrix values around major gray level transitions. Correlation is a measure of the linearity of the gray level relationship in d related pixels.

The co-occurrence method describes second order image statistics and works well for a large variety of textures. It characterizes the spatial relations between tonal pixels, and is invariant to monotonic gray-level transformations. On the other hand, it does not consider primitive shapes, and therefore cannot be used for large primitives. Memory requirements is another big disadvantage. Although co-occurrence matrices are very good in discriminating between textures, the method is computationally intensive.

3.3.3 Gray Level Difference Matrix (GLDM)

Let $I(x, y)$ be the image intensity function. For any given displacement $\delta = (\Delta x, \Delta y)$, let $I_\delta(x, y) = |I(x, y) - I(x + \Delta x, y + \Delta y)|$, and $f'(i|\delta)$ be the probability density of $I_\delta(x, y)$. If there are m gray levels, this has the form of a m-dimensional vector whose i^{th} component is the probability that $I_\delta(x, y)$ will have value i. The value of $f'(i|\delta)$ is obtained from the number of items $I_\delta(x, y)$ occurs for a given δ, i.e

$$f'(i|\delta) = P(I_\delta(x, y) = i)$$

Four possible forms of the vector δ were considered: $(0, d)$, $(-d, d)$, $(d, 0)$ and $(-d, d)$ where d is the interpixel distance. From each of the density functions five texture features were extracted. They are

$$Contrast : CON = \sum_{i=0}^{N_G - 1} i^2 f'(i|\delta) \tag{3.10}$$

$$Mean : MEA = \sum_{i=0}^{N_G - 1} i f'(i|\delta) \tag{3.11}$$

$$Entropy : ENT = \sum_{i=0}^{N_G - 1} f'(i|\delta) log(f'(i|\delta) \tag{3.12}$$

$$Inverse\ \ Difference\ \ Moment : IDM = \sum_{i=0}^{N_G-1} \frac{f'(i|\delta)}{i^2+1} \tag{3.13}$$

$$Angular\ \ Second\ \ Moment : ASM = \sum_{i=0}^{N_G-1} [f'(i|\delta)]^2 \tag{3.14}$$

3.3.4 Laws' Textural Measures

Laws' textural energy measures determine texture properties by assessing average gray-level edges, spots, ripples, and waves in texture [60]. The measures are derived from three vectors each of length three : $L3 = \{1, 2, 1\}$ which represents averaging;, $E3 = \{-1, 0, 1\}$ calculates the first difference(edges); and $S3 = \{-1, -2, -1\}$, corresponding to the second difference(spots). If these vectors are convolved with themselves or with one another we obtain the following five vectors, each of length five:

$$\begin{array}{lcccccccc}
\text{L5} & = & \{ & 1, & 4, & 6, & 4, & 1 & \} \\
\text{S5} & = & \{ & \text{-1}, & 0, & \text{-2}, & 0, & \text{-1} & \} \\
\text{R5} & = & \{ & 1, & \text{-4}, & 6, & \text{-4}, & 1 & \} \\
\text{E5} & = & \{ & \text{-1}, & \text{-2}, & 0, & 2, & 1 & \} \\
\text{W5} & = & \{ & \text{-1}, & 2, & 0, & \text{-2}, & 1 & \}
\end{array}$$

which perform local averaging, spot, ripple, edge and wave detection respectively. Mutual multiplying of these vectors, considering the first term as a column vector and the second term as a row vector, results in 5×5 Laws' masks. The masks used in our analysis are:

$L5^tE5$

$$\begin{bmatrix}
\text{-1} & \text{-2} & 0 & 2 & 1 \\
\text{-4} & \text{-8} & 0 & 8 & 4 \\
\text{-6} & \text{-12} & 0 & 12 & 6 \\
\text{-4} & \text{-8} & 0 & 8 & 4 \\
\text{-1} & \text{-2} & 0 & 2 & 1
\end{bmatrix}$$

$L5^tS5$

$$\begin{bmatrix}
\text{-1} & 0 & 2 & 0 & \text{-1} \\
\text{-4} & 0 & 8 & 0 & \text{-4} \\
\text{-6} & 0 & 12 & 0 & \text{-6} \\
\text{-4} & 0 & 8 & 0 & \text{-4} \\
\text{-1} & 0 & 2 & 0 & \text{-1}
\end{bmatrix}$$

The masks were convolved with each fetal lung and liver images and the energy statistics were computed. These energy statistics were used as the features.

3.3.5 Fractal Dimension and Lacunarity

Fractal based texture analysis was introduced in [76], where a correlation between coarseness and fractal dimension of a texture was demonstrated. A fractal is defined [65] as a set for which the Hausdorff-Besicovich dimension is strictly greater than the topological dimension. Fractal models typically relate a metric property such as line length or surface area to the elementary length or area used as a basis for determining the metric property. The functional relationship between the ruler size r and the measurement length L can be expressed as

$$L = cr^{1-D} \tag{3.15}$$

where c is a scaling constant and D is the **fractal dimension**. Fractal dimension correlates well with the function's intuitive roughness.

Consider the function (3.15) as a stochastic process. One of the most important stochastic fractal models is the fractional brownian motion model described in [65] which considers naturally rough surfaces as the end results of random walks. Importantly, intensity surfaces of textures can also be considered as resulting from random walks, and the fractional brownian motion model can be applied to texture descriptions. The intensity surface of an ultrasonic image can be viewed as the end result of random walks and a fractional Brownian motion model [17] can be used for its analysis.

Fractal description of textures is typically based on the determination of fractal dimension and **lacunarity** to measure texture roughness and granularity from the image intensity function. The topological dimension of an image is equal to three - two spatial dimensions and the third dimension representing the image intensity. Considering the topological dimension T_d, the fractal dimension D can be estimated from the Hurst coefficient H as

$$H = T_d - D \tag{3.16}$$

For images, $T_d = 3$ and $D = 3 - H$, where D is the fractal dimension. The Hurst parameter H or the fractal dimension D can be estimated from the relationship

$$E\left((\Delta f)^2\right) = c\left[(\Delta r)^H\right] = c(\Delta r)^{6-2D} \tag{3.17}$$

where $E(.)$ is an expectation operator, $\Delta f = f(i,j) - f(k,l)$ is the intensity variation, c is a scaling constant, and $\Delta r = ||(i,j) - (k,l)||$ is the spatial distance. A simpler way to estimate fractal dimension is to use the following equation :

$$E(|\Delta f|) = \kappa(\Delta r)^{3-D} \tag{3.18}$$

where $\kappa = E(|\Delta f|)_{\Delta r=1}$. By applying the log function and considering that $H = 3-D$,

$$\log E(|\Delta f|) = \log \kappa + H \log(\Delta r) \tag{3.19}$$

The parameter H is obtained by using least-squares linear regression to estimate the slope of the curve of gray-level differences $id(k)$ versus k in log-log scale.

Given a $M \times M$ image I, the intensity difference vector (IDV) is defined as $IDV = [id(1), id(2), ..., id(s)]$, where s is the maximum possible scale and $id(k)$ is the average of the absolute intensity difference of all pixel pairs with horizontal or vertical distance k. We compute $id(k)$ as

$$\begin{aligned} id(k) &= \frac{1}{2M(M-k-1)} \sum_{i=0}^{M-1} \sum_{j=0}^{M-k-1} |f(i,j) - f(i,j+k)| \\ &\quad + \sum_{i=0}^{M-k-1} \sum_{j=0}^{M-1} |f(i,j) - f(i+k,j)| \end{aligned} \tag{3.20}$$

Fractal dimension and lacunarity are the important features that characterize the roughness and granularity of the fractal surface.

Given a fractal set A, let $P(m)$ be the probability that there are m points within a box of size L, centered about an arbitrary point of A. Then $\sum_{m=1}^{N} P(m) = 1$, where N is the number of possible points within the box. Lacunarity [106] is defined as,

$$\Lambda = \frac{(M_2 - M^2)}{M^2} \tag{3.21}$$

where $M = \sum_{m=1}^{N} mP(m)$ and $M_2 = \sum_{m=1}^{N} m^2 P(m)$

Lacunarity represents a second-order statistic and is small for fine textures and large for coarse ones.

3.4 Feature Selection

Using the methods described above a set of 64 features were extracted at different resolutions of the images. Out of these the features of SGLDM and GLDM had similar variations with respect to GA. Since the computational cost of SGLDM features was higher than that of GLDM features, they were discarded. Among the remaining features, Fractal dimension, Intercept, Lacunarity from fractal measures, CON, MEA, IDM, ENT, ASM from GLDM, energy statistics of Laws' textural measures, Mean, Variance, Coefficient of variation, Skewness and kurtosis from histogram of the images were chosen as they exhibited notable trend with respect to GA. A second degree polynomial was fit in the least square error sense, to characterize the trend shown by these features. The various textural features and their dynamics with respect to GA is represented in Fig.3.2. Figure 3.3 presents how lung and liver features vary with respect to GA.

Various statistical tests were performed out in consultation with a bio-statistician to find the minimal number of features characterizing the changes in the lung during the pulmonary maturity process. The samples were evaluated with a confidence interval of 0.99. Figures 3.4 to 3.7 give the nature of their behaviour.

Pearson's correlation test was performed on the above mentioned 15 features to evaluate the nature of correlation between the features and GA. The results of the correlation test are given in Table 3.1. Features which exhibited good correlation with GA are: (i) Fractal dimension, (ii) Lacunarity from the fractal measures, (iii) Mean, (iv) Variance, (v) Coefficient of variation and (vi) Second moment from the histogram. Dynamics of these features with respect to GA is presented in Fig. 3.8. The characterization of the changes in the chosen lung and liver features is given in Figure 3.9. Figure 3.10 gives the statistical details of the final six features selected for classification. It was observed that data sets from both the hospitals exhibited similar behaviour.

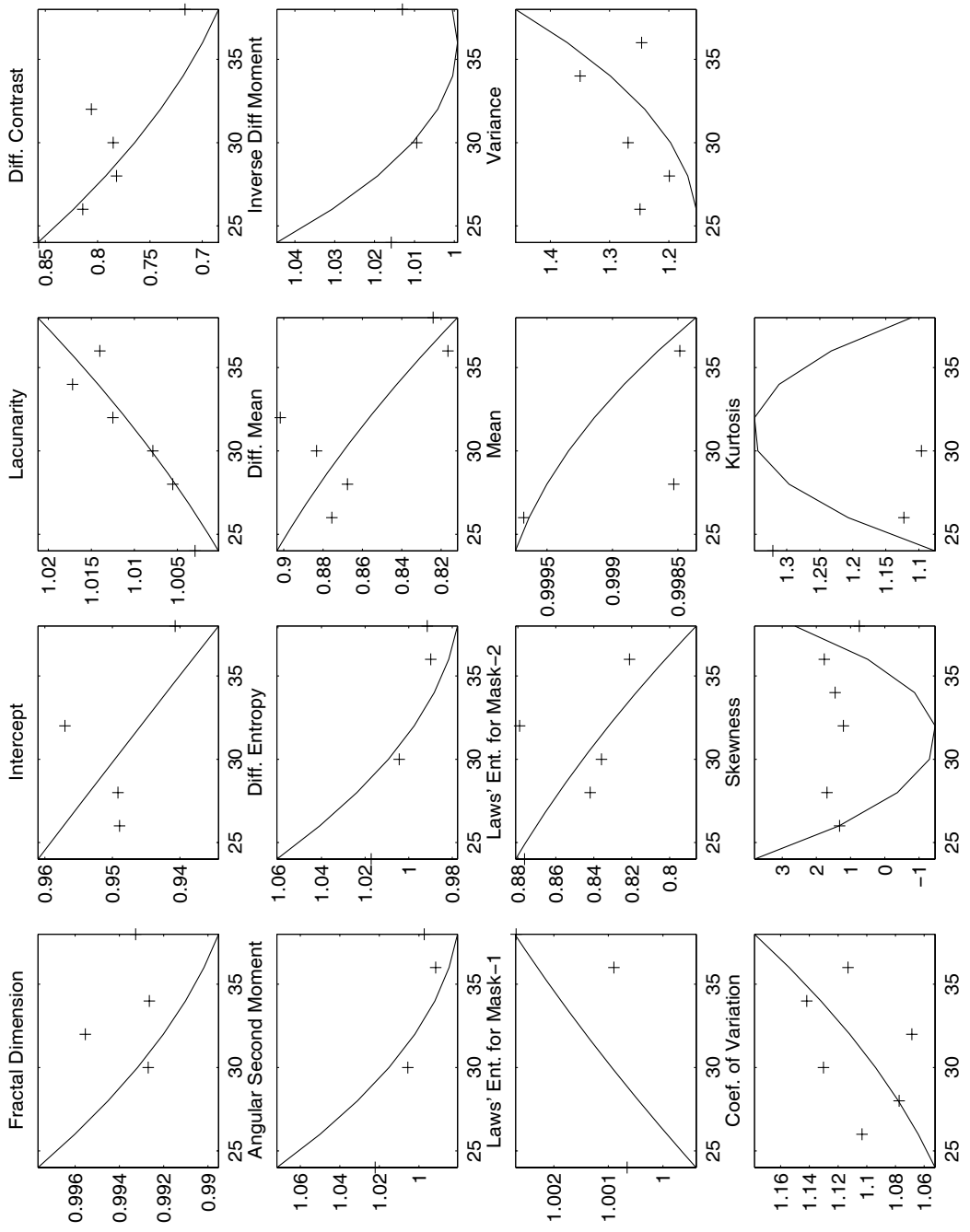

Figure 3.2: Plot showing the variation of the ratio of lung - liver feature values with gestation age

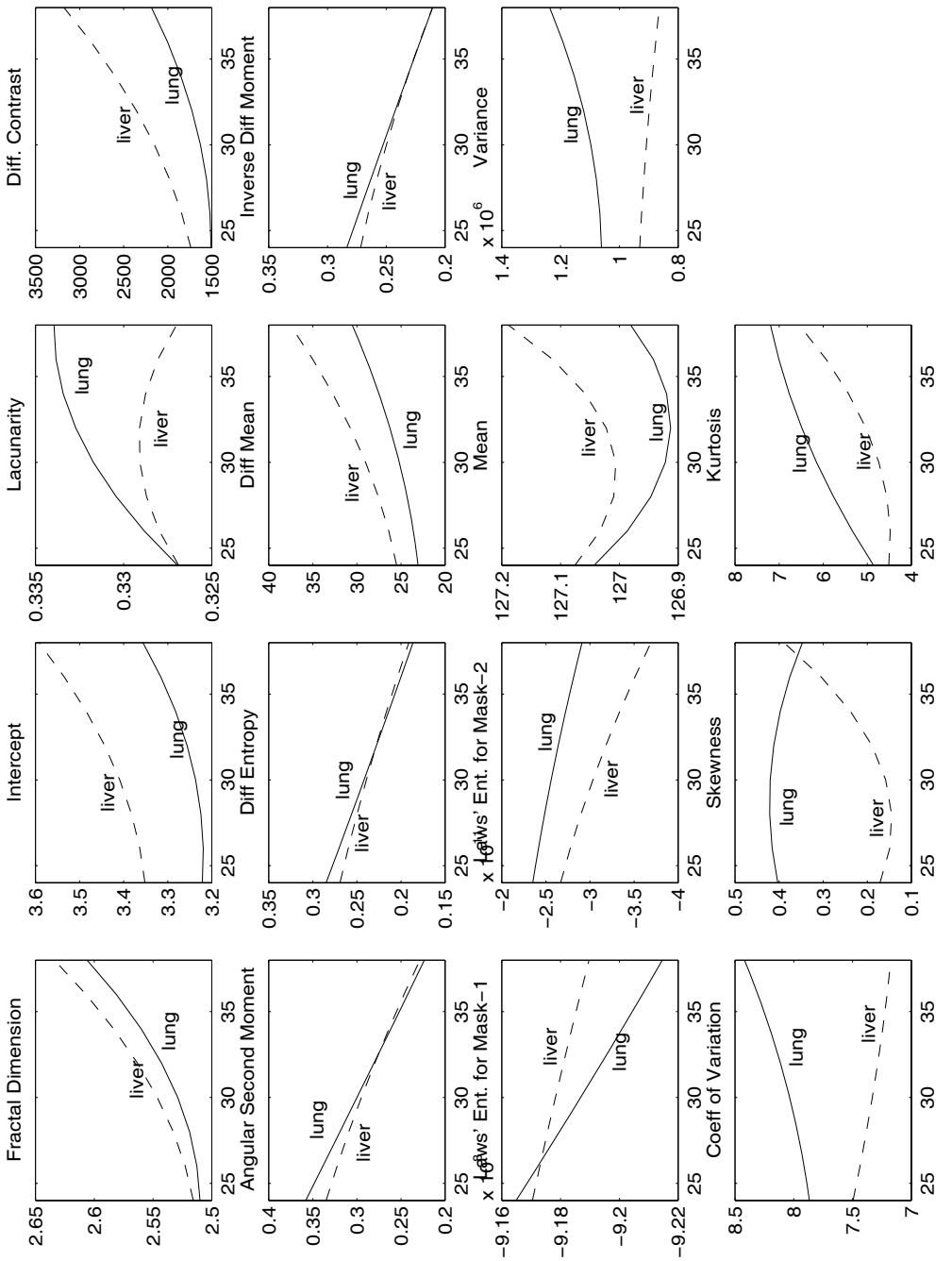

Figure 3.3: Plot showing the variation of lung and liver feature values with gestation age

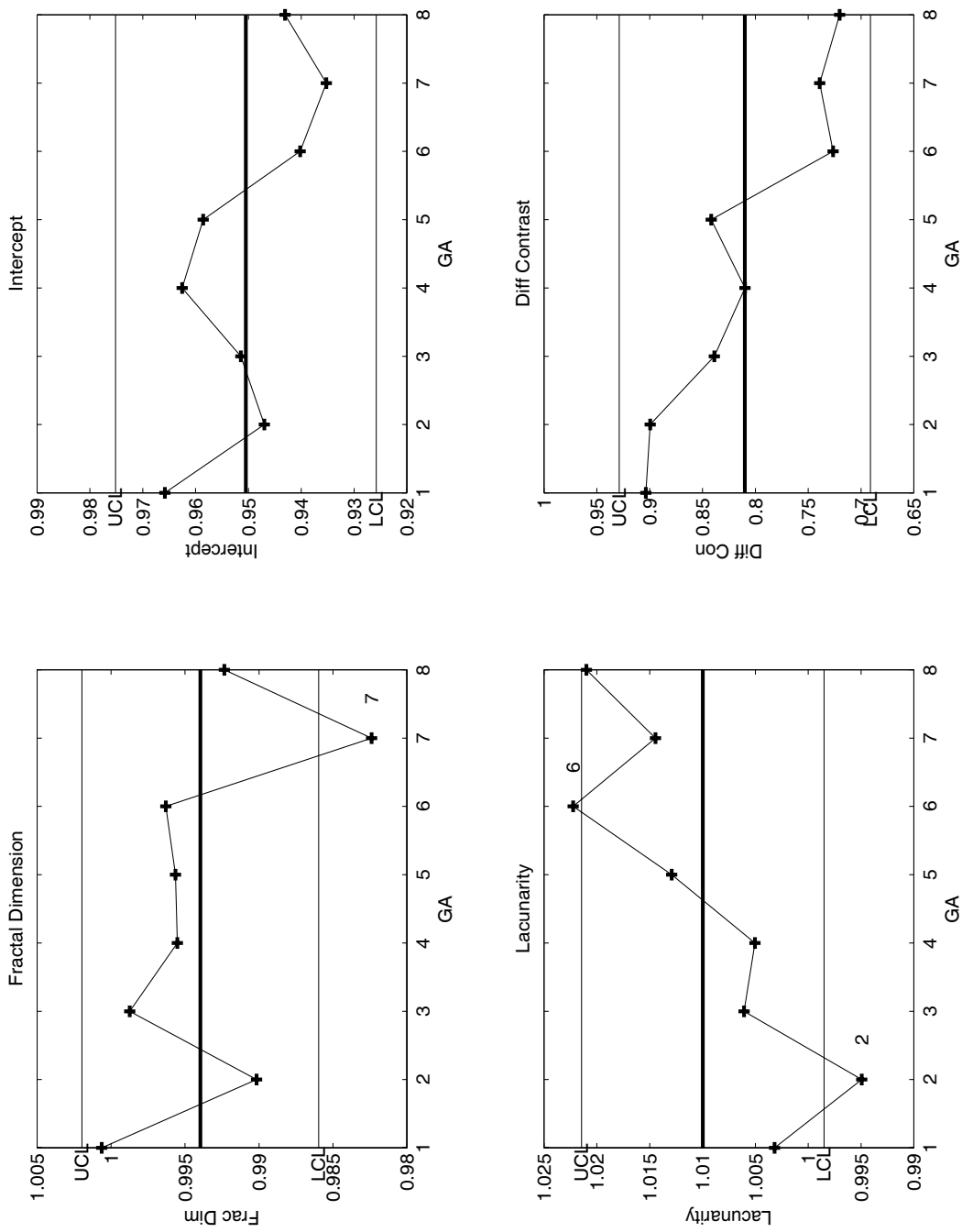

Figure 3.4: xbarplot showing the confidence interval and the outliers of features with respect to gestation age

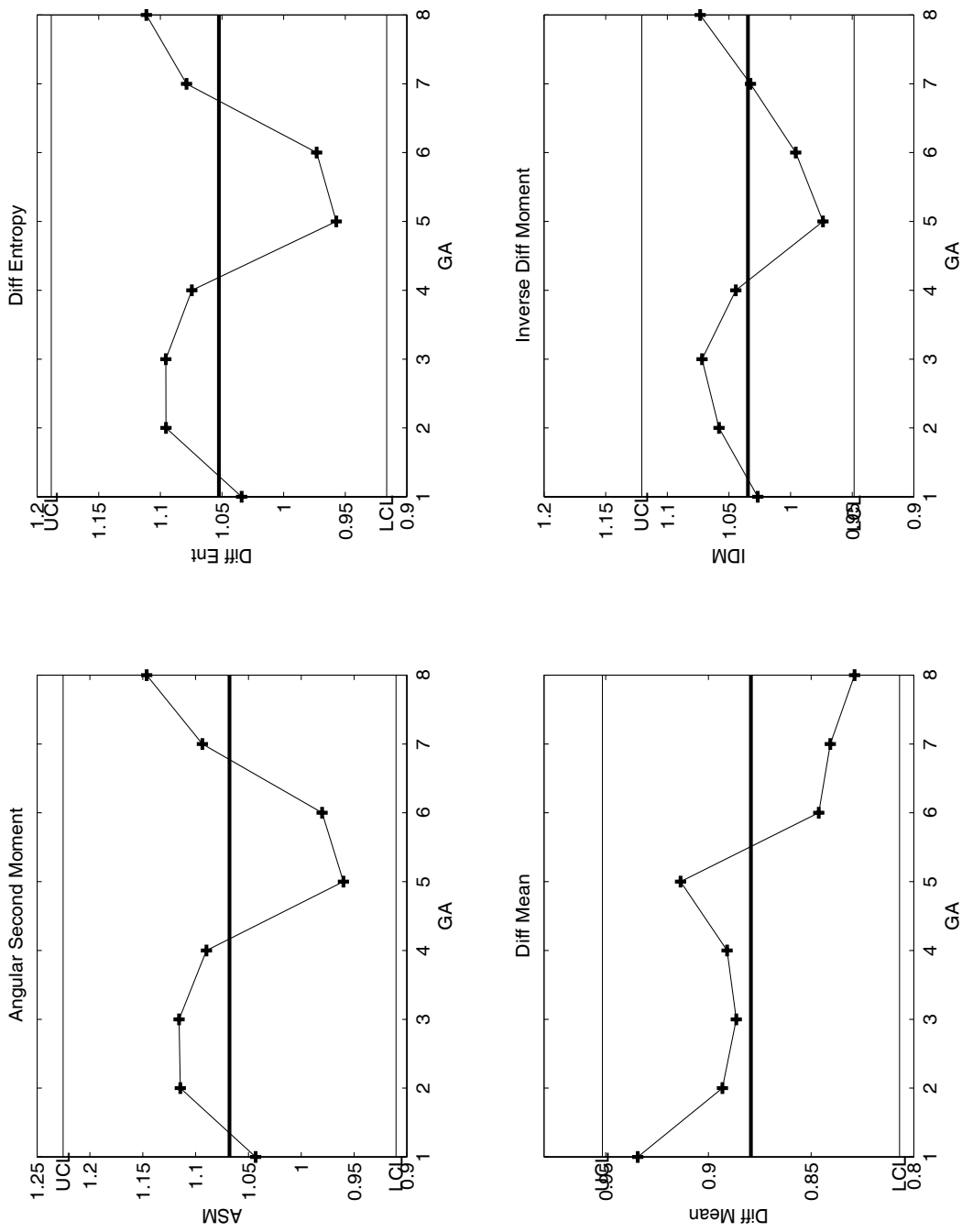

Figure 3.5: xbarplot showing the confidence interval and the outliers of features with respect to gestation age

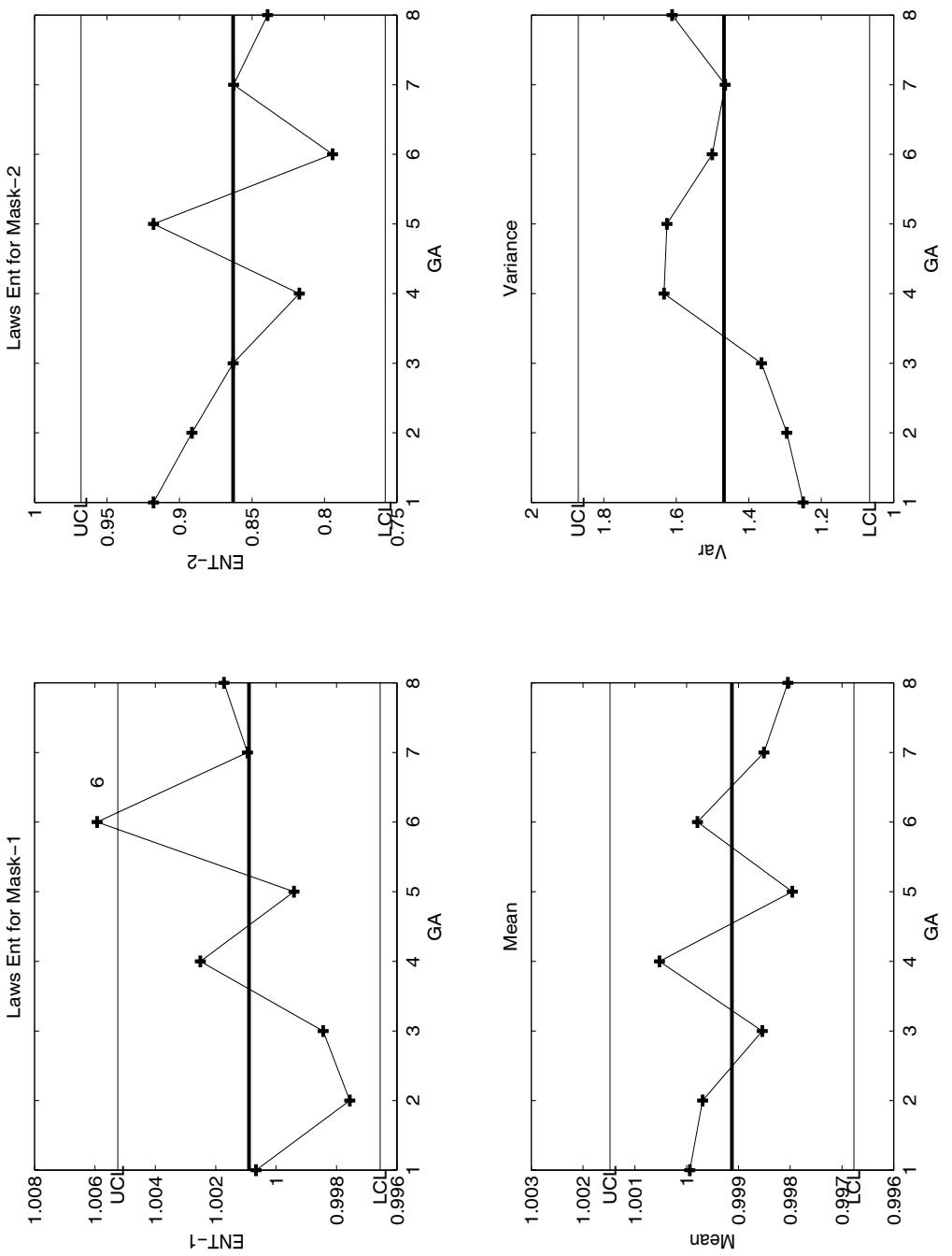

Figure 3.6: xbarplot showing the confidence interval and the outliers of features with respect to gestation age

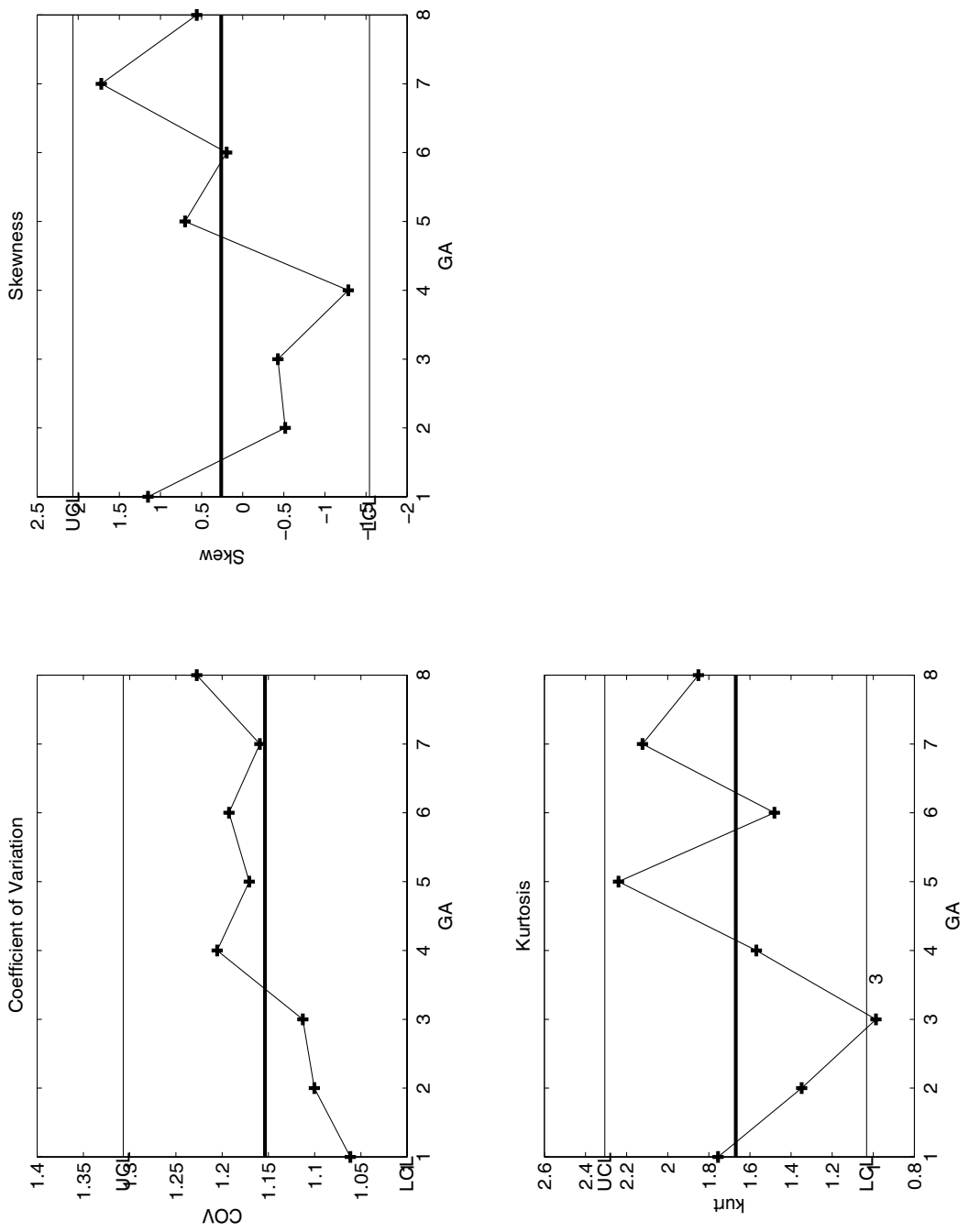

Figure 3.7: xbarplot showing the confidence interval and the outliers of features with respect to gestation age

Table 3.1: Correlation of the features with gestation age

	Coef.var	ASM	CON	ENT	IDM	MEA	ENT1	ENT2	FrDim	GA	Intr	Kurt	Lac	Mean	Skew	var
Coef.var	1	-0.2192	-0.6673	-0.2259	-0.0594	-0.7364	0.5818	-0.7685	-0.4267	0.78	-0.5761	-0.4051	0.6935	-0.1119	-0.3656	0.9776
ASM	-0.2192	1	0.435	0.9989	0.9729	0.2437	-0.5859	0.4073	0.096	-0.6254	0.2121	-0.5351	-0.7425	0.1884	0.1079	-0.127
CON	-0.6673	0.435	1	0.435	0.3018	0.967	-0.5812	0.8833	0.576	-0.8213	0.9311	0.2865	-0.7527	0.1856	0.0125	-0.6376
ENT	-0.2259	0.9989	0.435	1	0.9734	0.2467	-0.566	0.405	0.0889	-0.6348	0.2221	-0.5486	-0.7525	0.2214	0.0852	-0.1358
IDM	-0.0594	0.9729	0.3018	0.9734	1	0.0941	-0.4183	0.2038	0.1141	-0.5195	0.1022	-0.7073	-0.6091	0.2298	0.0756	0.0527
MEA	-0.7364	0.2437	0.967	0.2467	0.0941	1	-0.5054	0.88	0.585	-0.778	0.9579	0.4437	-0.6869	0.1902	-0.0585	-0.7431
ENT1	0.5818	-0.5859	-0.5812	-0.566	-0.4183	-0.5054	1	-0.7642	-0.1149	0.4937	-0.3432	-0.2921	0.6029	0.4462	-0.458	0.5471
ENT2	-0.7685	0.4073	0.8833	0.405	0.2038	0.88	-0.7642	1	0.2321	-0.762	0.7607	0.4955	-0.8116	0.0442	0.1218	-0.7868
FrDim	-0.4267	0.096	0.576	0.0889	0.1141	0.585	-0.1149	0.2321	1	-0.501	0.5781	0.0138	-0.1978	0.0886	0.1526	-0.3263
GA	0.78	-0.6254	-0.8213	-0.6348	-0.5195	-0.778	0.4937	-0.762	-0.501	1	-0.6856	0.0281	0.9358	-0.4939	-0.1108	0.7207
Intr	-0.5761	0.2121	0.9311	0.2221	0.1022	0.9579	-0.3432	0.7607	0.5781	-0.6856	1	0.3203	-0.5923	0.265	-0.2552	-0.5897
Kurt	-0.4051	-0.5351	0.2865	-0.5486	-0.7073	0.4437	-0.2921	0.4955	0.0138	0.0281	0.3203	1	0.042	-0.3917	0.1322	-0.5102
Lac	0.6935	-0.7425	-0.7527	-0.7525	-0.6091	-0.6869	0.6029	-0.8116	-0.1978	0.9358	-0.5923	0.042	1	-0.4445	-0.0326	0.6683
Mean	-0.1119	0.1884	0.1856	0.2214	0.2298	0.1902	0.4462	0.0442	0.0886	-0.4939	0.265	-0.3917	-0.4445	1	-0.4651	-0.1185
Skew	-0.3656	0.1079	0.0125	0.0852	0.0756	-0.0585	-0.458	0.1218	0.1526	-0.1108	-0.2552	0.1322	-0.0326	-0.4651	1	-0.2247
Var	0.9776	-0.127	-0.6376	-0.1358	0.0527	-0.7431	0.5471	-0.7868	-0.3263	0.7207	-0.5897	-0.5102	0.6683	-0.1185	-0.2247	1

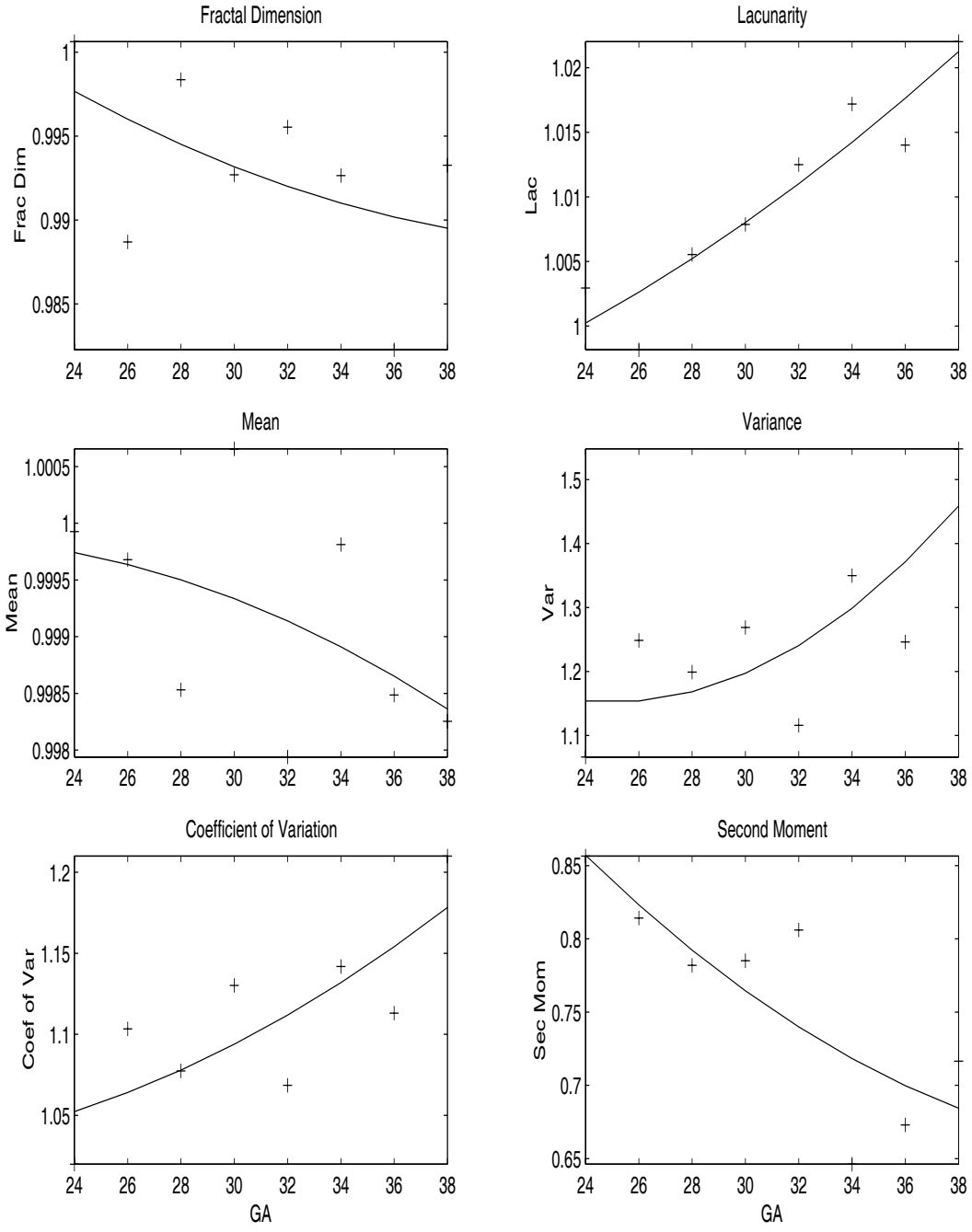

Figure 3.8: Plot showing the variation of the features (chosen for classification) with respect to gestation age

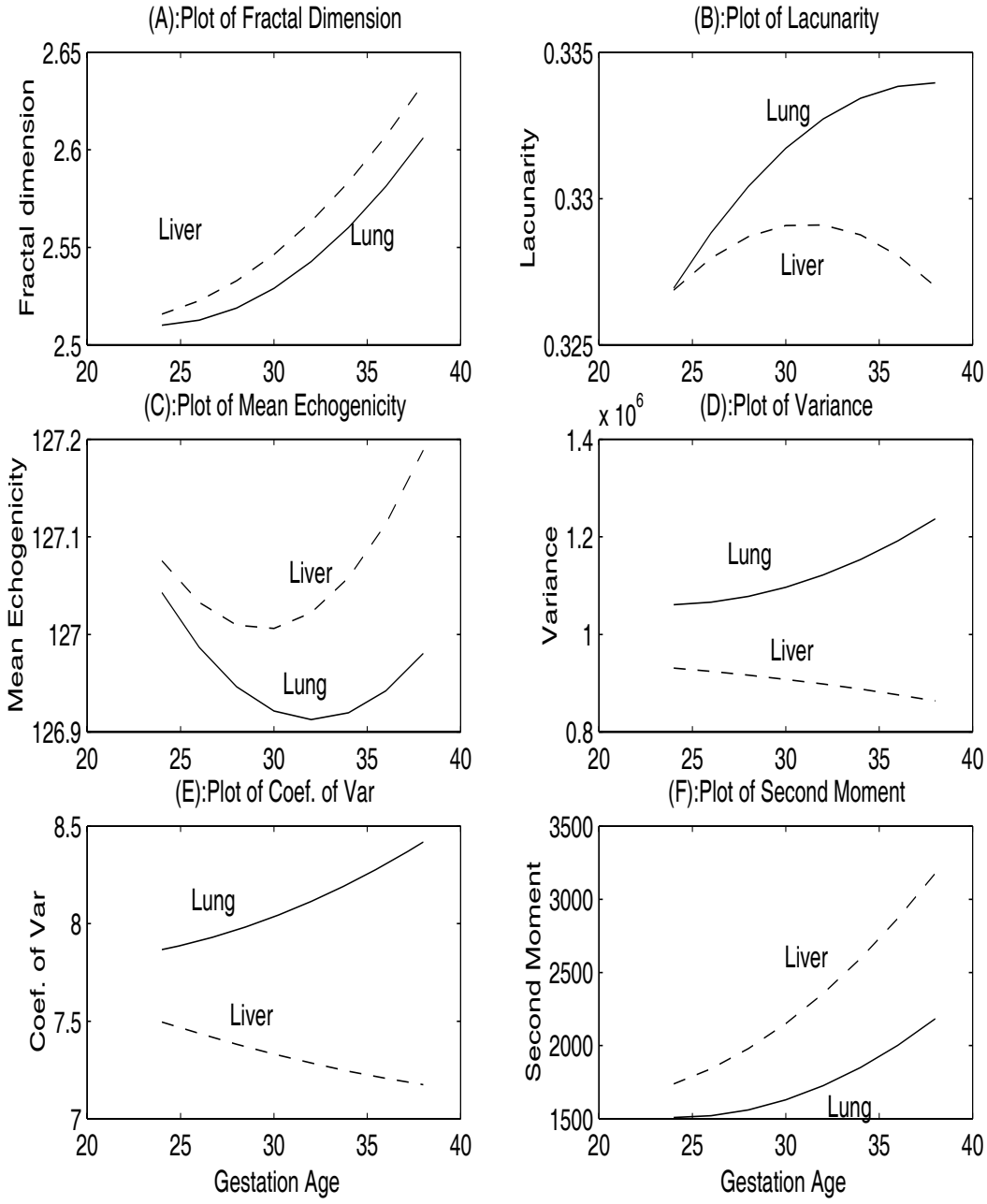

Figure 3.9: Plot showing the variation of features (chosen for classification) of lung and liver with respect to gestation age

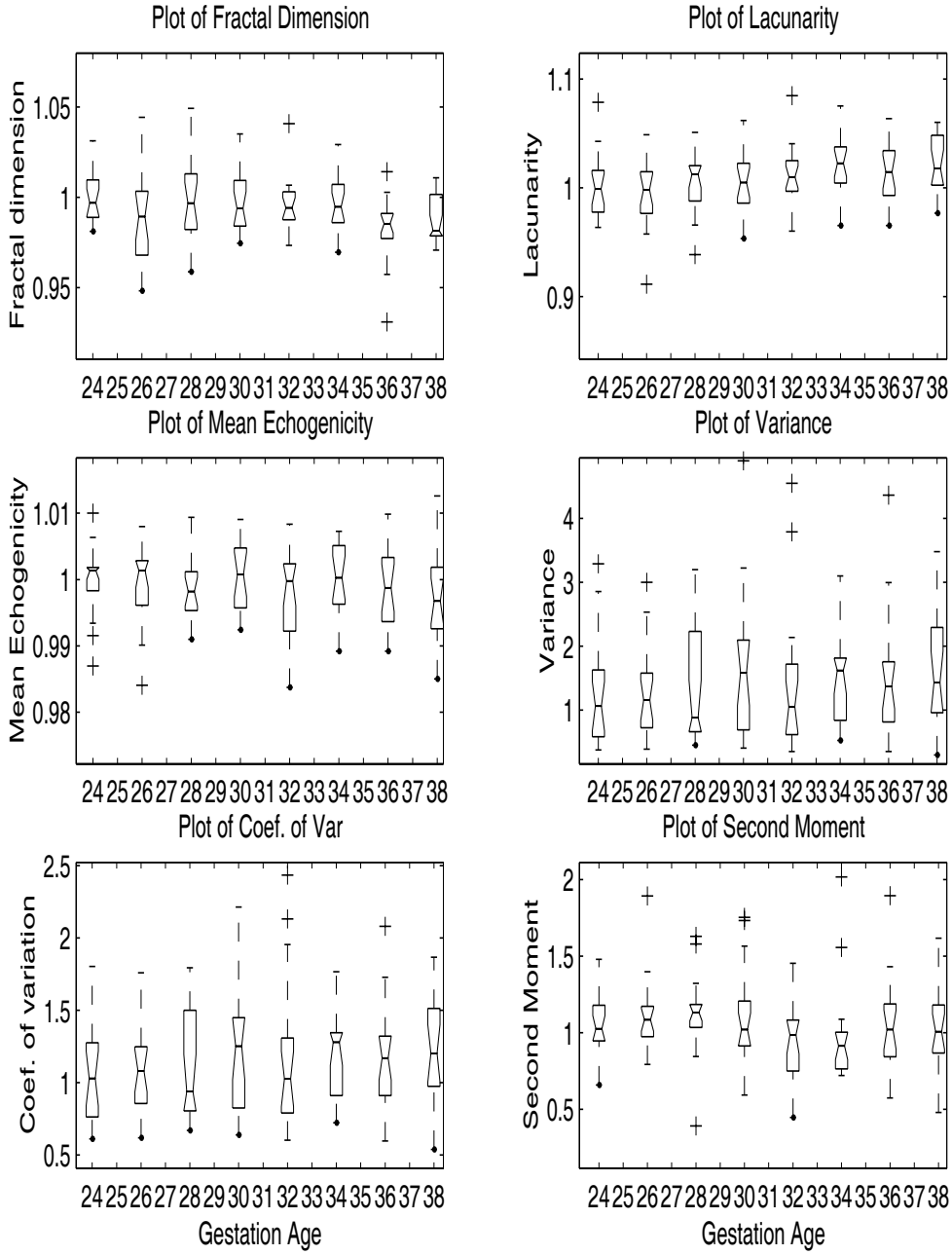

Figure 3.10: Boxplot showing the statistical details of 6 chosen features for classification

3.5 Classification of Fetal Lung

Once the appropriate set of features is extracted from the data, it is matched with the same set of features extracted from the reference patterns. The class to which the test pattern belongs is described by finding the reference pattern having the maximal resemblance to the test pattern in terms of the features.

The design of the classifier has a profound influence on the performance of a classification system. Hence, selection of appropriate features and classifier is an important step in the development of any classification system. Sufficient care needs to be taken especially in medical applications.

It is not our objective to develop a new classifier system. Hence, we restrict ourselves to test how some of the classifiers respond to the features extracted from the fetal lung and liver. A brief account of the classifiers used in our work is given in the following sections.

3.5.1 Nearest Neighbour (NN) Classifier

This classifier [32] makes use of a simple feature matching technique to declare the class of the test pattern. The algorithmic listing of the procedure is as follows:

1. Compute the Euclidean distance between the test feature vector and each of the reference vectors.
2. Find the reference vector which yields the minimum distance.
3. Declare the class of the test pattern as that of the reference vector found in Step 2.

3.5.2 k-Nearest Neighbour (k-NN) Classifier

The k-NN classifier [32] is a generalization of the NN classifier. NN classifier relies on the nearest neighbour for its decision. There is a possibility of this yielding an erroneous decision because the obtained single neighbour may be an outlier of some other class. In order to avoid this, and to improve the robustness of the approach, the k-NN classifier

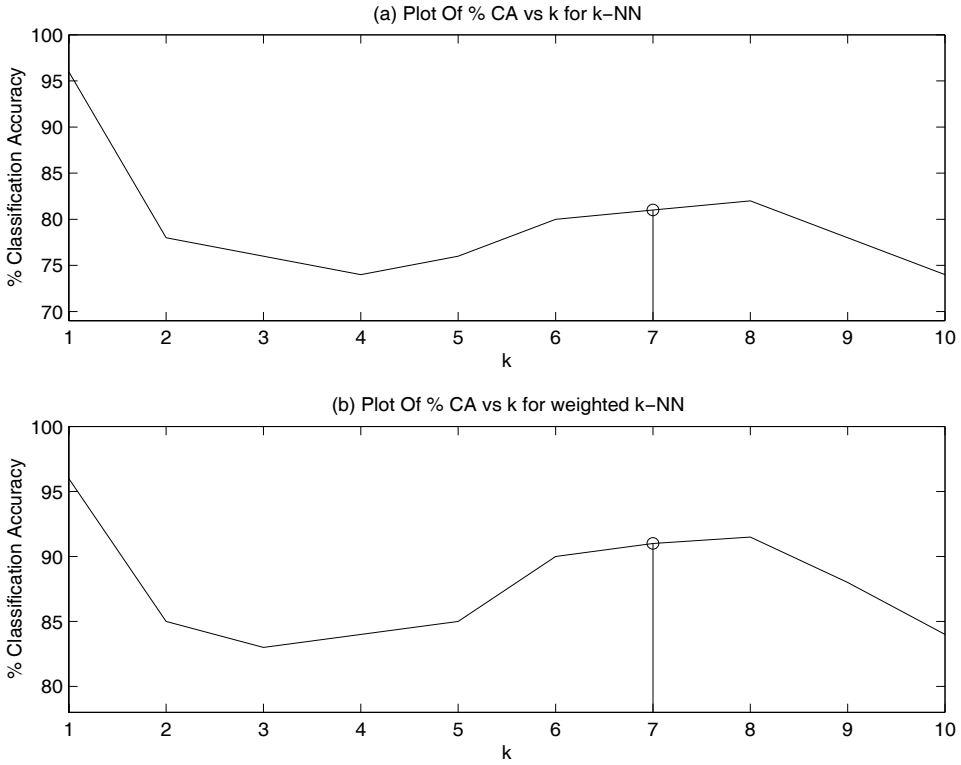

Figure 3.11: Plot of classification accuracy (CA) with respect to various values of k

works with k patterns in the neighbourhood of the test pattern in the feature space. The algorithm of the k-NN classifier is given below.

1. Compute the Euclidean distances between the test (feature) vector and each of the reference vectors.

2. Sort the reference vectors based on the distances and choose the least-distant k patterns.

3. Find the representation of various classes by counting the number of patterns belonging to each class within the $k-$ neighbourhood space.

4. Declare the test pattern to belong to the class having maximal representation.

The value of k was selected as 7 after experimental verification (see Fig. 3.11) of the classification accuracy for various values of k.

3.5.3 Weighted k-Nearest Neighbour (wk-NN) Classifier

The wk-NN classifier is a modified version of the k-NN classifier. In the k-NN classifier, though a search in the k-neighbourhood drives the classification, the distance of the test character from a template does not play any role. The k-NN classifier acts on a *population encoding* kind of strategy, where *only* the representation from each of the classes plays a crucial role, with equal weight assigned to each of the representations. In an effort to bring about a weighted representation, the weighted k-NN or the modified k-NN (mk-NN) [33] associates a distance-based weight with each prototype member in the k-neighbourhood. This weighted representation schedule then drives the classification process. The weight is calculated as follows:

Let $\mathcal{S} = \{s_1, s_2, \ldots, s_k\}$ be the set of reference patterns in the $k-$neighbourhood of the test pattern in the feature space, sorted in the increasing order of their distances from the test pattern. Let $\mathcal{X} = \{x_1, x_2, \ldots, x_k\}$ be their respective distances from the test pattern, where x_1 is the minimum and x_k is the maximum distance. Let $\mathcal{W} = \{w_1, w_2, \ldots, w_k\}$ be a weight set with w_i as the weight assigned to pattern s_i (based on its distance from the test feature vector), given as:

$$w_i = \frac{x_k - x_i}{x_k - x_1} \tag{3.22}$$

The algorithmic steps are described below.

1. Compute the Euclidean distances, x_i, between the test (feature) vector and the reference vectors.
2. Sort the reference vectors based on the distances and choose the least-distant k patterns.
3. Calculate weight w_i associated with each reference pattern s_i in the $k-$neighbourhood.
4. Find the class which contributes maximum weight in the neighbourhood. Declare the test pattern to be belonging to this class.

When investigated experimentally for the value of k, even in this case a value of $k = 7$ was selected as it had good classification accuracy (see Fig. 3.11) after the value of $k = 1$.

3.5.4 Multilayer Perceptron

Multilayer perceptron (MLP) [49], is an important class of feedforward neural networks. Typically, the network contains a set of sensory units (source nodes) that constitute *input layer*, one or more *hidden layers* of computation nodes, and an *output layer* of computation nodes. The input signal propagates through the network in a forward direction, on a layer-by-layer basis.

MLPs have been applied successfully to solve some difficult and diverse problems by training them in a supervised manner employing the *error back-propagation algorithm*. This algorithm is based on the *error-correction learning rule*. Basically, error back-propagation learning consists of two passes through the different layers of the network: a forward pass and a backward pass. In the *forward pass*, an activity pattern (input vector) is applied to the sensory nodes of the network, and its effect propagates through the network layer by layer. Finally, a set of outputs is produced as the response of the network. During the forward pass, the synaptic weights of the network are all *fixed*. During the *backward pass*, the synaptic weights are all *adjusted* in accordance with an error-correction rule. Specifically, the actual response of the network is subtracted from a desired (target) response to produce an *error* signal. This error signal is then propagated backward through the network, against the direction of synaptic connections. The synaptic weights are adjusted to make the actual response of the network move closer to the desired response in a statistical sense.

A MLP has three distinctive characteristics:

1. The model of each neuron in the network includes a *nonlinear activation function*. The important point to emphasize is that the nonlinearity is *smooth* (i.e differentiable everywhere), as opposed to the hard-limiting threshold of perceptron. A commonly used nonlinearity function is *sigmoidal nonlinearity*.

2. The network contains one or more layers of *hidden neurons* that are not part of the input or the output of the network. These hidden neurons enable the network to learn complex tasks by extracting progressively more meaningful features from the

input patterns.

3. The network exhibits a high degree of *connectivity*, determined by the synapses. A change in the connectivity of the network requires a change in the population of synaptic connections or their weights.

It is through the combination of these characteristics together with the ability to learn from experience through training that the MLP derives its computing power.

The configuration of MLP used in our study had 6 input nodes, one hidden layer with 3 nodes and 2 output nodes corresponding to the two classes, mature and immature. The network was trained using back-propagation algorithm with momentum. We have used *Netlab* software developed by Christopher M Bishop and I.T. Nabney, Neural Computing Research group, Aston University, UK.

3.5.5 Radial Basis Function

The construction of a RBF network [49], in its most basic form, involves three layers with entirely different roles. The input layer is made up of source nodes that connect the network to its environment. The second layer, the *only* hidden layer in the network, applies a nonlinear transformation from the input space to hidden space; in most applications, the hidden space is of high dimensionality. The output layer is linear, supplying the response of the network to the activation pattern (signal) applied to the input layer. A mathematical justification for the rationale of a nonlinear transformation followed by a linear transformation is based on the paper by Cover (1965). According to this paper, a pattern-classification problem cast in a high-dimensional space is more likely to be linearly separable than in a low-dimensional space.

RBF networks and MLPs are examples of nonlinear layered feedforward networks. They are both universal approximators. There exists always an RBF network capable of accurately mimicking a specified MLP, or vice-versa. However, these two networks differ from each other in several important respects.

1. An RBF has a single hidden layer, whereas a MLP may have one or more hidden

layers.

2. The computation nodes of a MLP, located in a hidden or an output layer, share a common neuronal model. On the other hand, the computation nodes in the hidden layer of a RBF network are quite different and serve a different purpose from those in the output layer of the network.

3. The hidden layer of a RBF network is nonlinear, whereas the output layer is linear. However, both the hidden and the output layers of a MLP are usually nonlinear.

4. The argument of the activation function of each hidden unit in RBF network computes the *Euclidean norm (distance)* between the input vector and the center of that unit. Whereas, the activation function of each hidden unit in a MLP computes the *inner product* of the input vector and the synaptic weight vector of that unit.

5. MLPs construct *global* approximations to nonlinear input-output mapping. On the other hand, RBF networks use exponential decaying localized nonlinearities (e.g., Gaussian functions) to construct *local* approximations to nonlinear input-output mappings.

RBF may require more number of parameters as compared to MLP for nonlinear input-output mapping for the same degree of accuracy.

The RBF was implemented using *Netlab* software developed by Christopher M Bishop and I.T. Nabney, Neural Computing Research group, Aston University, UK. The configuration used was 6 input nodes corresponding to the final features selected after the correlation test, 15 hidden nodes and 2 output nodes corresponding to mature and immature classes. Initial centers of the gaussian kernels used in the hidden layer was estimated using k-means algorithm.

3.5.6 Support Vector Machines

Amongst the discriminant approaches for classification, one of the most recent is the Support Vector Machine (SVM) [13], where the optimal hyper-plane decides the separation

between individual classes of patterns. The creation of a unique model to represent a class, derived by training the model with prototypes of each class, aids in maximization of the correct classification rate.

The concept of optimal hyper-plane was initially proposed by Vapnik [104]. The optimality is in the following sense: the average distance between the hyper-plane and the closest training points on both sides is maximal. Whereas data with linear separability may be analyzed with a hyper-plane, linearly non-separable data is analyzed with *Kernel functions* (defined below) of other types such as polynomials (of higher order), Gaussian and tan-sigmoid. It may be noted here that a linear case yields a hyper-plane.

A SVM classifier is typically defined with the *Kernel* and the vectors which act as *supports* to the decision surface. Once the functional form of the kernel is chosen, the problem of obtaining the support vectors is solved within an optimization framework. The output of a SVM is a linear combination of the training examples projected on to a high dimensional feature space through the use of *kernel* functions.

SVM Torch, a software developed by a group at IDIAP, Switzerland, [25] was used in this work.

In our study, we have used some primitive and some powerful classifiers. Our aim was to see how good the features are; i.e to check the ability of the features to characterize the changes during the process of pulmonary maturation.

3.6 Training and Test Data

In order to test the validity of the method across populations, and to confirm its robustness, samples were collected from subjects belonging to different races: Indians, Malayans and Chinese. The collected data was grouped into three classes, namely, immature, in transition and mature, depending on the GA. Samples from 24 to 32 weeks of gestation were considered to belong to the immature class (possibility of pulmonary risk), samples above 32 weeks but less than 36 weeks were considered as transition group and those from 36 to 38 weeks, as mature (reduced risk), as pulmonary risk is very rare after 35 weeks of gestation due to the presence of phosphocholine transferase enzyme system [41]. Three

different types of training and test sets were formed from the samples. The first set had 800 training and 200 test samples. Of the training data, 600 belonged to the immature class and 200, to mature class. The test set contained 150 samples of immature class and 50 of mature class. In the second training set, 400 samples were from 24 to 30 weeks of gestation, and 200, from 36 to 38 weeks. In the test set, 200 samples belonged to the transition period and 50, to 36 to 38 weeks. The third set contained 400 training samples, with equal number from immature and mature classes. The test set had 100 samples and equal number of immature and mature samples were randomly picked from the total data set. The rationale behind the selection of these three training and test sets is explained in the discussion section.

3.7 Classification Results

Figure 3.1 shows the lung and liver areas in the fetal images, and the ROI for extraction of textural features. Figure 3.10 gives the descriptive statistical details of the lung to liver feature values in the form of boxplots. It also characterizes the variation of the above features with respect to GA. Figure 3.9 demonstrates the dynamics of the features, chosen based on the correlation test, as a function of the GA for the lung and the liver. Figures 3.9A & B show that both FD and LAC increase as a function of the GA. This is to be expected because the granularity of the cells change with the GA. Explicitly, the cells of the lung are found elongated during early gestation period, which could give rise to images that are quite smooth. However, the cells become spherical and fluid-filled [100] towards the term. Further, since the fluid to tissue content ratio changes with GA, the diffuse scattering properties also change, leading to more granular images.

Figure 3.9 C shows a decrease in the echogenicity of lung as compared to the liver as the GA increases. The echogenicity of the lung is almost the same as the echogenicity of the liver at early GA. As liver enlarges in size with GA, more number of cells are formed leading to more solid tissue which in turn increases echogenicity. However, in lung during the morphological changes more fluid filled structures are formed leading to less echogenicity near the term. Results show the changing morphology in lung and liver

leading to differential interaction with ultrasound, which is brought out in our study. The variance of the gray values of the lung (Fig. 3.9 D) has an upward trend with GA, whereas that of the liver remains relatively unchanged throughout the period. The plot of CV (Fig. 3.9 E) shows a similar trend as that of the VAR and the plot of SM (Fig.3.9 F) is similar to that of FD. It may be noted that the nature of variation of the features of the liver is, in most cases, similar to that of the lung.

Further, the data was grouped based on the different asian races were evaluated using the same set of features to check the correlation with the mean behaviour of the features across the cross-section of population. It was observed that almost all samples in every group had similar variations with respect to gestation age. There were differences in the individual values of the features, but the trend remained the same. The number of samples which did not confine to the trend of the mean behaviour of the features was less than 4% in every class. These were considered as the outliers.

Table 3.2 shows the results of classification. In our training, we have considered immature lung classified as immature as true positive (TP). In all the cases, we have less number of false negatives, which is a preferred outcome. The results indicate the consistency of classification.

The descriptive statistics of the features used for the classification are given in Table 3.3. When tested for the nature of distribution of feature values, most of the features were found normally distributed at every GA. The details of the normal distribution fit are given in Table 3.4.

3.8 Discussion

In the area of fetal monitoring, a reliable method to determine lung maturity is a boon. The use of ultrasound to study fetal lung maturity is advantageous over other methods because of its non-invasive nature. Traditionally, ultrasound has been used in fetal monitoring to obtain physical measurements of fetal size and placenta condition. In our work, pulmonary risk assessment based on ultrasound textural features has given encouraging results.

In our study, we have considered three training and test sets as explained in the earlier section. This formulation is to test the generalization and adaptability of the classifiers. The first training set is more biased towards the immature class. We need our classifiers to be more sensitive and specific for the immature class, because classification of immature class as mature is less desirable. If a mature lung is classified as immature, the problem is not very serious because adequate care would be taken. The classifiers' accuracy for the training and test sets is given in Table 3.2. It may be noted that all the classifiers have almost comparable accuracy of classification, with NN and wk-NN having a little edge over the others. The number of false negatives is low for every classifier. The results show a high degree of specificity of the classifiers to the immature class.

In the second case, the training set did not contain any sample from 32 - 34 weeks, and the test set did not contain any sample from GAs below 32 weeks. This step was undertaken to ensure that the classifier is not biased by data, which could belong to either of the classes. Maturity does not occur before 32 weeks for a normal fetus, whereas it is guaranteed beyond 36 weeks [41]. Thus, the testing of images from the intervening period is likely to throw light on the transition period. An increase in the number of false negatives is seen in this case (ref Table 3.2). From the results it is evident that some of the subjects have been classified as mature even though clinically the weeks of gestation suggest that they should be in immature stage of pregnancy (before 35 weeks). However, it is understood that even in normal pregnancies when premature delivery takes place not all babies will develop RDS. This signifies that in those babies the lungs were mature enough. This would explain the fact that some of the fetuses were classified as mature before 34 weeks. As seen from the results, the NN classifier and its variants have performed poorly when compared to other classifiers, showing their poor generalization capability.

In the third set, we had equal number of samples from both classes to have an unbiased training of the classifiers. From Table 3.2, we see that even in the case of unbiased training, the classification results are very consistent, with very few false negatives. In fact, the results are very close to the biased training, and in the case of RBF and SVM classifiers,

better than the latter.

Further, the results of MLP and RBF are comparable in all the three sets. MLP and RBF are universal approximators and there exists always an RBF network capable of accurately mimicking a specified MLP, and vice-versa. In our study also, they have given similar results confirming the consistency of the classification.

The NN and wk-NN have performed better where representative samples from all GAs are used. When tested with samples only from 24 to 30 weeks and 36 to 38 weeks, all the classifiers had comparable accuracy of classification. At the boundary between the two classes, the neighbourhood classifiers have performed better. Their accuracy can be attributed to more closeness in the neighbourhood relation among the samples at the boundary of the two classes. The boundary samples along with the other samples of the two classes contribute for the greater accuracy of NN and wk-NN classifiers.

Some of the earlier studies [[35, 39, 15, 3, 82, 97]] have established the usefulness of ultrasound examinations in predicting pulmonary maturity with various degrees of accuracy, by using various features like, placenta grading, physical measurements of fetal size, echogenicity of the lung and liver regions, attenuation of frequencies in lung and liver regions, and shift in the RF frequency spectrum during the process of maturation. In our study, we have used textural features as a measure of pulmonary maturation, which has yielded an accuracy of classification from 73% to 96%. To the best of the authors' knowledge, this seems to be the first ever attempt to classify fetal lung maturity in terms of textural features of the ultrasound image.

3.9 Conclusions

Since in all the cases, the lung and the liver have been imaged together, the effects due to the imaging techniques (including the internal processing by the machine) are likely to affect both the regions similarly, and thus may not vary the textural features of the lung and liver differentially. Thus the textural features are better indicators of the histological changes, compared to the study of only the echogenicity. Based on the obtained results, it appears that a fairly good decision, about the maturity of the fetal lung, can be made

based on the characteristics of the ultrasound images.

This result is worth investigating further, because of its clinical ramifications. One of the potential areas of application of this would be when normal subjects go into premature labour. The current practice is to give an injection of steroid to the mother to accelerate lung maturity and facilitate delivery after a certain period of time. This would mean that a waiting period is essential from the time of giving the steroid injection to delivery. This may not be possible in some instances. Hence knowing maturity of the lung will help to not only prognosticate whether there is increased risk of RDS in a given fetus but also helps to alert the neonatologists to provide intensive monitoring for the new born. This exercise may possibly not be required if the lung is classified as mature prior to delivery in a preterm situation.

Being simple, non-invasive and harmless to both mother and fetus, ultrasound analysis is worth evaluating further as there is no other available gold standard for pulmonary maturity. The similar trends in features with respect to GA shown in different ethnic groups and their classification indicate though growth patterns of various ethnic groups may be different their trend of change over a period of time is maintained in different population groups. This also is an encouraging factor for further investigation to check across different populations in the world.

A complete sonographic analysis, which combines the above textural features with parameters such as fetal BPD, PG, femur length, head circumference and the abdominal circumference could possibly enhance the prediction accuracy. Also, an analysis of data from high risk pregnancies (mothers with hypertension or diabetes mellitus) could be used to further validate the prediction of maturity using sonographic features. Further investigation combining ultrasound with biochemical tests will help to establish the validity of the method and eliminate the use of invasive tests for fetal pulmonary maturity analysis.

Table 3.2: Confusion matrix of various classifiers obtained for the training and test sets 1, 2 and 3. (I: immature class, M: mature class, CA: classification accuracy and FN: number of false negatives)

Classifiers	*Correct Class*	*Classifier output*					
		Test set-1		Test set-2		Test set-3	
		I	M	I	M	I	M
NN	I	145	5	170	30	46	4
	M	3	47	33	17	0	50
	CA	96%		74.8%		96%	
	FN	5		30		4	
k- NN	I	142	8	164	36	44	6
	M	30	20	30	20	16	34
	CA	81%		73.6%		78%	
	FN	8		36		6	
mk- NN	I	147	3	170	30	46	4
	M	15	35	14	36	5	45
	CA	91%		82.4%		91%	
	FN	3		30		4	
MLP	I	150	0	187	13	46	4
	M	37	13	37	13	16	34
	CA	81.5%		80%		80%	
	FN	0		13		4	
RBF	I	142	8	190	10	47	3
	M	30	20	43	7	14	36
	CA	81%		78.8%		83%	
	FN	8		10		3	
SVM	I	142	8	165	35	47	3
	M	23	27	22	28	10	40
	CA	84.5%		77.2%		87%	
	FN	8		35		3	

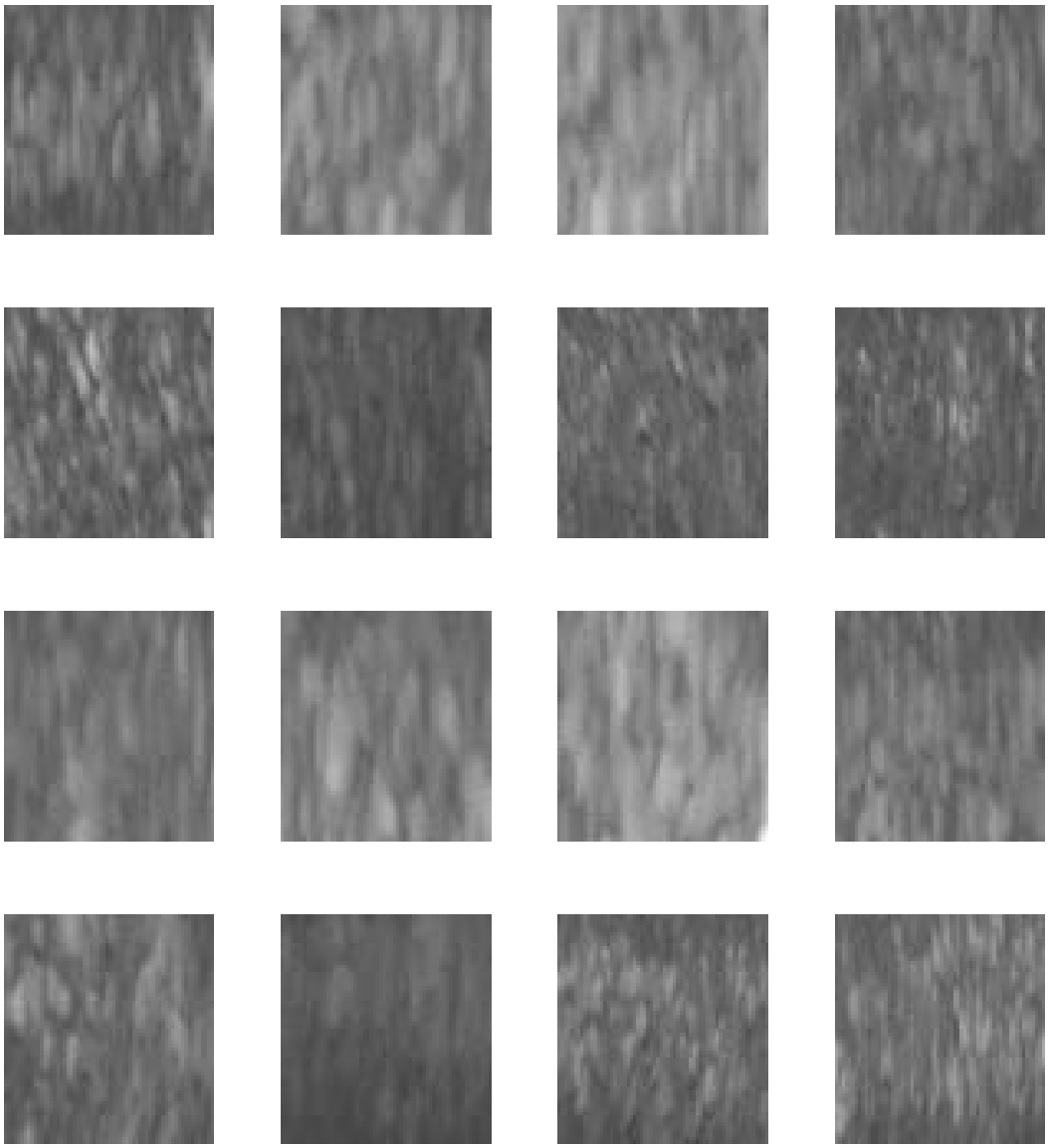

Figure 3.12: Samples of lung and liver images from GA 24 - 38 weeks. first two rows : Lung , last two rows : Liver

Table 3.3: Descriptive statistics of the features

Gestational Age	**24**	**26**	**28**	**30**	**32**	**34**	**36**	**38**
Fractal dimension								
Mean	0.998	0.993	1.000	0.994	0.990	0.994	0.984	0.992
Standard Error	0.002	0.002	0.004	0.002	0.002	0.002	0.002	0.002
Sample Variance	0.000	0.000	0.001	0.000	0.000	0.000	0.000	0.001
Minimum	0.959	0.946	0.953	0.944	0.953	0.962	0.911	0.947
Maximum	1.045	1.050	1.171	1.046	1.041	1.034	1.027	1.088
Confidence Level(95.0%)	0.003	0.004	0.007	0.004	0.003	0.003	0.004	0.005
Lacunarity								
Mean	1.004	1.003	1.008	1.007	1.014	1.007	1.018	1.022
Standard Error	0.002	0.003	0.003	0.003	0.003	0.003	0.003	0.003
Sample Variance	0.001	0.001	0.001	0.001	0.001	0.001	0.001	0.001
Minimum	0.950	0.919	0.939	0.959	0.960	0.921	0.941	0.970
Maximum	1.090	1.094	1.085	1.085	1.105	1.084	1.122	1.122
Confidence Level(95.0%)	0.005	0.006	0.006	0.005	0.006	0.005	0.006	0.006
Second Moment								
Mean	1.043	1.110	1.116	1.059	0.960	1.011	1.094	1.111
Standard Error	0.050	0.053	0.063	0.064	0.064	0.071	0.120	0.138
Sample Variance	0.045	0.064	0.071	0.093	0.073	0.115	0.261	0.440
Minimum	0.658	0.790	0.392	0.594	0.446	0.721	0.574	0.393
Maximum	1.479	1.893	1.630	1.754	1.453	2.017	2.711	3.750
Confidence Level(95.0%)	0.106	0.109	0.133	0.132	0.134	0.147	0.254	0.287
Mean								
Mean	1.151	1.141	1.111	1.112	1.174	1.179	1.156	1.249
Standard Error	0.039	0.039	0.040	0.040	0.047	0.036	0.043	0.041
Sample Variance	0.167	0.156	0.164	0.146	0.208	0.124	0.197	0.158
Minimum	0.492	0.468	0.374	0.534	0.566	0.505	0.597	0.501
Maximum	2.620	2.067	2.461	2.834	2.434	1.977	3.417	2.491
Confidence Level(95.0%)	0.078	0.077	0.079	0.079	0.093	0.070	0.086	0.081
Coefficient of Variance								
Mean	0.874	0.880	0.809	0.850	0.818	0.831	0.744	0.728
Standard Error	0.021	0.028	0.028	0.022	0.027	0.023	0.031	0.033
Sample Variance	0.045	0.083	0.079	0.044	0.070	0.053	0.102	0.100
Minimum	0.372	0.326	0.297	0.312	0.286	0.265	0.316	0.153
Maximum	1.529	1.968	1.861	1.187	1.516	1.397	2.157	1.630
Confidence Level(95.0%)	0.041	0.056	0.055	0.043	0.054	0.046	0.062	0.065

Table 3.4: Normal distribution parameters of the features

Gestational Age		**24**	**26**	**28**	**30**	**32**	**34**	**36**	**38**
Features	Parameters								
Frac Dim	$\hat{\mu}$	1.001	0.990	0.999	0.996	0.996	0.996	0.982	0.992
	$\hat{\sigma}$	0.014	0.027	0.021	0.015	0.015	0.015	0.019	0.027
	μ_{conf}	0.993	0.976	0.988	0.988	0.988	0.988	0.973	0.979
		1.008	1.004	1.010	1.003	1.003	1.004	0.992	1.006
	σ_{conf}	0.011	0.020	0.016	0.012	0.011	0.012	0.014	0.020
		0.022	0.040	0.032	0.023	0.023	0.023	0.029	0.040
Lac	$\hat{\mu}$	1.003	0.995	1.006	1.005	1.013	1.022	1.015	1.021
	$\hat{\sigma}$	0.030	0.032	0.030	0.027	0.027	0.026	0.027	0.029
	μ_{conf}	0.988	0.979	0.991	0.991	0.999	1.009	1.001	1.006
		1.018	1.011	1.022	1.019	1.027	1.036	1.028	1.036
	σ_{conf}	0.022	0.024	0.023	0.020	0.020	0.020	0.020	0.021
		0.045	0.048	0.046	0.041	0.041	0.039	0.041	0.043
Sec Mom	$\hat{\mu}$	1.040	1.110	1.120	1.090	0.960	0.980	1.090	1.150
	$\hat{\sigma}$	0.213	0.249	0.267	0.325	0.270	0.325	0.511	0.712
	μ_{conf}	0.934	0.987	0.979	0.923	0.822	0.814	0.832	0.782
		1.150	1.240	1.250	1.260	1.100	1.150	1.360	1.510
	σ_{conf}	0.160	0.187	0.200	0.244	0.203	0.244	0.384	0.534
		0.319	0.373	0.400	0.488	0.405	0.487	0.766	1.070
Mean	$\hat{\mu}$	1.000	1.000	0.999	1.000	0.998	1.000	0.999	0.998
	$\hat{\sigma}$	0.005	0.006	0.004	0.005	0.007	0.006	0.006	0.007
	μ_{conf}	0.997	0.997	0.996	0.998	0.995	0.997	0.995	0.994
		1.000	1.000	1.000	1.000	1.000	1.000	1.000	1.000
	σ_{conf}	0.004	0.005	0.003	0.004	0.005	0.004	0.005	0.006
		0.008	0.009	0.007	0.008	0.010	0.009	0.009	0.011
Coeff of Var	$\hat{\mu}$	1.060	1.100	1.110	1.210	1.170	1.190	1.160	1.230
	$\hat{\sigma}$	0.363	0.306	0.376	0.439	0.521	0.292	0.358	0.345
	μ_{conf}	0.876	0.994	0.920	0.981	0.904	1.040	0.976	1.050
		1.250	1.260	1.310	1.430	1.440	1.340	1.340	1.400
	σ_{conf}	0.272	0.230	0.282	0.329	0.391	0.219	0.269	0.259
		0.544	0.459	0.564	0.658	0.781	0.438	0.537	0.517

Chapter 4

Magnetic Resonance Imaging

4.1 Introduction

No other imaging modality has witnessed the explosion of growth and development that Magnetic Resonance Imaging (MRI) has over the past 10 years. Once labeled NMR, for Nuclear Magnetic Resonance imaging, the "nuclear" term has been removed due to its negative connotations among the general public. Using a combination of the inherent magnetic resonance properties of tissue and application of radio frequency pulses, MRI obtains images by measuring various tissue characteristics. The resulting frequency information is converted, using Fourier Transform techniques, to spatial intensity information of slices through the body. As with CT, these slices can be integrated using advanced computer graphics techniques to produce 3-D views of the imaged tissues. Unlike CT, where the signal is generated by x-ray beams, in MRI the patient becomes the signal source. MRI is extensively used in brain studies. It is an advanced medical imaging technique providing rich information about the anatomy of human soft tissue.

4.1.1 Physical Principles of MRI

Atomic nuclei of odd number of protons exhibit a magnetic moment, somewhat as if the nuclei were replaced by tiny magnets. In the absence of an applied magnetic field, these magnetic moments are arbitrary and random. Following the application of a large

magnetic field B_0 in the order of 0.3 to 2.0 Tesla, the magnetic moments of all the atomic nuclei align themselves in the direction of B_0. This results in a net magnetic moment M, the vector sum of all the individual magnetic moments of the charged nuclei, in the direction of B_0. Currently, the most prevalent entity for which measurements are taken is the ^1H nucleus. Other nuclei in the body are also suitable for measurement, but the ^1H nucleus is preferred for two reasons. Firstly, ^1H is abundant throughout the body tissues in the form of H_2O. Secondly, of all the available atomic nuclei, it is the ^1H proton that yields the highest detectable signal. Other nuclei such as ^{13}C, ^{19}F, ^{23}Na and ^{31}P, while less efficient, are finding increased use, both in research laboratories and in established MRI installations in certain hospitals. The use of these nuclei offers the advantage of exploring a large number of metabolic processes that cannot be studied using ^1H. For the rest of this discussion, we shall assume that ^1H is the nucleus of reference.

When ^1H nuclei are placed in the field B_0, they *precess* or wobble at a characteristic frequency, known as the Larmor frequency, proportional to the strength of B_0, according to the following equation:

$$\omega = \gamma B_0, \tag{4.1}$$

where ω is the Larmor frequency, γ is the magnetogyric ratio of the atomic nuclei, (for ^1H, $\gamma = 42.6 MHz/Tesla$) and B_0 is the strength of the field in Tesla.

Following the application of the magnetic field, a radio frequency (RF) pulse is applied perpendicular to B_0 at the Larmor frequency. This causes the induced magnetic moment M to rotate or *nutate* away from B_0. The extent of nutation varies linearly with the amplitude and the duration of the pulse. The operator can thus control the imaging process by controlling the above said parameters of the RF pulse. When the pulse is removed, the induced field M reverts to its original direction, namely, that of B_0. A signal is produced in the RF coil wound around the inside of the magnet bore. Two parameters, T_1 and T_2, are associated with the decay of the resonant signal, being measures of the longitudinal and transverse relaxation times, respectively.

The information obtained thus far is only a measure of the concentration of ^1H protons

in the tissue being imaged. In order to spatially locate the frequency data received, pulsed magnetic gradients are imposed in the x, y and z directions concurrently with the primary field B_0. If no gradients are applied, then all the nuclei in the magnetic field precess at the same Larmor frequency. If a gradient is applied, then the detected ω becomes a function of the position of the ^1H proton that generated the signal. These gradients are applied in a timed sequence, known as a pulse sequence. The pulse sequence of a conventional MR imager is shown in Fig. 4.1. A RF pulse, modulated by a sinc-like function, is applied at the Larmor frequency; the amplitude of the pulse determines the nutation angle. Simultaneously, a z-gradient is applied inducing a z-dependency in the Larmor frequency of the object. This determines the *slice* to be imaged within the object. The negative lobe in the z-gradient waveform, is used to rephase the spins within the excited slice. The spins within the slice can then be encoded spatially in the x and y directions.

The first pulse in the x-gradient ensures that all the spins are in phase in the resulting signal. When the signal is to be measured, the second pulse is applied to vary the Larmor frequency in the x direction. The final gradient performs encoding in the y direction. It is applied such that the incremental phase accumulation corresponds to powers of complex exponential functions. A set of RF and/or gradient magnetic field pulses and time spacing between these pulses is referred to as a pulse sequence. The period of time between the beginning of a pulse sequence and the beginning of the succeeding (essentially identical) pulse sequence is called the repetition time or TR of the cycle. The time from the center of the RF pulse to the center of the signal is known as the echo time (TE).

The data acquisition phase is terminated when many cycles of the pulse sequence illustrated in Fig. 4.1 have been applied. If the gradient fields are applied as shown in Fig. 4.1, then a transaxial slice is produced. Interchanging x, y, and z yields coronal and sagittal slices. Oblique views from any desired angle in the section being imaged can be produced by taking linear combinations of x, y, and z waveforms.

The relaxation times T_1 and T_2 are produced differently and have varying effects on the resulting image [59]. If TR and TE are relatively short, then T_1 or spin-spin relaxation times result, and the obtained images contain more detail. If TR and TE are

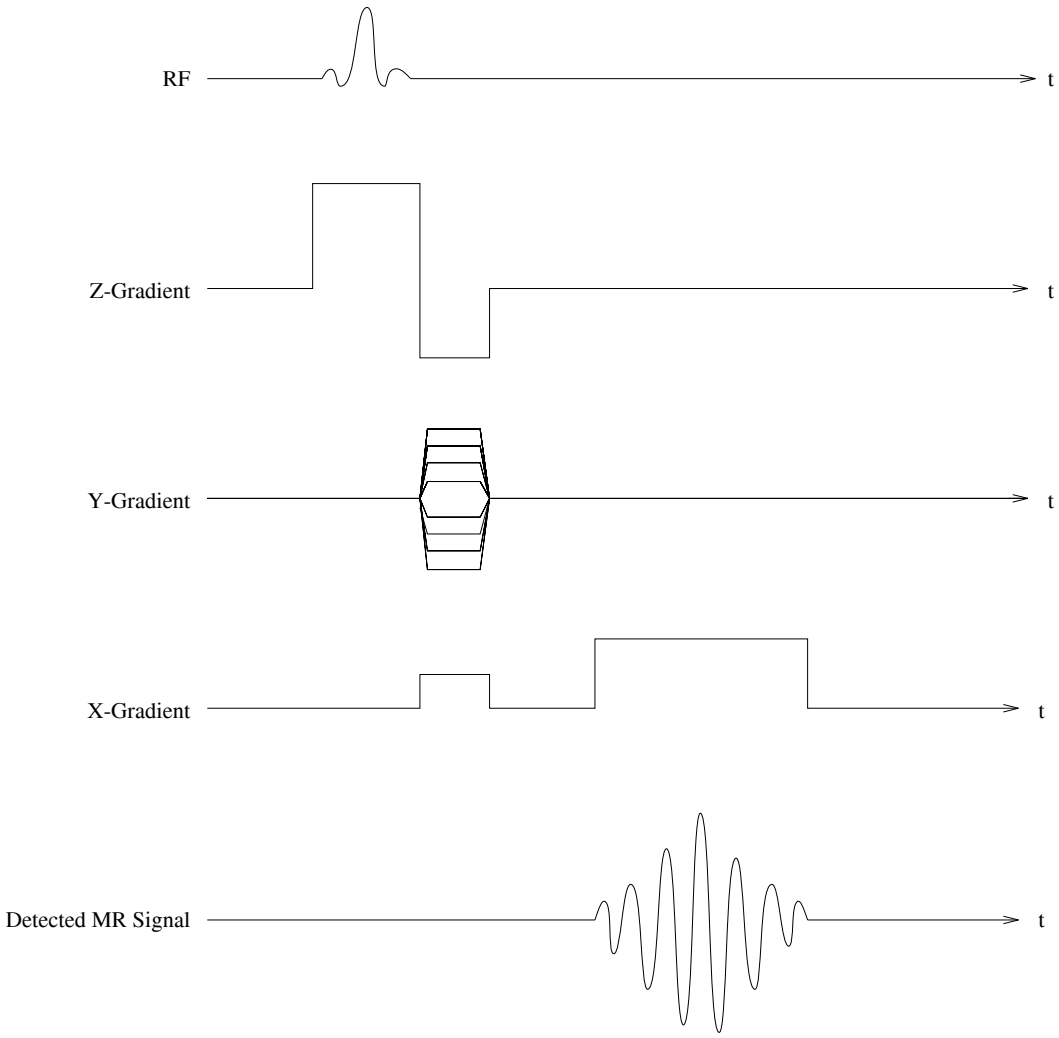

Figure 4.1: The pulse sequence of a conventional MRI system.

PD – weighted	T1 – weighted	T2 – weighted
Long TR (about 2000 ms) Short TE (5 – 30 ms)	Short TR (200 – 500 ms) Short TE (15 – 20 ms)	Long TR (2000 – 3000 ms) Long TE (100 – 200 ms)

Gray Scale	PD – weighted	T1 – weighted	T2 – weighted
	Higher PD brighter the signal intensity in the image.	Longer the spin – lattice relaxation time, darker will be the signal intensity.	Longer the spin – spin relaxation time, brighter will be the signal intensity.

Table 4.1: Characteristics of TR and TE for T1-, T2- weighted and PD images and their manifestation on the gray scale

both long, then T_2 relaxation times are produced resulting in more contrast between the different tissues. Table 4.1 illustrates this relationship between TR, TE and the different resulting images. It also shows how T1- and T2-weighted images manifest on the gray scale. The operator has full control over the T1- and T2-weighted images by regulating the application of RF pulses and the x, y, and z gradients.

The ensuing frequency encoded information can be decoded in several standard ways. The filtered back-projection methods used in CT apply equally to the reconstruction of MRI data. This was the method of choice during the early development of MRI. Today, however, the back-projection methods have largely been replaced by faster and more accurate two dimensional Fourier Transform techniques [24]. Following reconstruction, various geometric and other compensatory techniques are applied to reduce artifactual contamination caused by imperfections in the reconstruction process.

4.1.2 Current Status of MRI

While magnetic resonance imaging has many advantages over computed tomography, it also suffers from some difficulties. Clinically, MRI is superior to CT in detecting demyelinating lesions such as those found in Multiple Sclerosis. Since MRI is relatively insensitive to bone (due to the absence of H_2O in bone), it can image regions abutting bone, such as the cerebral cortex and the base of the brain, much more clearly. This imaging modality was previously the slowest of all the imaging techniques, requiring up to 8 minutes per slice and up to 45 minutes for a single examination of a desired section. Continued research has resulted in producing images in breath-holding times by reducing the number of excitations required down to just one [24]. However, most systems in operation still suffer from long examination times resulting in imaging artifacts. These artifacts arise from physiological motions due to patient breathing, peristalsis, and even pulse beats. MRI measurements are quite sensitive to even the slightest motion. Thus, patients who cannot remain still for long periods present a serious problem. The MRI source-detector coupling is housed in a large doughnut shaped structure, which encloses the patient during the examination. Many patients suffer claustrophobia when placed in the imaging area and as many as 15 percent of patients refuse the procedure on these grounds.

In addition to these patient-related difficulties, installation of MRI machines presents technical problems. The need to exclude external RF interference means that specialized rooms must be designed. This adds to the cost of the already high price of MRI equipment. Although no health related disorders have been attributed to the application of strong magnetic fields and radio frequency pulses to date, the long-term safety of MRI is yet to be determined. There are other safety factors to be considered as well, such as ensuring that the patient contains no metallic prostheses or implants, since these may lead to serious injury when the patient is placed inside the high magnetic field. RF waves also may lead to disruption of implanted pace-makers.

MRI has caused a second revolution in medical imaging and is currently still in its infancy. Future developments in reducing the scanning times and the costs to the patient, high speed reconstruction methods, and the use of several other atomic nuclei will

make MRI a leader in diagnostic radiology in years to come. Further, the ongoing research involving post-processing of MRI images using 3D graphics techniques offers broad opportunities for further development and utilization.

4.2 Basics of Image Segmentation

4.2.1 Introduction

Segmentation is one of the difficult and extensively researched problems in image analysis. Image segmentation divides an image into non-overlapping regions, each having an uniform property within itself, distinct from the other regions, for example average gray level. It is the first step in a process leading to description, classification and interpretation of an image. To date, no generalized segmentation algorithm exists, which is suitable for all or even many different types of images. Most currently available algorithms are *ad hoc* in nature. One of the reasons for the difficulty encountered in segmenting images is the infinite number of possibilities that any image can represent. A truly general image segmentation algorithm would require the use of vast amounts of knowledge and data.

Another problem is related to the evaluation of segmentation algorithms. There is no adequate solution to the problem of determining the validity or accuracy of a given segmentation algorithm. In many cases, various mathematical and other assumptions are made with respect to the image under investigation. Given these assumptions, verification of the segmentation technique is possible to some degree. However, it is generally the case that the algorithms are validated for a few, specific images. Despite these limitations, many hundreds of segmentation algorithms have been published in the literature.

The applications of image segmentation include pattern recognition, computer vision systems, biomedical applications like automated tumour volume determination and 3-dimensional visualization. Before discussing specific algorithms, it is meaningful to formally define image segmentation.

4.2.2 Definitions

Several definitions have been put forward for image segmentation; however, the one that is generally accepted as *the* definition is as follows: A *segmentation* [37] of a $2D$ image grid I, over a predicate P, is a partition of I into N non-empty, disjoint subsets $I_1, I_2, \ldots, I_N$ such that:

$$\bigcup_{i=1}^{N} I_i = I \tag{4.2}$$

$$I_i,\ i = 1, 2, \ldots, N \text{ is connected} \tag{4.3}$$

$$I_i \cap I_j = \emptyset, \text{ for all } i \neq j \tag{4.4}$$

$$P(I_i) = \ \mathit{TRUE}, \text{ for } i = 1, 2, \ldots, N \tag{4.5}$$

$$P(I_i \cup I_j) = \ \mathit{FALSE}, \text{ for } i \neq j, \text{ where } I_i \text{ and } I_j \text{ are adjacent.} \tag{4.6}$$

Equation 4.2 states that every pixel must be in some region or the other. That is, no pixel in the image can exist outside all the defined regions. Equation 4.3 stipulates that regions must be connected; each I_i is composed of contiguous lattice points. Equation 4.4 indicates that the intersection of two regions is empty; regions are disjoint. The predicate P in eqn. 4.5 implies that the region I_i must satisfy some property, for example, uniform texture. Equation 4.6 states that if two regions I_i and I_j are adjacent and disjoint, then the predicate P cannot be true for the region defined by the union of I_i and I_j. That is, properties are different for adjacent regions. The predicate P, discussed in eqns. 4.5 and 4.6, is formally defined below:

> Let I denote the sample points in the picture, i.e., the set of pairs
>
> $$(i, j) \quad i = 1, 2, \ldots, M, \quad j = 1, 2, \ldots, N$$
>
> where M and N are the number of pixels in the x and y directions respectively. Let Y be a non-empty subset of I consisting of contiguous picture points. A *uniformity predicate* $P(Y)$ is one, which (i) assigns the value "true" or "false" to Y depending only on the properties related to the brightness matrix $f(i, j)$

for the points of Y and (ii) has the property that if a region Z is a subset of Y and $P(Y)$ is true, then $P(Z)$ is also true.

The most basic form of uniformity predicate is based on the comparison of the mean pixel intensity in a given region and the standard deviation from the mean. In general, a region R is called uniform, i.e. $P(R) = TRUE$, if there exists a constant a such that:

$$\max_{i,j}|(f(i,j)) - a| \leq T$$

for some threshold T. Using the mean, μ and standard deviation, σ, this means that:

$$\max_{i,j}|(f(i,j)) - \mu| \leq k\sigma$$

for some constant k. Other features used to determine region uniformity are based on a variety of properties of the image, including the co-occurrence matrix, texture, Fourier transform and correlation functions. The elements of the co-occurrence matrix $C(i,j)$ denote the number of pairs of pixels having gray levels i and j, which exist at a particular distance apart and at a fixed angle. Properties of the co-occurrence matrix, such as entropy and correlation, are used to characterize the textures of regions [111].

4.2.3 Overview of Segmentation Methods

Image segmentation algorithms can be loosely categorized into thresholding methods, edge detection, and region oriented techniques.

The simplest method of segmentation involves thresholding. Most thresholding techniques involve a binarization of the image into foreground and background objects. All the pixels that have a certain property such as falling into a given intensity range are assigned to the same group. Pixels outside the given range are not included in the object. The application of these techniques is limited to images having few objects. Another drawback of thresholding is the difficulty in the proper selection of the threshold value required to optimally extract the desired objects. Many factors, including the characteristics of the imaged material itself, could make it difficult to obtain an optimal threshold value. The observed intensity value of an object in an image is affected by the proximity of the object to nearby objects, and imaging conditions such as lighting and shadows.

Edge detection based segmentation methods locate significant intensity changes in images that can be interpreted as edges between objects. Although many improvements have been demonstrated in recent years, the edge detection methods are still complicated by the difficulty of finding actual object boundaries as opposed to noise or artifacts. Following edge detection, it is often the case that many gaps exist along the detected contours of an object. The complexity of properly linking the fragmented edges further detracts from their usefulness.

The third general class of image segmentation techniques is formed by the region-oriented methods. These techniques assume that objects are defined by individual, closed regions in space. Region analysis techniques are further classified into region growing and region splitting and merging methods. In region growing, individual pixels or their neighbourhoods are used as seeds and an analysis is performed on the neighbours of the seeds to determine their inclusion into the region. This analysis is iteratively applied until the objects cease to grow further. The split and merge methods of region analysis work by iteratively splitting the image into smaller and smaller regions until it is determined that all the currently existing regions have some uniform property. Two adjacent regions are then merged with one another if it is determined that the merged regions also satisfy the desired property. The difficulty of defining the uniformity property and the complexity of applying these techniques detract from their general application.

Recently, the above techniques have been augmented by the incorporation of mathematical morphology, pyramidal schemes and model-based image segmentation. It has been observed that accurate segmentation of many images, especially medical images, requires external knowledge about the objects represented in the image. In order to incorporate external knowledge, many organ and tissue models have been applied to the segmentation of medical scans with limited success. Most of these model-based techniques involve the acquisition and analysis of many data sets in order to form the model. For this reason, to date, the success of these methods has been marginal.

The following subsections briefly describe the three classes of segmentation methods presented above.

4.2.4 Thresholding

The simplest method of image segmentation employs thresholding. Pixels possessing the same property (gray level, colour, etc.) are combined into a group. In its most general form, thresholding can be described mathematically as:

$$S(i,j) = k \text{ if } T_{k-1} \leq f(i,j) < T_k \text{ for } k = 1, 2, \ldots, m$$

where (i,j) are the coordinates of a pixel in the x, y directions, respectively,

$S(i,j)$ is the segmentation function,

$f(i,j)$ is the characteristic feature (e.g. gray level),

$T_0, \ldots, T_m$ are the threshold values, and

m is the number of distinct labels to be applied to the image.

If $m = 2$, the method is termed as *binary* thresholding. If $m > 2$, these methods are described as *multi-modal* thresholding techniques. Thresholding is best applied to images of relatively few homogeneous areas which are contrasted against a uniform background. For example, in the case of binary thresholding, a suitable application is extraction of text from a printed page.

Well known histogram modification and manipulation techniques are applied in image thresholding [42]. The survey papers by Lee et al. [61] and Sahoo et al. [92] indicate that *moment preserving* thresholding (MPT) [101] gives the best results among the methods tested. In MPT, the objective is to compute the k'th moments of an image and to find the threshold values that preserve the moments in the segmentation. The k'th moment of an image is defined as,

$$m_k = \frac{\sum_i \sum_j f^k(i,j)}{MN}$$

Thus the zeroth moment of an image is 1, and the first moment is the average gray level present in the image. These moments are also obtainable from the histogram of the image. Preservation of moments is motivated by the assumption that the original image is simply a blurred version of the true segmentation. Tsai et al. [101] use a value

of $k = 3$ in order to obtain segmentations using 2, 3 and 4 different threshold levels. Extensions to higher dimensional thresholding are possible but with substantial increases in computational load.

A multidimensional extension of thresholding, called feature clustering, clusters the pixels in a feature space, and then segments the image based on the properties of these clusters. Clusters are generally formed using two or more characteristic features. The clusters need not be contiguous in space.

Thresholding and clustering methods have the advantage of being fast and simple to implement. There are, however, inherent shortcomings present in all thresholding techniques. Primarily, there is the problem of threshold selection, which usually requires some *a priori* knowledge of the image being segmented. In addition, the valleys and peaks in the histograms, used to segment the images, are often not well defined and may also be affected by noise, thus making their differentiation difficult. Thus, the thresholding methods are best suited to images of low number of regions with highly contrasting backgrounds.

4.2.5 Segmentation by Edge Detection

Edge detection methods of image segmentation involve locating local discontinuities in pixel intensities, followed by some method of connecting these fragmented *edges* to form longer, hopefully significant and complete boundaries. Most methods of edge detection involve the application of a smoothing filter (e.g. Gaussian), followed by a first or second order *gradient* operator. In the case of a first order gradient, local maxima signify the existence of an edge. If a second derivative operator is applied, then zero crossings in the result indicate the presence of an edge. A thresholding operator is usually applied to the result to filter out insignificant edges, or edges caused by noise not removed by the smoothing process.

The biggest drawback of edge detection methods of image segmentation is their sensitivity to the size and type of smoothing and derivative convolution masks applied. In some cases, these two masks are not parameterized and are therefore not under user control.

This limits the applicability of these algorithms to only certain types of images.

Further, most edge detection algorithms are sensitive to noise and can yield edge points that do not lie on a boundary between regions. Furthermore, edges that are computed are often not linked, where contiguity exists in the image. In order to be useful in successfully segmenting the image, these edges must be joined. Algorithms for edge linking are often at least as complex as the edge detection algorithms used in the first place.

4.2.6 Region-oriented Segmentation

While thresholding and edge detection involve determining the differences in the intensities between pixels or groups of pixels, region based methods deal with the similarities between them. Region growing methods start with individual or sets of pixels as seeds and then analyse the neighbours of the seeds. If the neighbours have similar characteristics (intensity or some other property), then those pixels become part of a region. This process continues with the updated regions until no further expansion is possible.

One advantage of region growing is that little *a priori* information is necessary to segment the image. In addition, isolated areas with similar features can be successfully segmented by careful selection of seeds for these regions independently. Difficulties are encountered while choosing a seed point or region and evaluating criteria for including neighbouring pixels. The latter is a problem common to all techniques, namely, the selection of the threshold.

In contrast to the forms of image segmentation discussed so far, region splitting and merging begins with an image subdivided into smaller regions. These regions are grouped together if the pixel intensities meet some uniformity criteria, for example, similar average intensity level. The regions are further split if they do not meet the uniformity criterion. The order of splitting and merging is varied and is dependent on the implementation and data structures used. Relatively complex data structures are required to perform split and merge techniques with corresponding complexity in maintaining these structures. The problems of determining a valid uniformity criterion and a threshold at which to assign the uniformity, exist.

Each one of the segmentation techniques discussed above has certain merits and limitations and therefore works well for specific types of images only. Combinations of the above techniques have also been applied successfully in some cases. Thus, the choice of segmentation technique is highly application dependent.

4.3 Medical Image Segmentation

Segmentation is an important step in most medical image analyses. In many classification processes, segmentation forms the first step. The applications of segmentation include diagnosis, evaluation and treatment of disease. Since manual segmentation is tedious, time consuming and subjective, attempts have been made to automatically classify and quantify tissues, organs, and disease states from images obtained by various medical imaging modalities.

Segmentation of medical images is a challenging task due to the complexity of the images and the absence of models of anatomy that fully capture the possible deformations in each structure. Also, due to the relatively low signal to noise ratios and inherent artifacts generally present in medical images, their segmentation is particularly difficult. Because of these problems, even though many algorithms have been reported, most of them have inconsistent results and/or limited applications. Thus, only a few algorithms are being used in practice.

Medical images, including CT, MRI, PET and SPECT data, add new complications to the problem of segmentation. Each modality has particular characteristics that detract from a straightforward solution. These difficulties range from the partial volume effects common to all modalities to RF inhomogeneities experienced by MRI, beam hardening effects of CT and scatter and attenuation problems common to PET and SPECT.

The main obstacles to segmentation of MR images are the presence of noise, errors in the scanners, and the structural variations of the imaging objects, which can be categorized into four different types : thermal/electronic noise, magnetic field inhomogeneities, biological tissue variations, and partial volume effects. The characteristics of some of the inherent shortcomings of MRI are described below.

Partial Volume Effect

All medical imaging modalities suffer from the partial volume effect to some extent. The measured value represents the average of the signal received through a section of tissue of specific thickness. Voxels may intersect more than one tissue type, depending on the area and the slice thickness realized. For example, a given voxel in a brain MR image may represent the attenuation through a volume of brain tissue measuring several cubic millimeters. Let us assume that this volume of tissue contains 40% gray matter and 60% white matter. If gray matter yields a value of 50 and white matter, 100, then the obtained value will be an average measurement representing the combined composition, i.e. 80, which is not an accurate representation of the underlying tissue. The extent of this problem depends upon the tissue resolution. The resolution obtainable with MRI is higher than that of CT, which in turn is more than that of PET and SPECT. Thus, the partial volume effect in MRI is not as pronounced as in the case of CT, PET and SPECT.

Radio Frequency and Magnetic Field Inhomogeneities

Slight fluctuations in either the radio frequency signal and/or the applied magnetic field during a MRI scan can result in what is termed as the *shading artifact*. This artifact, which was more pronounced in the early MRI machines, causes a subtle change in the average gray level of identical tissues from image to image. Methods have been developed to reduce this difficulty and have been incorporated into both the pre- and post-reconstruction phases of image creation.

Effect of Imaging Sequence

Different pulse sequences applied during a MRI scan result in varying tissue discrimination capabilities. If a scan relies primarily on the T1 component of the MRI signal, it is called an inversion recovery sequence. T1 images highlight the contrast between gray and white matter. Sequences which rely heavily on the T2 component of the MRI signal are known

as spin-echo sequences and produce images which are less clear anatomically. However, differentiation of subtle tissue pathology is easier with T2-weighted images.

T1 and T2 times determine the brightness of a pixel. For example, a tissue with a short T1 time shows up as bright in a T1-weighted image, whereas a short T2 time entails a dark zone in a T2-weighted image. Both types of sequences show the tumours well; on T1-weighted images, the tumours show up as dark areas and on T2-weighted sequences, as white areas. Normal tissues may appear differently on different scan sequences. However, fat is always bright due to short T1 and long T2 times. On the other hand, air, calcification and cortical bone are usually dark due to low hydrogen ion concentration. Rapid flow in healthy blood vessels results in no signal and thus, dark image areas.

Because of these differences in T1 and T2 scans, prior knowledge of the scan sequence type is necessary in order to interpret the results properly. These decisions must be made prior to imaging, depending on what needs to be emphasized or visualized in the scan.

4.4 Literature Survey

Brain matter, as assessed by magnetic resonance imaging, can generally be categorized as white matter, gray matter, cerebrospinal fluid and vasculature. Most brain structures are anatomically defined by boundaries of these tissue classes. Segmentation of tissues into these categories is an important step in quantitative morphology of the brain. MR image segmentation has been proposed for a number of clinical investigations, like measurements of tumor volume, evaluation of the therapeutic response (in a tumor), differentiation of tissues within tumors that have similar MR characteristics, planning of surgical procedures and neurological investigations. Automated segmentation and morphological measurements of brain tissues and structures may be a prelude to automatic identification of brain structures and functional divisions of the cortex, and complementary to brain functional studies. MR image segmentation can be roughly divided into two categories : a single image segmentation, where a $2D$ or $3D$ gray scale image is used and multi-spectral image segmentation, where multiple MR images with different gray scale contrasts are used.

Segmentation of MR images could be based on sets of features that can be extracted from the images, such as pixel intensities, edges and textures. Selection of good features is the key to successful segmentation. Based on feature selection, one or more features are used for segmentation. The focus of our work is neither feature extraction nor feature selection; hence we will not explore further on feature selection and extraction.

Currently available methods for MR image segmentation can be categorized into classical, statistical, fuzzy and neural network techniques [4, 21]. Classical approaches include the use of standard image processing techniques such as thresholding [64, 47], edge- and region- based techniques [57, 70]. Since classical methods do not employ *a priori* information, the final segmentation is sensitive to noise and may not result in continuous regions. The common intuitive approach to segmentation is global thresholding. Difficulty with this approach is determining the correct value(s) for the threshold(s). Knowledge or prior information based thresholding methods have been reported [103, 20, 54, 45, 63, 40], where a *goodness function* describing the separation of background, skull and brain, is used to determine global thresholds. This approach has limited application due to the wide variation in the anatomy being imaged by MRI.

Edge detection [75, 66, 12] methods suffer from incorrect detection of edges due to noise, over- and under- segmentation, and variability in threshold selection in the edge image [30, 91]. Morphological filtering followed by edge detection [90, 89] has also been reported [6]. Another method is boundary tracing [1], where the operator clicks a pixel in the region to be outlined and the method then finds the boundary starting from that point. This cannot, however, distinguish tissue types and is usually restricted to segmentation of large, well defined structures.

Seed growing methods have also been reported, where the segmentation requires an operator to empirically select seeds and thresholds. Pixels around the seed are examined, and included in the region if they are within the thresholds. Each added pixel then becomes a new seed.

Random field methods have been successfully applied, where an energy function is required to describe the problem [7, 55]; it is often very difficult to define the energy

fucntion, though.

Fuzzy segmentation techniques have not been applied for single-channel image segmentation although they have shown promise in segmenting multichannel images [9, 45, 71].

Supervised methods require a user supplied training set, usually obtained by drawing regions of interest on the images. Using Maximum Likelihood (ML) methods, where multivariate gaussian distributions are assumed [20, 45, 62, 40, 55], statistics like mean and covariance matrices are computed for the above regions. The remaining pixels are then classified by calculating the likelihood of each tissue class, and picking the tissue type with the highest probability. Parametric methods are useful when the feature distributions for different classes are well known, which is not necessarily the case for MR images [20]. k- nearest neighbourhood (k-NN) has given results superior, both in terms of accuracy and reproducibility, to parametric methods [20]. Artificial neural networks have also been used [20, 45, 29, 49, 48, 83, 73, 108].

All supervised methods are operator dependent. Inter- and intra- operator variabilities have been measured and shown to be relatively large [20, 40, 28]. This limits the use of supervised methods. Thus, unsupervised methods are preferred from the viewpoint of reproducibility.

Unsupervised techniques, also referred to as *clustering*, automatically find the structure in the data. A cluster is an area in the feature space with a high density. Clustering methods include k-means [4, 40, 103], and its fuzzy equivalent, fuzzy c-means [4, 45, 80]. These methods and their variants are basically limited to finding linearly separable clusters. Another promising development is using semi-supervised methods [2].

The expectation-maximization algorithm [31] has also been used for clustering MR images [109, 43], where the knowledge of tissue class is considered as the missing information. The method assumes a normal distribution, and incorporates an explicit bias field, which frequently arises in MR images.

Model based approaches, such as deformable models [28, 23] (also known as active contour models), minimize an objective function to obtain a contour of interest, especially if an approximate location of the contour is available. A deformable contour is a planar

curve that has an initial position and an objective function associated with it. A special class of deformable contours called *snakes* was introduced by Witkin [110]. Here, the initial position is specified interactively by the user and the objective function is referred to as the energy of the snake. The snake tries to minimize its energy over time, similar to physical systems. The balloon model for deformable contours is an extension of the snake model. It modifies the snake energy to include a *balloon* force, which can be either an inflation, or a deflation force. All these methods require an operator input to place the snake close to the boundary.

Validation of MR Image Segmentation

MR image segmentation is used to determine the volume of tissues in their 3D spatial distributions in diagnostic and therapeutic applications and surgical simulation protocols. Obviously, a quantitative measure of the accuracy and/or reproducibility of the proposed segmentation method is required. Since a direct measure of ground truth is not logistically feasible, or even possible with pathologic correlation, several alternative procedures have been used [8, 50, 11, 54, 40, 9, 58, 69, 1, 53, 22, 5, 72, 99, 77, 102, 112, 105]. Various validation methods used are :

- MRI contrast methods.
- Phantoms.
- MRI simulations
- Manual labeling of MR images.

4.5 Motivation for our Work

Brain tissue particularly has a complex structure, and its segmentation is an important step for the derivation of computerized anatomical atlases, pre- and intra- operative guidance for therapeutic intervention, clinical investigations, planning for surgical procedures and surgery simulations.

Segmentation of MR images is a difficult task because of the presence of noise, high variability among patients with respect to the anatomical structure of the brain, complex shapes of the anatomical structures, and variations in contrast. Manual segmentation is tedious, time consuming and subjective. Some of the images obtained from the neurocenter had low contrast. The differential contrast between tissues even in some normal subjects was very low making the differential study and manual segmentation difficult. These factors influenced us to think of enhancement schemes and further use enhanced images to get a clinically meaningful segmentation with reasonable computational cost and time.

In the next chapter, we propose three different schemes for enhancement. We also present the segmentation methods used in our study. The results of evaluation of the performance of the enhancement techniques are also presented. MR images, both original and enhanced, are segmented using five different approaches and the results are compared.

Chapter 5

MR Image Enhancement and Segmentation

5.1 Introduction

Image enhancement refers to accentuation or sharpening of image features such as edges, boundaries, or contrast. The enhancement process does not increase the inherent information content in the data, but it does increase the dynamic range of the chosen feature. Image enhancement includes gray level and contrast manipulation, noise reduction, edge crispening and sharpening, filtering, and pseudocoloring. The difficulty associated with image enhancement is the absence of any quantifiable criterion. Therefore, a large number of image enhancement techniques are empirical and require interactive procedures to obtain satisfactory results. Some of the common enhancement techniques are

- Point Operations
  - Contrast stretching, Noise clipping, Window Slicing, Histogram Modeling
- Spatial operations
  - Noise Smoothing, Median Filtering, Unsharp Masking, Zooming
- Transform operations

  - Linear filtering, Root filtering, Homomorphic filtering

- Pseudocoloring

  - False coloring, Pseudocoloring

Image enhancement can be performed either globally or locally. Global methods operate similarly on all the pixels in the image. They may be independent of the pixel values in an image, or may reflect statistics calculated from all the pixels. A local method operates based on the values of the current pixel and its neighbours. A local operation can be adaptive because results depend on the particular pixel values encountered in each image region. A typical application of a global operation is to increase overall image contrast or brightness, whereas local operations are used to preferentially enhance certain regions of low contrast or brightness, without affecting other regions.

Although a particular task often can be addressed by either a global or a local operation, there is an overriding trade-off between the two approaches. The user must choose the operation to be used based on experimentation or by the knowledge of the problem.

Requiring no location-dependent computation, global operations are generally simpler to implement, but are also less flexible than local operations, which provide adaptive image modification. Since global operations treat all pixels equally, some of the image regions may be affected. For example, a global increase in brightness will cause dark regions to be more visible, but may cause very bright regions to be clipped at the top range of brightness. Global operations use the statistics of the entire image, and thus, may average the local features. Noise effects are reduced, but features associated with a desired signal are also averaged. This is acceptable only if a single type of signal is distributed uniformly throughout the image. It may not perform well when nonuniform distribution of signals is present.

A useful initial characterization of an image may be based on statistics derived from the entire set of constituent pixels. These descriptors, constructed from an intensity histogram of the image, are referred to as global features. The intensity histogram is a plot of the frequency of occurrence (in terms of the number of pixels) of each of the possible

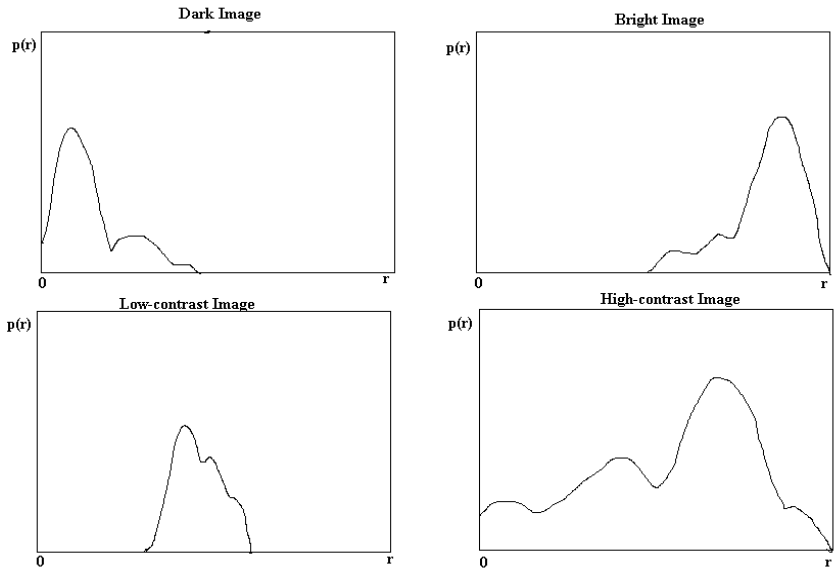

Figure 5.1: Histograms of different types of images

discrete intensity values. In statistical terms, histogram is a distribution of sample values for a population of intensities. Histogram for four different types of images are shown in Fig. 5.1.

The most basic feature is the average pixel value $\overline{I}$, which is a measure of image brightness. A second feature is the spread or variance of pixel values about the mean. Variance is a measure of image contrast : narrower the spread, lower the contrast. Such global features can conveniently be determined from the histogram. Another useful feature is the range, defined as the difference between the maximum and minimum pixel value in the image. Range serves as a feedback in the image acquisition stage to attain a good quality image. The entropy of a histogram is a measure of the global information content of an image in terms of average bits per pixel. For an eight-bit image, an entropy value approaching 8 indicates rich information; a value near 0 indicates the presence of predominating regions that have little variation in pixel values.

We initiated our study by exploring the properties of various MR images acquired from the routine scans. Many of the images were having low contrast as shown in Fig. 5.2. Contrast, in medical imaging, is defined as the relative difference of intensities of two adjacent regions within an examined object on a gray or colour scale. A quantitative definition of contrast (C) is given by the following equation:

$$C = \frac{(Ia - Ib)}{(Ia + Ib)} \tag{5.1}$$

where Ia and Ib are the signal intensities of two adjacent pixels or voxels.

In MRI, the intensity of the image is not standardized [88]. The signal intensity of a MR image can represent a mixture between T1, T2 and ρ values. In addition, factors such as flow, diffusion and perfusion influence the signal emitted by structures within a volume element. Thus, the comparison of signal intensities of two different images is meaningless and cannot be used for clinical diagnosis. Normalization of images (e.g. with a water filled vial outside the patient's body) allows an approximation that can be used to calculate relative signal intensities, which then can be compared. However, these values are semiquantitative. They also differ between different MR equipment and so have limited diagnostic value.

Contrast in conventional radiographs and computed tomography images is essentially based on small density differences and can only be changed by adding contrast agents. The contrast of MRI is influenced by more factors than other imaging methods. More information is encoded in MR images compared to other imaging modalities. This makes the contrast behaviour of MRI more complex than that of any other medical imaging modality. The numerous factors influencing contrast can be divided into two groups: the *intrinsic* and *extrinsic* parameters. Table 5.1 lists these parameters. Many *extrinsic* factors directly influence the *intrinsic* factors. For the clinical application of MRI, it is necessary to be aware of the influences of these factors, if one is to react rapidly and efficiently in a diagnostic question.

One of the main advantages of MRI is the possibility of changing contrast by choosing special pulse sequences and their parameters. By emphasizing one factor or mixing several factors in a specific way, the contrast behaviour of a certain morphologic region

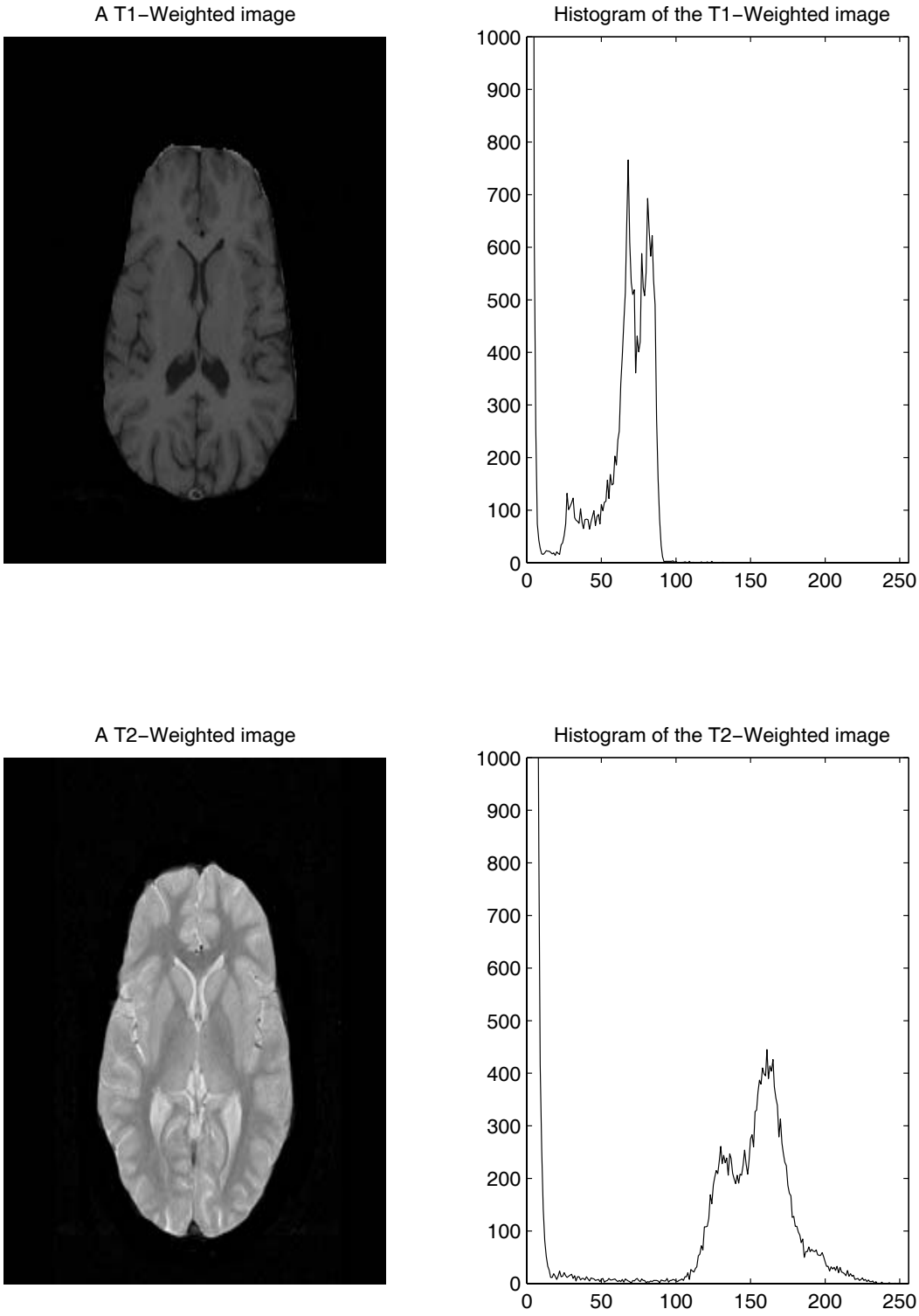

Figure 5.2: Samples of MR images used in the study and their histograms

Factors influencing the contrast of a MR image	
Intrinsic factors	
1. Proton Density	• slice orientation
2. T1 Relaxation	• number of averages
3. T1 -ρ Relaxation	• pulse shape/bandwidth
4. T2 Relaxation	• pixel size
5. Cross Relaxation	• matrix size
6. Dia- and ferromagnetic perturbations	• field of view
7. Chemical shift	• acquisition mode (2-/3-D)
8. Temperature	• artifact suppression
9. Diffusion	• triggering/gating
10. Perfusion	• orientation of phase vs.
11. Physiologic motion	frequency encoding gradients
12. Bulk flow	3. RF sequences
13. Viscosity	• saturation recovery/ partial saturation
14. Changes of tissue composition (e.g. age)	• inversion recovery
Extrinsic factors	• spin echo
1. Magnetic field strength	• rapid sequences
• static field	4. Pulse sequence parameters
• gradient field	• repetition time
2. Magnetic field inhomogeneity	• echo time
3. Hardware & software parameters	• inversion time
• type of coil	• flip angle
• number of slices	5. Contrast changing agents
• slice thickness and gaps	

Table 5.1: Factors influencing the contrast of a MR image

or pathological lesion can be highlighted. However, two images of the same patient taken with two different imagers using the same parameters can have different contrast.

When analyzing the brain MR images obtained in a study of normal subjects at the neurocenter, some of the images were found to be of very low contrast. It was difficult to quantify the various regions in the images. Samples of such low contrast images and their histograms are shown in Fig.5.2. The figure also shows how the three major tissue components of the brain, namely, gray matter, white matter, and the cerebrospinal fluid (CSF) manifest differently in the T1- and T2- weighted images. The details of how these tissues are distributed in the gray scale are illustrated in Table 5.2. Figure 5.3 shows the

Gray Scale	PD – weighted	T1 - weighted	T2 – weighted
	Gray and White matter	Fat Bone marrow	CSF
	Fat	Gray and White matter	Gray and White matter
	CSF	CSF	Fat
	Cortical bone and flowing blood	Cortical bone and flowing blood	Cortical bone and flowing blood

Table 5.2: Signal intensity of different components on the gray scale

distribution of the characteristic values of these tissues in terms of T1, T2 and PD.

The enhancement of contrast between the different tissue types was formulated as an objective in our study, while preserving the overall shape of the histogram. In the pursuit of realization of the objective, various enhancement methods, based on linear and nonlinear transformations, were explored. We have formulated three enhancement techniques based on entropy measures and polynomial transformation. The details of the proposed enhancement techniques are described in section 5.3.

5.2 Data Collection

The images used in our study were obtained from National Institute of Mental Health and NeuroSciences (NIMHANS), Bangalore. T1- and T2-weighted images were acquired from a 1.5 Tesla Siemens MRI system. The imaging protocol included spin-echo (SE), T1-weighted sequences [TR/TE/1 = 650/15/1] and turbospin echo (TSE), T2-weighted

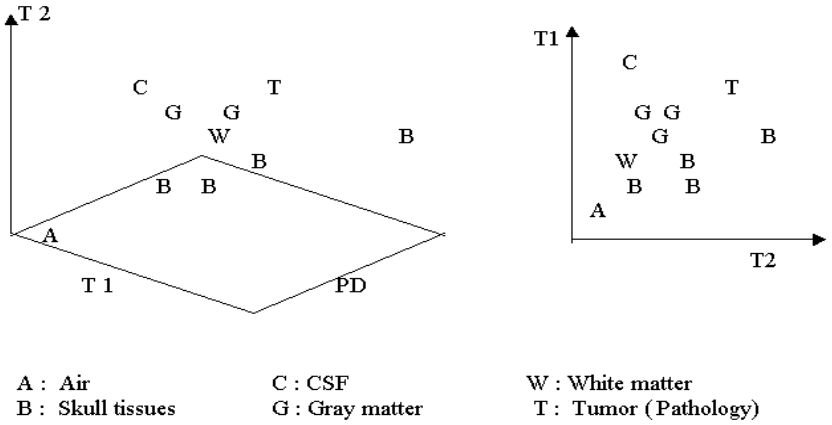

Figure 5.3: Distribution of different components of brain on T1-, T2- and PD weighted scale

sequence [TR/TE/1 = 5500/22,90/1] in axial planes. A field of view (FOV) of 230-250 and a matrix of 256×256 was employed for these sequences. An inversion recovery sequence FLAIR (Fluid Attenuated Inversion Recovery) [TR/TE/1 = 9000/120/1] was also performed in axial plane. The flip angle for TSE-T2 and FLAIR sequences was 180° and 70° for T1-weighted sequence. More than 150 images were used in the study. The slices were of 3 mm thickness, with a separation of 1 mm between the slices. Each pixel in the image represents an area of $0.95mm \times 0.95mm$. The slices were taken at ventricular, subventricular and supraventricular sections. All the images obtained from the Siemens system, though of 12-bit resolution, had a dynamic range of around 10 bits only. Initially segmentation was carried out on these 10-bit images, and the results showed no improvement over the results obtained with images scaled down to 8-bit resolution. Further, since the monitors we used could display only 256 gray levels, neither the original 10-bit images, nor any of the intermediate results could be viewed on the screen. Hence, the images were converted to 8-bits by linear transformation. The nature of the histogram was preserved during the conversion. The scans interpreted as normal by the neuroradiologists were used for both enhancement and segmentation studies. However, the enhancement schemes were also explored on a few pathological MR and x-ray CT images.

5.3 Proposed Enhancement Techniques

Entropy is a measure of the average amount of information present or the degree of uncertainty of the random variable. Consider a random variable X, which can take values $x_1, x_2, x_3, \ldots, x_N$ with probabilities $p(x_k), k = 1, 2, \ldots, N$. The information associated with x_k is defined as

$$H(x_k) = -\ln \ p(x_k) \tag{5.2}$$

If we know that the event x_k occurs with probability $p_k = 1$, then there is no information contained in X, since we know the outcome exactly. The Shannon's [94, 95, 56] entropy of a source (such as an image, I) is defined as the average information generated by the source, i.e.

$$Entropy = E(I(x_k)) = H_S(X) = -\sum_k p(x_k) \ \log \ (p(x_k)) \tag{5.3}$$

Digital image can be considered as a source of independent pixels, and its entropy can be estimated from its histogram. There are other entropy measures which are also quite useful. One of them is Renyi's entropy measure [87], which is defined as

$$H_R(X) = \frac{1}{1-\alpha} \ \log \ \sum_{k=1}^{N} p(x_k)^{\alpha}, \qquad \alpha > 0, \ \alpha \neq 1 \tag{5.4}$$

The entropy measures are global features and have a single value for the entire image. The nonlinear transformations proposed on the lines of Shannon and Renyi's entropy measures for enhancement of MR images are described in the following subsections.

5.3.1 Weighted Nonlinear Method (WNM)-1

This method is based on the Shannon's entropy relation. We have made use of the pixel intensities as the variable instead of the probability measures of the pixels. The method is a point-based global method, since it operates similarly on each pixel of the image. The enhanced value of the pixel $Y_s(x_k)$, corresponding to an input pixel value x_k is given by,

$$Y_s(x_k) \ = \ x_k \ \log \ (x_k) \tag{5.5}$$

The processed pixels are then normalized to have the gray values between 0 to 255. The algorithm for the implementation of enhancement method based on Eqn. 5.5 is as follows.

Algorithm:

- Begin

  Read image : $orgimg(i,j) = img$;

  Convert into data vector $datvec \leftarrow orgimg$;

  If $datvec(i) == 0, \quad datvec(i) \;\; == \;\; \epsilon$;

  for $i = 1 \;\; to \;\; M \times N$

  Compute $Shdatvec(i) = datvec(i) * \log\left(datvec(i)\right)$

  end

  Normalize :

  $Minval =$ min $(Shdatvec)$

  $Enhdatvec =$ Integer $\left[\left(\frac{Shdatvec}{Minval}\right) * 255\right]$

  Convert data vector to image

  $Enhimg =$ Reshape $(Enhdatvec, M, N)$

- End.

The pixels having *zero* intensity value are replaced by a small value ϵ, for logarithm calculation. Enhancement can be controlled by suitably changing the base of the logarithm. Figures 5.4 and 5.5 show the histograms of the original and the resulting enhanced image, respectively. A considerable amount of enhancement is obtained if the gray values of the original image do not cover the entire gray scale. This method has worked better with T1-weighted images than T2-weighted ones, as in the latter case, the pixels corresponding to CSF have intensity values close to the upper limit of the gray scale and the background of the image has values near the lower limit of the gray scale. The results of enhancement based on Eqn. 5.5 are given in Figs. 5.6 and 5.7.

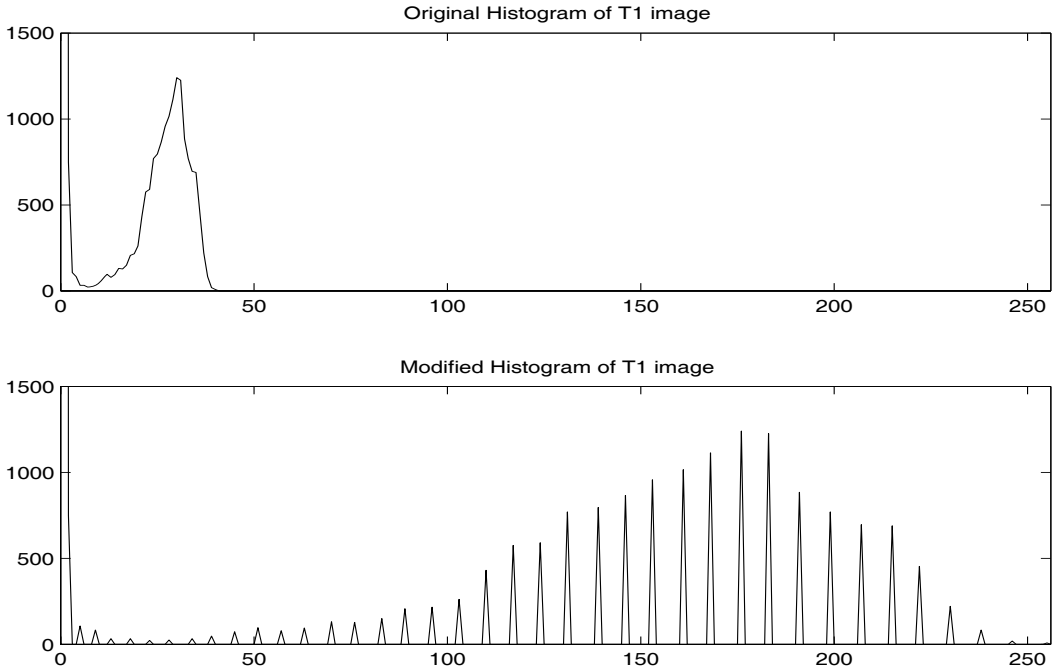

Figure 5.4: Histograms of original (T1) and WNM-1 enhanced images

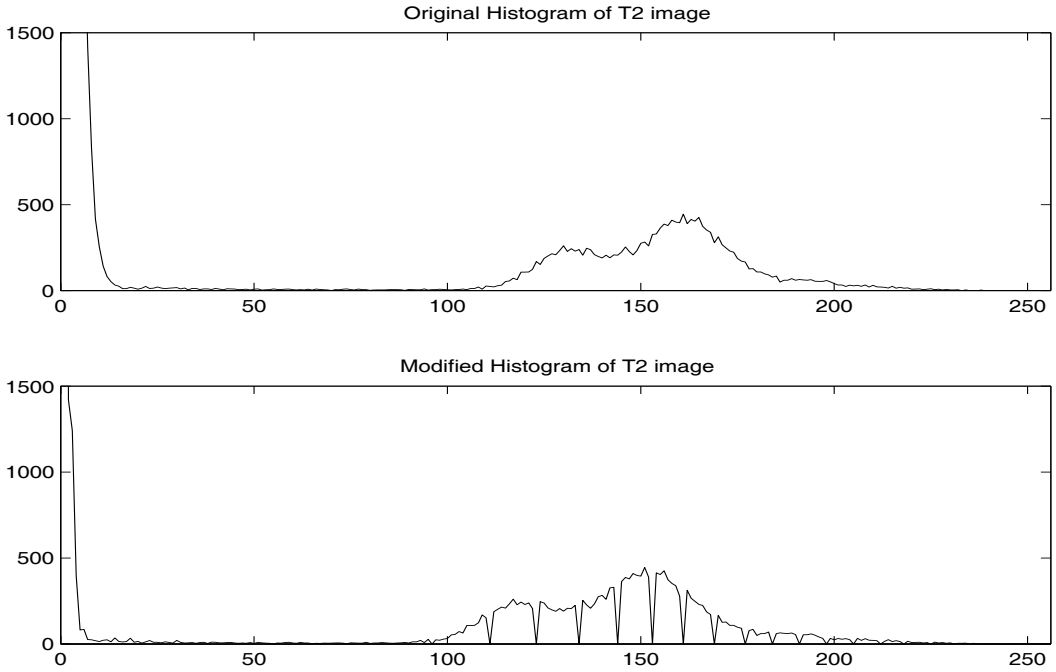

Figure 5.5: Histograms of original (T2) and WNM-1 enhanced images

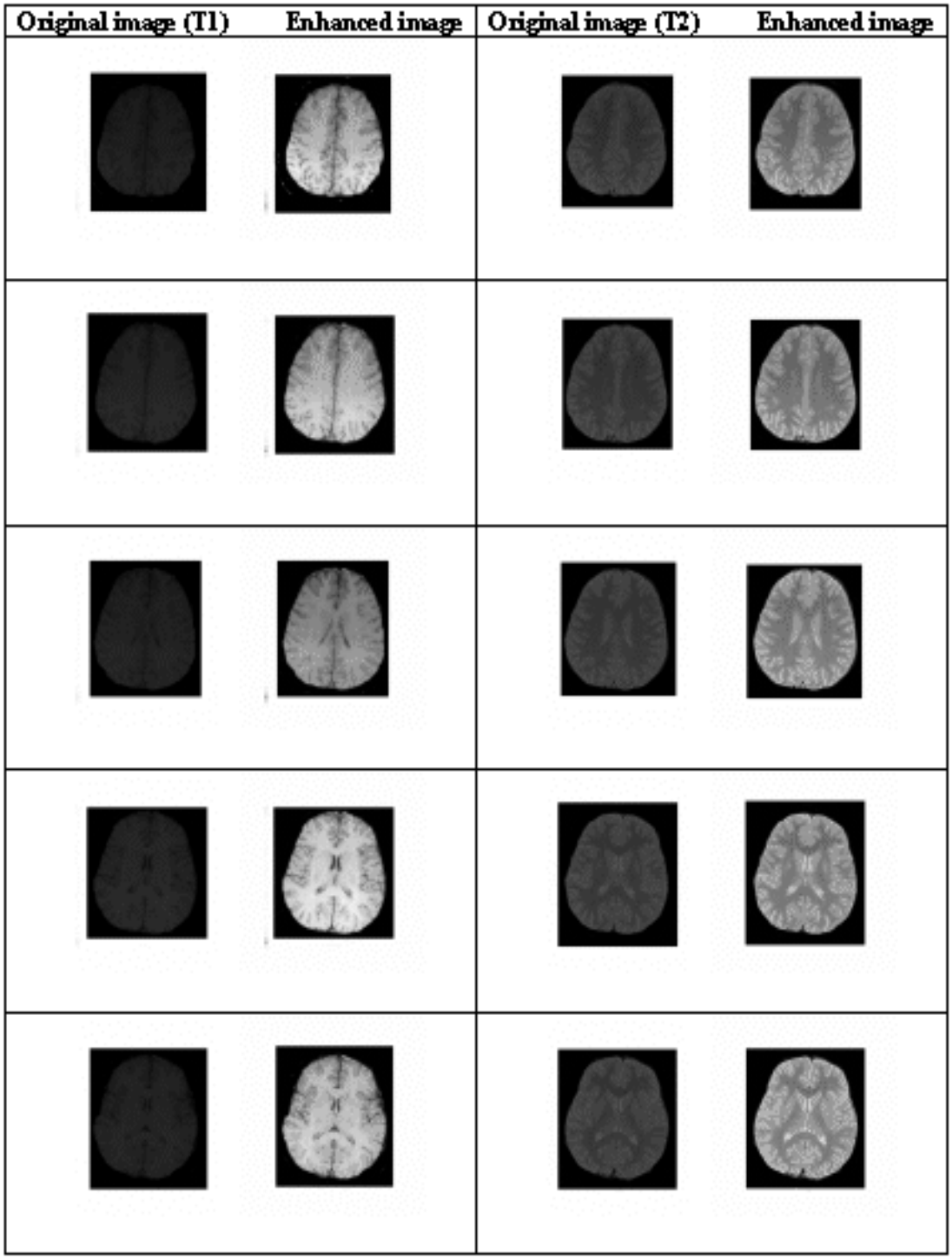

Figure 5.6: Original and WNM-1 enhanced images

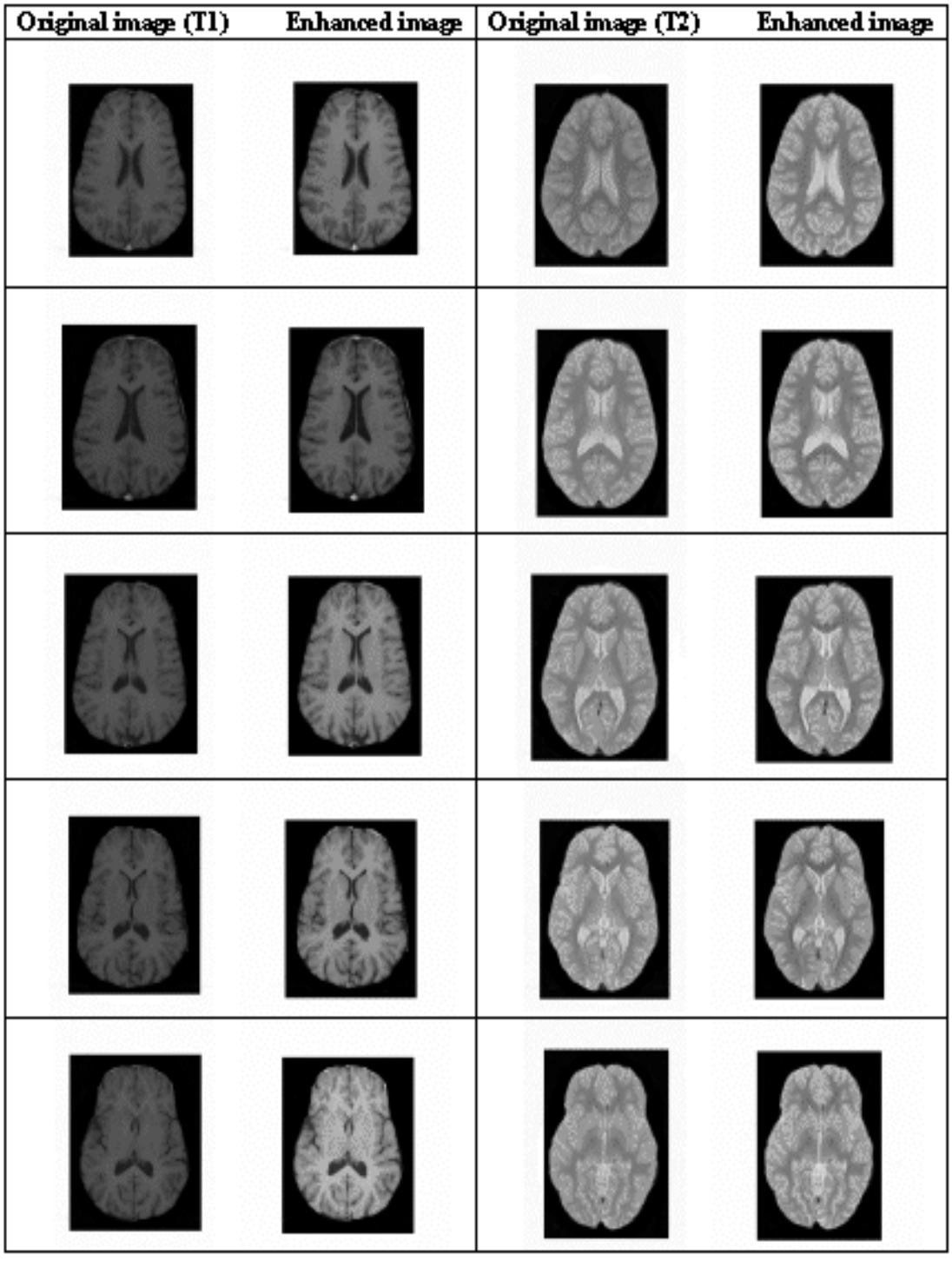

Figure 5.7: Original and WNM-1 enhanced images

5.3.2 Weighted Nonlinear Method (WNM) -2

A neighbourhood based formulation was used in this method. A 3×3 window was selected for processing. The input image is suitably appended with rows and columns to carry out the processing on the entire original image. This is also a global method, as each pixel is modified in a similar fashion. The transformation equation is based on Renyi's entropy relation (Eqn. 5.6) and is defined as follows:

$$Y_r(x_k) = \frac{1}{1-\alpha} \log \sum_{k=1}^{N_r} {x_k}^{\alpha}, \quad \alpha > 0, \ \alpha \neq 1 \tag{5.6}$$

where $Y_r(x_k)$ is the processed intensity value

x_k is the original intensity value,

and $N_r = 9$, is the No. of pixels in the window considered

The transformed image is weighted by the respective intensity values of the original image and then normalized. The algorithm for enhancement based on equation 5.6 is as follows.

Algorithm:

- Begin

  Read image : $orgimg(i,j) = img;$

  Append the image ($orgimg$) with appropriate number of columns and rows of zeros depending on the size of the window selected. (e.g 2 rows and 2 columns for 3×3 window) .

  $Intimg = Append\,[zeros(M,1) \quad orgimg \quad zeros(M,1)]$

  $$Intimg = Append \begin{bmatrix} zeros(1, N+2) \\ Intimg \\ zeros(1, N+2) \end{bmatrix}$$

  Convert into data vector $datvec(i,k) \leftarrow Intimg;$

If $datvec(i,k) == 0, \quad datvec(i,k) \;\; == \;\; \epsilon;$

for $i = 1 \;\; to \;\; M \times N$

$val \;\; = \;\; 0$

for $k = 1 \;\; to \;\; N_r$

Compute :

$val1 \;\; = \;\; datvec(i,k)^2$

$val \;\; \leftarrow \;\; val \;\; + \;\; val1$

end

$Enhdatvec(i) \leftarrow \log(val)$

end

Compute :

$Maxval =$ max $(orgimg)$

$Enhimg =$ Reshape $(Enhdatvec, M, N)$

$Enhimg = Enhimg * \left[\frac{orgimg}{Maxval}\right]$

Normalize :

$Enhimg = Integer \left[\frac{Enhimg}{max(Enhimg)} \times 255\right]$

- End.

Histograms of the enhanced T1- and T2-weighted images are given in Figs. 5.8 and 5.9. The images enhanced based on the above algorithm are shown in Figs. 5.10 and 5.11. We propose a polynomial based enhancement method in the following section.

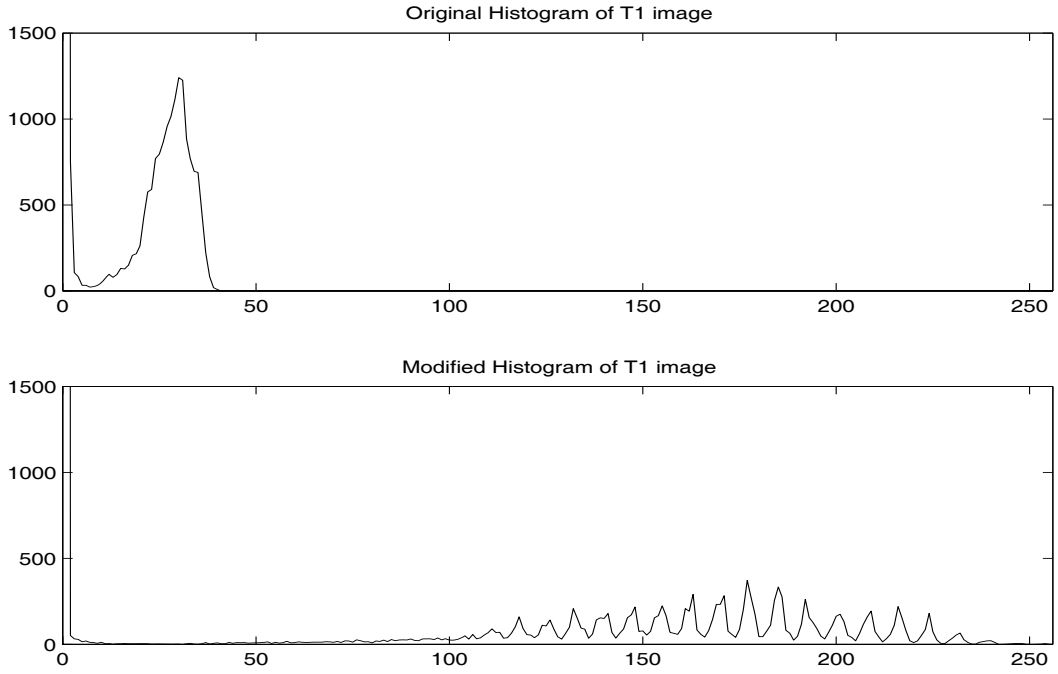

Figure 5.8: Histograms of original (T1) and WNM-2 enhanced images

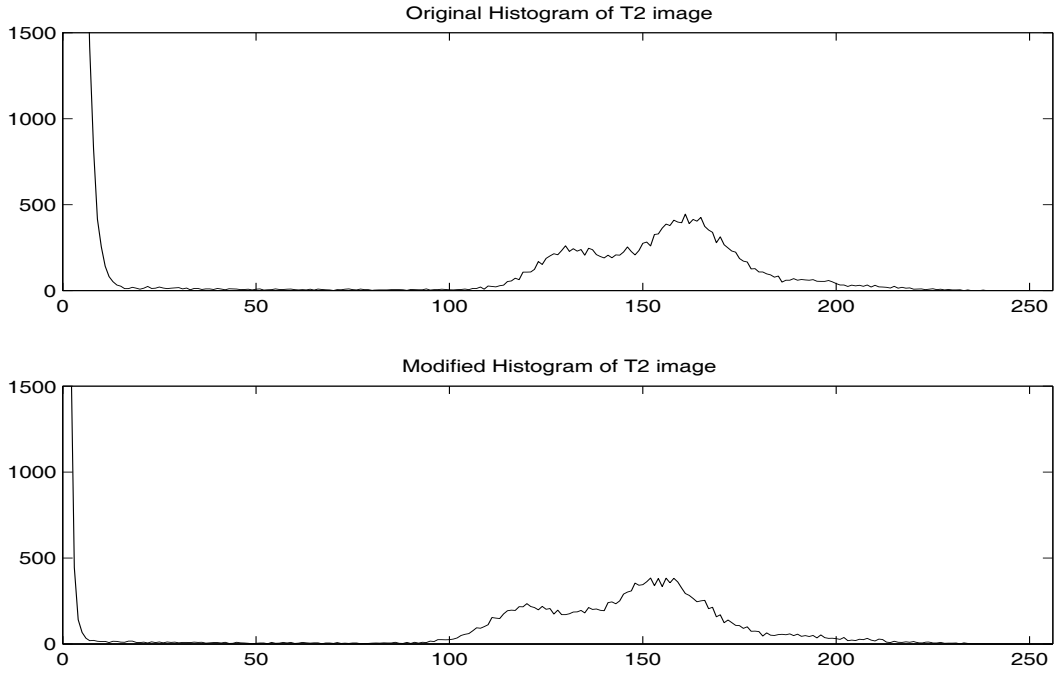

Figure 5.9: Histograms of original (T2) and WNM-2 enhanced images

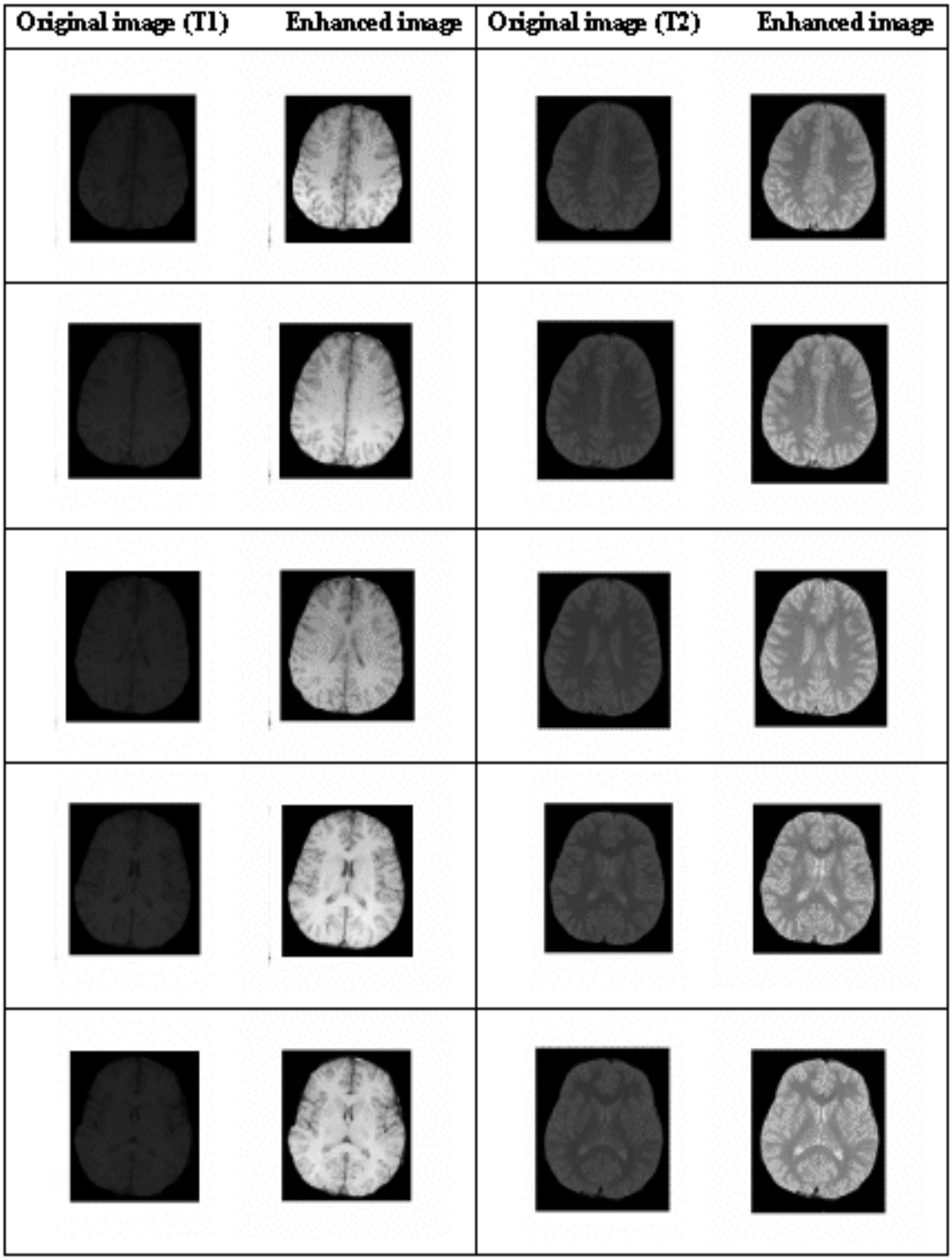

Figure 5.10: Original and WNM-2 enhanced images

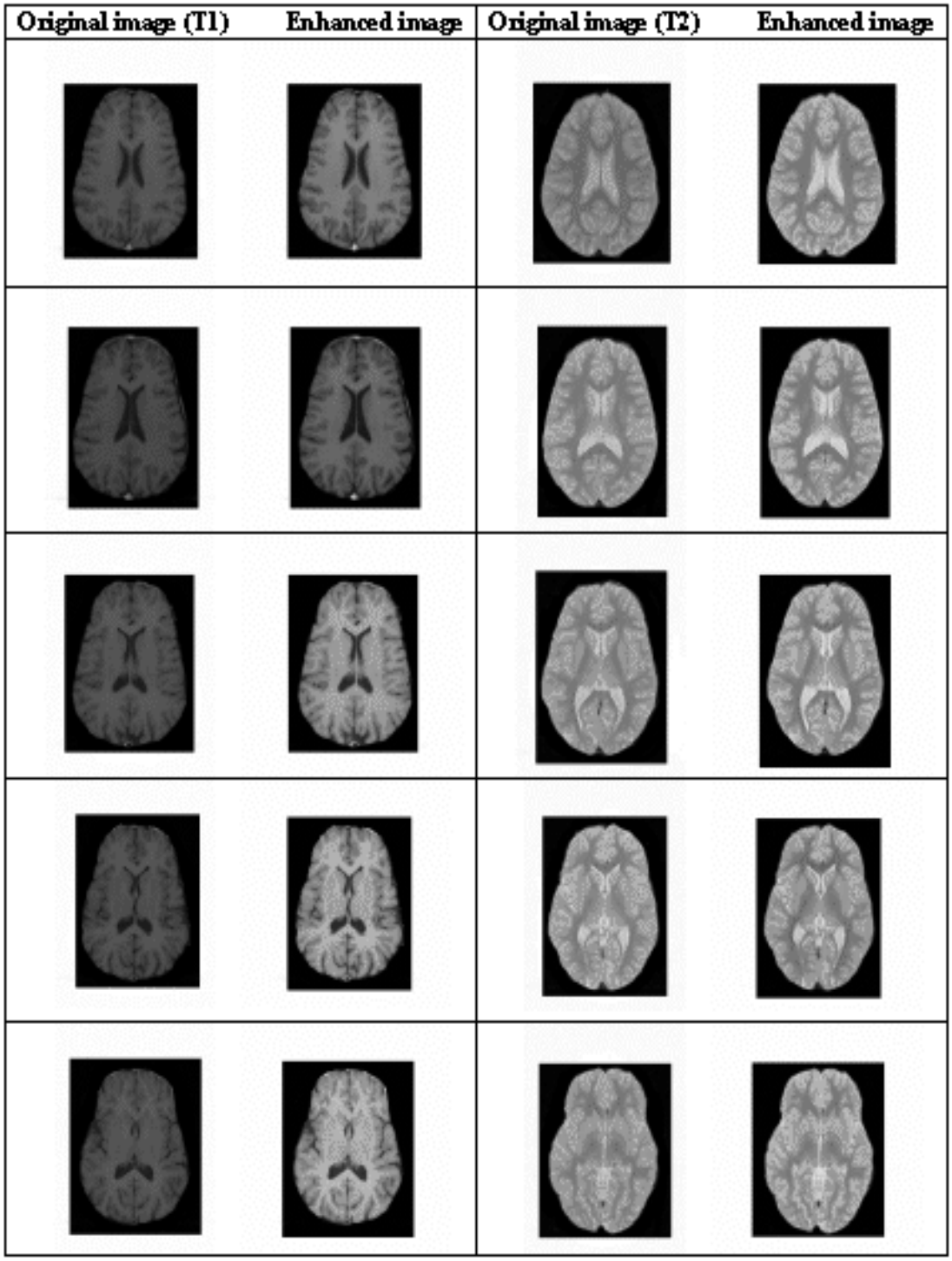

Figure 5.11: Original and WNM-2 enhanced images

5.3.3 Polynomial based Approach

Polynomial methods are useful for enhancing the image contrast, when the histogram stretching is to be carried out around a particular value of the input intensity. Specifically, the mapping function will stretch the given range of input intensities into a wider range of output intensities.

Given a range of input intensities, $x \in [x_{min}, x_{max}]$, and output intensities, $y \in [0, y_{max}]$, and the point $x = x_c$, at which the histogram is to be stretched, a third-order polynomial [93] can be specified to meet this criteria, mapping the input intensities x to output intensities y according to,

$$y(x) = Ax^3 + Bx^2 + Cx + D \tag{5.7}$$

where

$$A = \frac{1-m}{x_{max}^2 - 3x_c x_{max} + 3x_c^2} \tag{5.8}$$

$$B = -3Ax_c \tag{5.9}$$

$$C = m + 3Ax_c^2 \tag{5.10}$$

$$D = 0 \tag{5.11}$$

The values of A, B, C *and* D are calculated using the initial conditions,

$$\begin{aligned} y(0) &= 0, \quad \text{the lowest intensity value} \\ y(x_{max}) &= y_{max} = x_{max} \ \text{(i.e maximum of X and Y are usually 255)} \\ \dot{y}(x_c) &= \frac{dy}{dx} = m \\ \ddot{y}(x_c) &= \frac{d^2y}{dx^2} = 0 \end{aligned} \tag{5.12}$$

where m is the slope that defines the region of the histogram transformation around x_c, which should be symmetric. The second derivative, $\ddot{y}(x_c)$ or slope of the slope at x_c should be zero (inflection point), because it is the central intensity value around which the transformation takes place.

The value of $y(x)$ needs to be limited to a range of output intensities between 0 and

y_{max}. However, when the actual intensity values produced by the mapping function exceed y_{max}, the output range must be artificially clipped at y_{max}, and this clipping often leads to an undesirable appearance. The severity of clipping can be reduced by a gradual tapering toward upper and lower bounds; this is achieved by a ramp function of the form

$$\text{lower bound: } y_{lower}(x) = kx \tag{5.13}$$

$$\text{upper bound: } y_{upper}(x) = k(x - x_{max}) + y_{max} \tag{5.14}$$

where k is the slope of the ramp (adjustable parameter)

The severity of clipping is reduced when k is increased from zero, but as k approaches one, the range of contrast enhancement is narrowed, and the overall effect of the transformation is diminished, eventually leaving the image unaltered. A typical value of k is 0.2.

Taking into account the tapered bounds, the mapping function may be defined in the following form:

$$y = \begin{cases} y_{lower}(x) & : \quad y(x) < y_{lower}(x) \\ y_{upper}(x) & : \quad y(x) > y_{upper}(x) \\ y(x) & : \quad otherwise \end{cases} \tag{5.15}$$

This mapping function is shown in Fig. 5.12 for low, medium and high values of x_c. Typical value for the slope of the mapping function is $m = 2$.

Modifications are done in the selection of the polynomial parameters for the MR image data. Details of the modifications are given in the subsequent paragraphs.

The input images are used in the estimation of the control point (x_c). Figure 5.2 shows the histograms of the sample images. The histograms have clearly two distinct regions which are well separated. The peaks of the gray levels correspond to the background region of the MR image and the brain region. The background of the image has gray values in the range 0 to 20. By selecting a threshold value of 20, the background region of the MR images was removed. A gaussian mixture model was used to model the histogram of the background-free image. The overall density function (histogram) is the sum of two

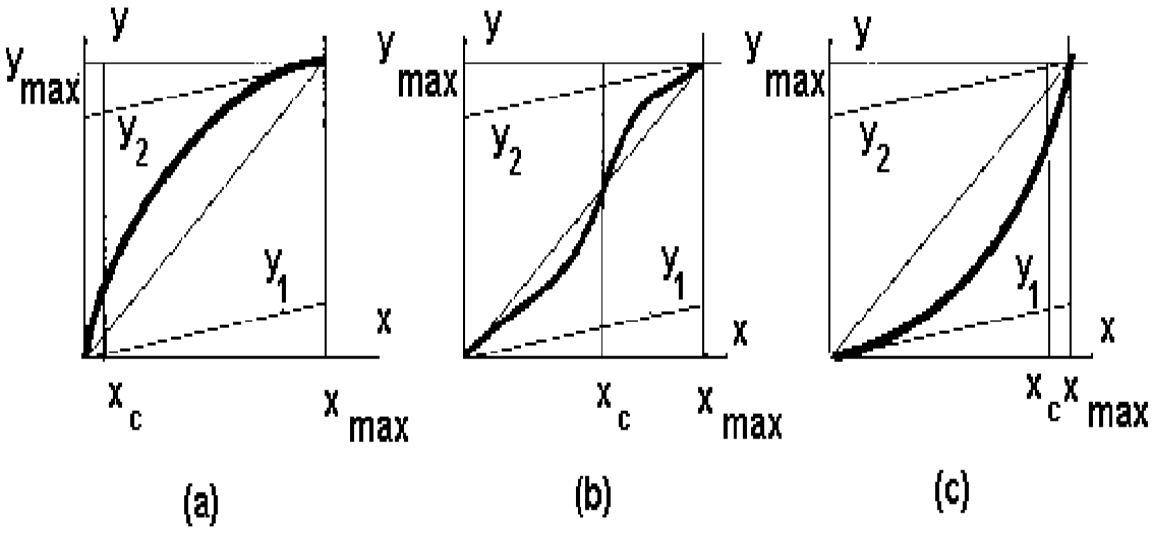

Figure 5.12: Polynomial mapping function to enhance (a) low intensities (b) middle intensities and (c) high intensities

unimodal densities. The mixture probability density function is defined as

$$p(z) \;=\; w_1\, p_1(z) \;+\; w_2\, p_2(z) \tag{5.16}$$

and for the Gaussian case, is

$$p(z) \;=\; \frac{w_1}{\sqrt{2\pi}\sigma_1} \exp\left[-\frac{(z-\mu_1)^2}{2{\sigma_1}^2}\right] \;+\; \frac{w_2}{\sqrt{2\pi}\sigma_2} \exp\left[-\frac{(z-\mu_2)^2}{2{\sigma_2}^2}\right] \tag{5.17}$$

where μ_1 and μ_2 are the mean values of the two brightness levels of the histogram, σ_1 and σ_2 are the standard deviations about the means, and w_1 and w_2 are the weights with which the gaussian functions are combined, subject to the condition,

$$w_1 \;+\; w_2 \;=\; 1 \tag{5.18}$$

The mean and variance parameters of the gaussian mixture model were estimated using the Expectation-Maximization technique. The value of x_c is calculated as follows:

$$x_c \;=\; \frac{\mu_1\sigma_2 \;+\; \mu_2\sigma_1}{\sigma_1 \;+\; \sigma_2} \tag{5.19}$$

Algorithm for the polynomial based enhancement is given below.

Algorithm :

- Begin

  Read image: $orgimg(i,j) = img$;

  Compute the histogram : $orghist \leftarrow Histogram\ (orgimg)$

  From the histogram find the maximum peak point which corresponds to background of the image.

  Assign : $B_{th} \leftarrow$max value of the background pixels

  Form a data vector with background pixels removed.

  $datvec \leftarrow orgimg$ (find $(orgimg > B_{th})$)

  Using the gaussian mixture model, estimate the mean and variance of the $datvec$, assuming a normal distribution of the data.

  Find the indices of the pixels which are less than B_{th}

  $[rowind\ \ colind] =$ find $(orgimg < B_{th})$

  Assign :

  $maxval \leftarrow 1.2 \times max(orgimg)$

  Output maxval : $(Y_{max}) = 255$;

  Output minval : $(Y_{min}) = 0$;

  Slope at the control point : $m = 2$

  Compute :

  Control Point : using Eqn. 5.19

  Coefficients :- $A,\ B,\ C,\ and\ D$ using Eqns. 5.8 to 5.11 respectively.

  Polynomial :-

  $outdatvec = A\ datvec^3 + B\ datvec^2 + C\ datvec$

$$outdatvec = \begin{cases} Y_{min} & : \quad outdatvec < Y_{min} \\ Y_{max} & : \quad outdatvec > Y_{max} \end{cases}$$

  Normalize:

  $Newmin =$ Min $(outdatvec)$;

  $Newmax =$ Max $(outdatvec)$;

If $Newmin > Y_{min}$ and/or $Newmax < Y_{max}$ then

$$outdatvec = \frac{outdatvec - Newmin}{Newmax - Newmin} * (Y_{max} - Y_{min})$$

Convert :

$Enhimg \leftarrow$ Reshape $(outdatvec,\ M,\ N)$

- end

The histograms of the enhanced T1- and T2-weighted images are given in Figs. 5.13 and 5.14. The enhanced images are presented in the Figs. 5.15 and 5.16.

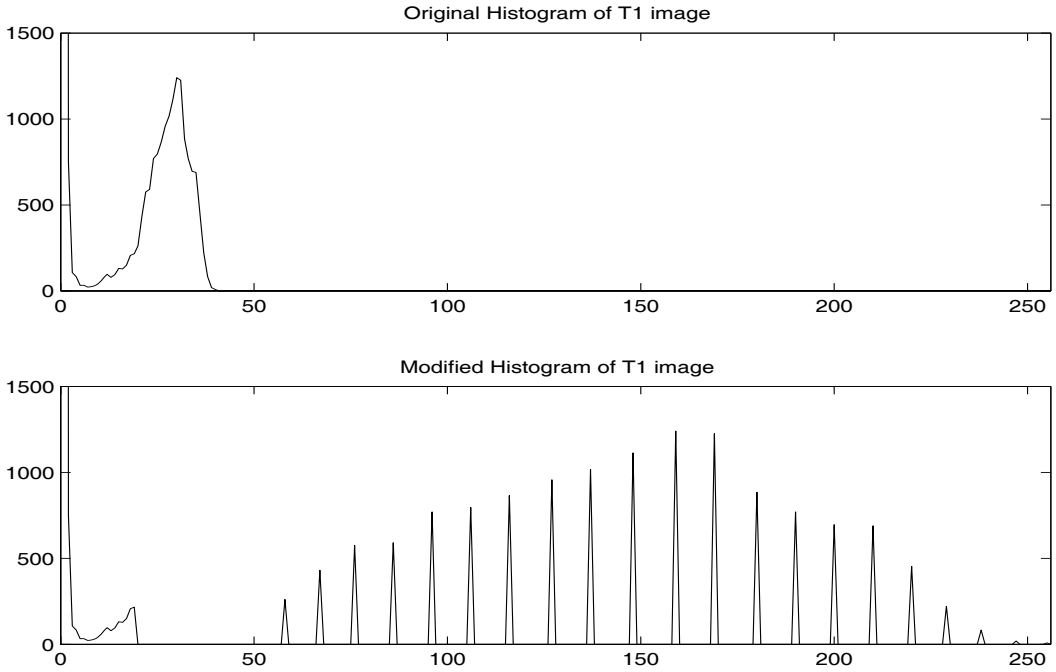

Figure 5.13: Histograms of original (T1) and polynomial enhanced images

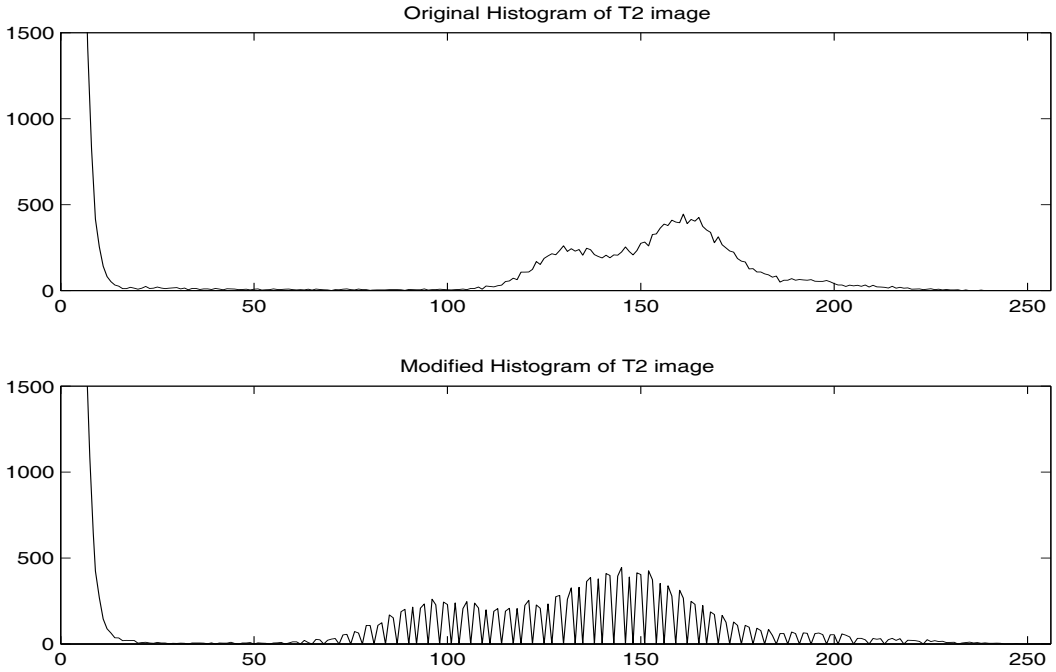

Figure 5.14: Histograms of original (T2) and polynomial enhanced images

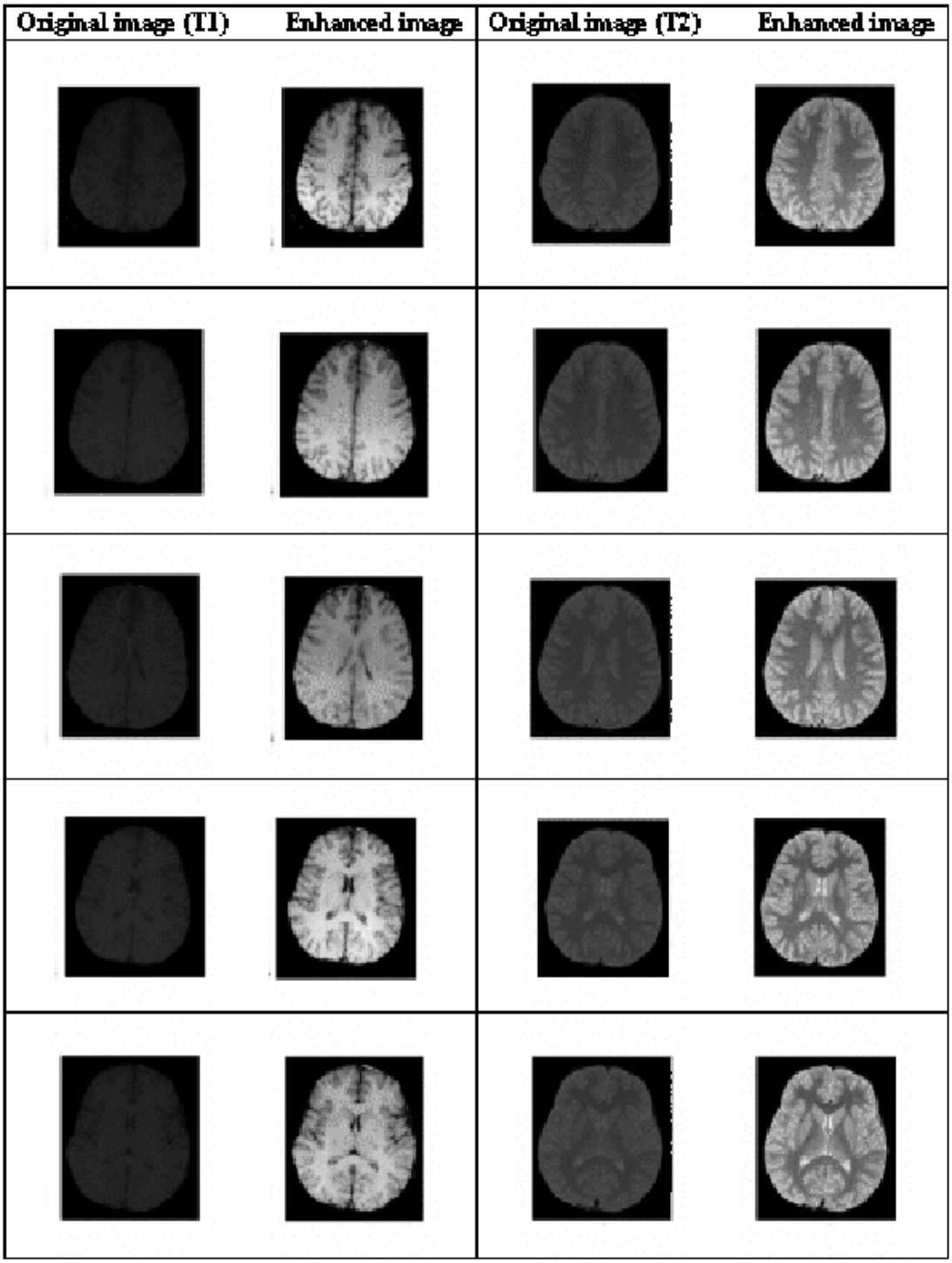

Figure 5.15: Results of polynomial enhancement - images from normal subjects

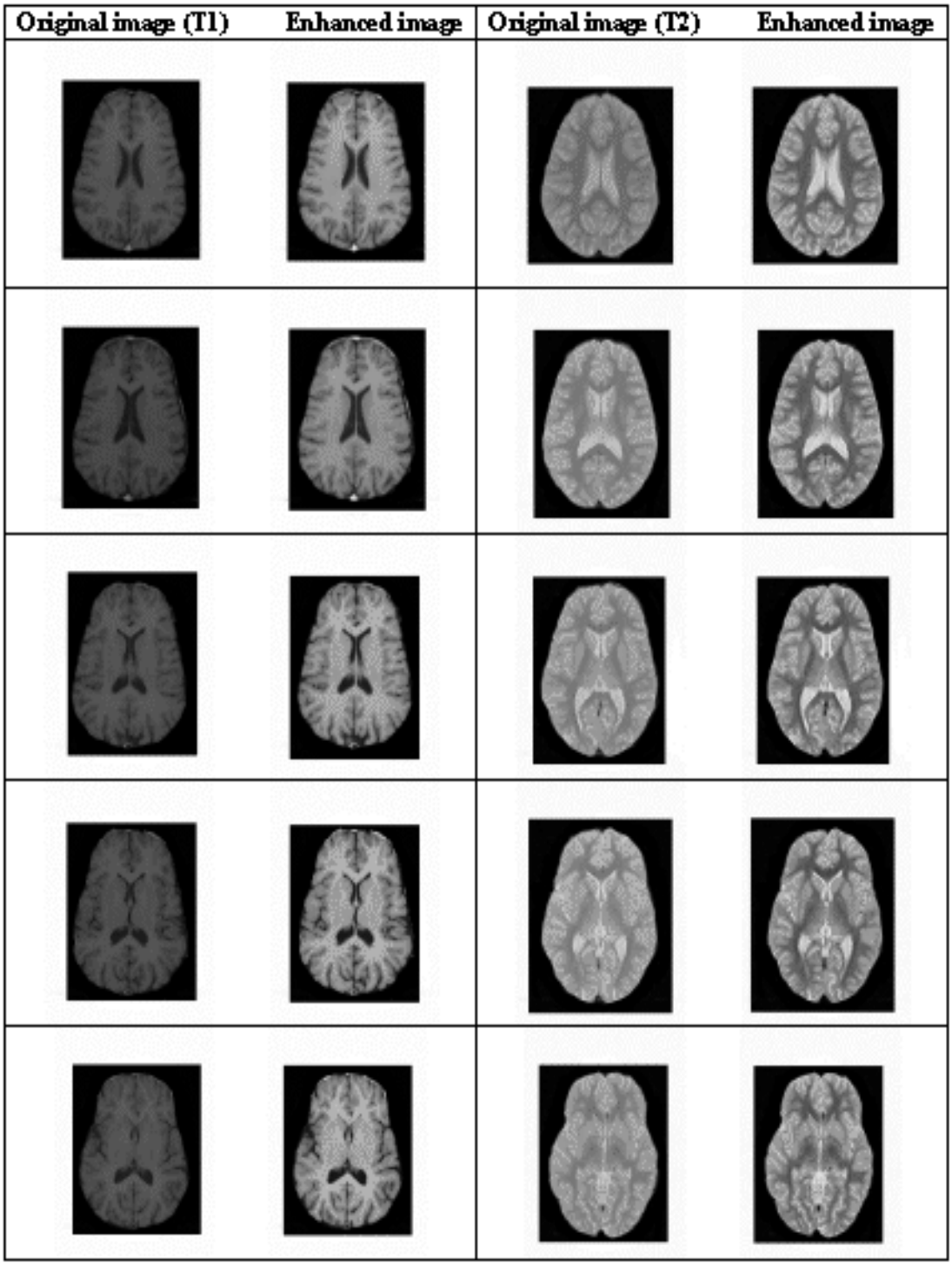

Figure 5.16: Results of polynomial enhancement of images from normals-contd.

5.4 Evaluation of Proposed Enhancement Techniques

A total of 120 images were used to evaluate the proposed methods. The data set contained axial slice images at various depths (subventricular, ventricular and supraventricular) and varying contrasts. The results obtained by all the proposed techniques are presented for some sample images in Figs. 5.6 to 5.16. All the methods have given good enhancement in terms of the contrast, especially for T1-weighted images which is evident from the figures. The enhanced images were evaluated by two neutral observers trained in MR image analysis who were blinded to the data sets. The evaluators rated the images on a scale of 1 (best contrast) to 4 (poor contrast).

To eliminate the possible bias of the evaluators, the orientations of the images were also changed. The order of presentation of the (test) images was random, also with respect to their original contrast. The outcome of their evaluation is given in Table 5.3. The evaluations agreed very well in the case of most of the original and polynomial enhanced images. The evaluation of the polynomial enhanced images as having the best contrast agreed in 89 of the cases. However, independently, each of them ranked 96 or more of the polynomial enhanced images as the best. Similarly, the agreement between the radiologists on the original images as having the lowest contrast was in 98 of the test images. There is no significant difference between the outputs of WNM-1 and WNM-2 as evaluated by the observers. 103 or more of these images were ranked as 2 or 3, consistently by both the evaluators.

We extended the enhancement techniques to pathological MR images and some CT images also, to explore their clinical utility on a routine basis. These images were evaluated after enhancement by all the methods. The neuroradiologists judged the polynomial based method to be the best for enhancing the pathological MR images too. So, we present the results of enhancement of MR images by the polynomial method in Fig. 5.17 for four clinical cases. From top to bottom, the images shown correspond to hematoma, multiple infarct, multiple sclerosis and white matter disease, respectively. The results of enhancement of CT images are displayed in Figs. 5.18 to 5.20. In conclusion, we see that the polynomial based enhancement results in the best contrast both in normal

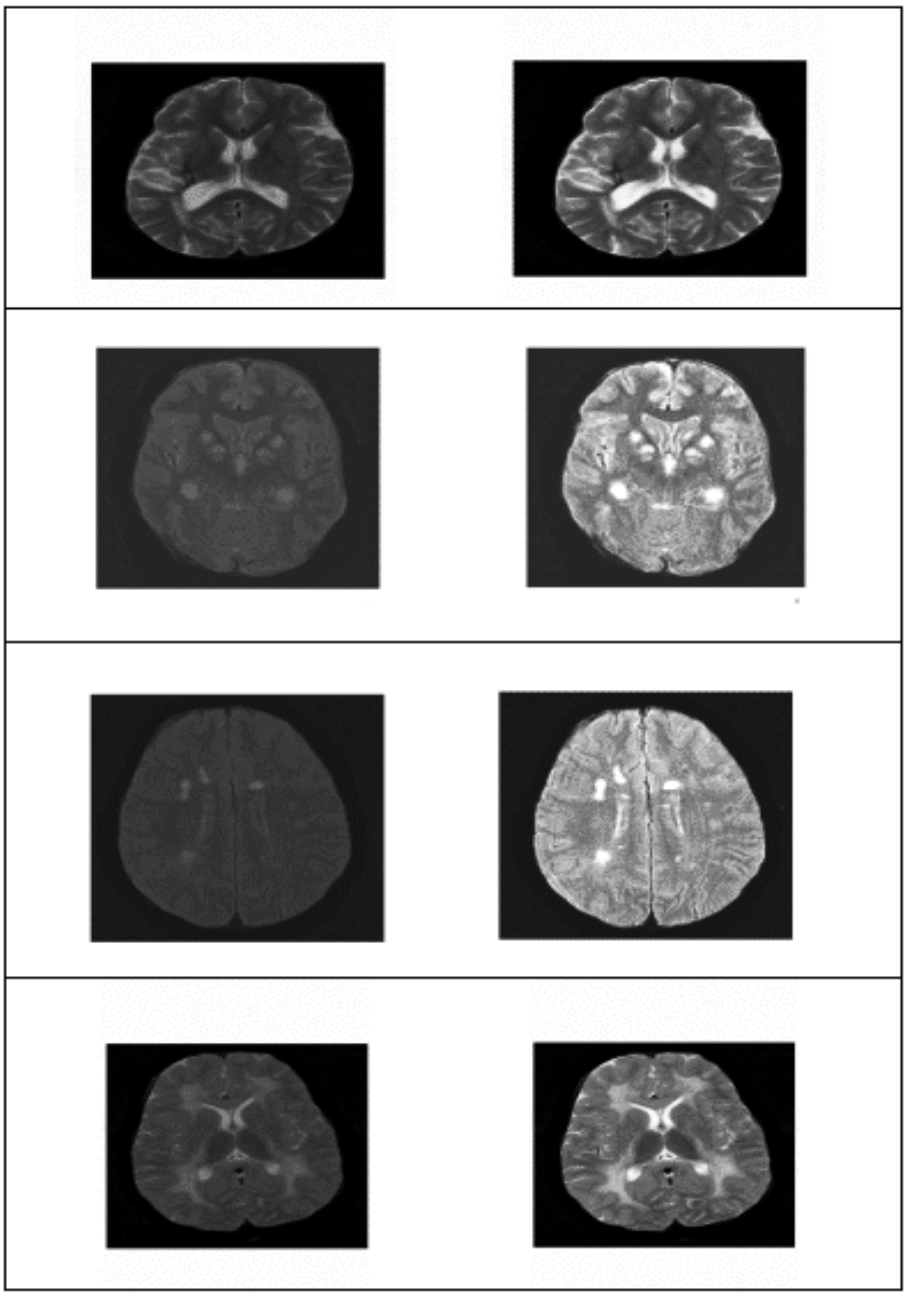

Figure 5.17: Pathological images enhanced by the polynomial method

Table 5.3: Results of evaluation of enhanced images

ORIGINAL IMAGES

		EVAL 1				
	Rating	**1**	**2**	**3**	**4**	**Total**
E	**1**	0	1	1	1	3
V	**2**	0	0	0	1	1
A	**3**	0	1	1	4	6
L	**4**	0	1	11	98	110
2	**Total**	0	3	13	104	120

IMAGES ENHANCED BY WNM-1

		EVAL 1				
	Rating	**1**	**2**	**3**	**4**	**Total**
E	**1**	6	0	2	0	8
V	**2**	6	36	16	1	59
A	**3**	3	20	26	0	49
L	**4**	1	1	2	0	4
2	**Total**	16	57	46	1	120

IMAGES ENHANCED BY WNM-2

		EVAL 1				
	Rating	**1**	**2**	**3**	**4**	**Total**
E	**1**	4	5	1	0	10
V	**2**	2	30	17	1	50
A	**3**	2	19	32	1	54
L	**4**	0	4	2	0	6
2	**Total**	8	58	52	2	120

POLYNOMIAL ENHANCED IMAGES

		EVAL 1				
	Rating	**1**	**2**	**3**	**4**	**Total**
E	**1**	89	1	3	6	99
V	**2**	3	1	2	3	9
A	**3**	3	2	2	4	11
L	**4**	1	0	0	0	1
2	**Total**	96	4	7	13	120

and abnormal MR images, and may have a wider application to other medical imaging modalities also.

5.5 Segmentation

There are many important applications of pattern recognition, which include a wide range of information processing problems of great practical significance, from speech recognition and the classification of handwritten characters, to fault detection and medical diagnosis.

There are two basic approaches in pattern recognition depending on the external knowledge about the input data. If we know the labels of input data, the pattern recognition problem is known as *supervised*, else *unsupervised*. In the case of *unsupervised*

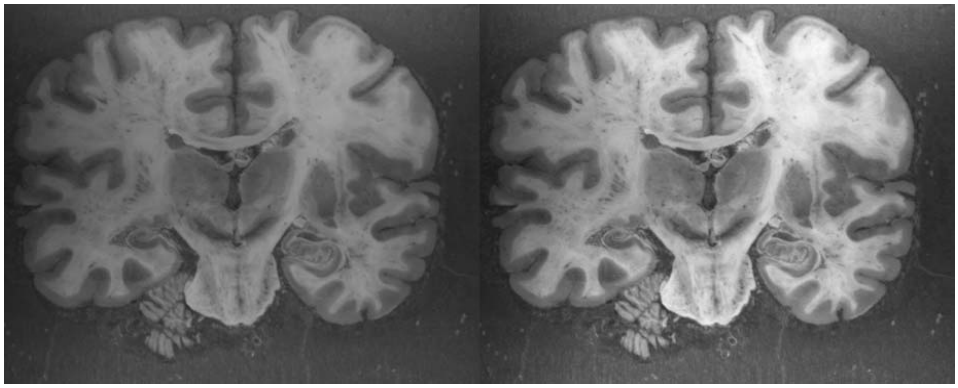

Figure 5.18: CT image enhanced by WNM-1

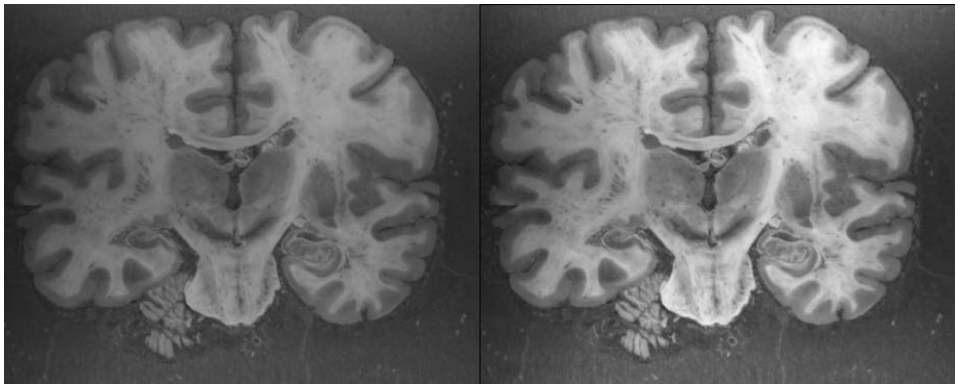

Figure 5.19: CT image enhanced by WNM-2

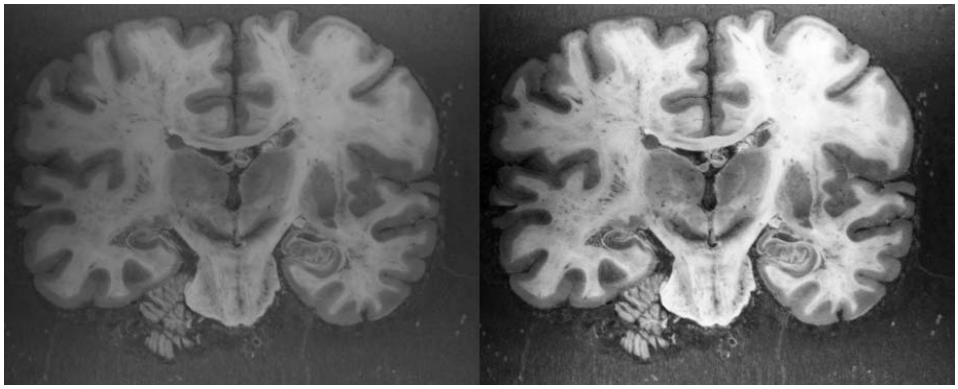

Figure 5.20: CT image enhanced by polynomial method

classification or *clustering*, the complexity of the problem increases since we don't have the labels. Each cluster is defined in terms of certain properties. The fundamental problem in clustering lies in choosing these properties.

There are two fundamental approaches to clustering, namely, *parametric* and *non-parametric*. If the purpose of unsupervised learning is data description, then we assume a predefined distribution function for the data set, and calculate the sufficient statistics which will describe the data set. For example, if we assume that a data set X comes from a normal distribution $N(\mu, \sum)$, the sufficient statistics are the sample mean $\mu = E\{X\}$ and the sample covariance $\sum = E\{XX^T\}$, which will describe the distribution perfectly. Another approach uses a mixture of distributions to describe the data [67, 68, 31]. We can approximate virtually any density function in this way, but estimating the parameters of a mixture is not trivial.

The mixture model is a semi-parametric way of estimating the underlying density function [32, 74, 18]. In the non-parametric kernel-based approach to density estimation, the density function is represented as a linear superposition of kernel functions, with one kernel centered on each data point.

In our work, we have used Gaussian mixture model (GMM), which is a measurement model for segmentation. The model relates the image data to the segmentation and takes the form of a finite gaussian mixture [86]. We have considered a *three-tissue gaussian* model (gray matter, white matter and cerebrospinal fluid), for segmentation. The brain region is extracted from the head scan prior to segmentation. The model parameters are estimated completely from the input image data. Intensities at the voxel sites were used as input feature to the segmentation algorithm.

5.5.1 Statistical Model

Consider a 3-D image volume that consists of a set of contiguous anisotropic rectangular parallelopipeds referred to as *voxels*. The voxels are defined on a 3-D cubic grid of points and indexed by Cartesian coordinates [85]. The set of coordinates of the voxels in the image is denoted by $I \subset N^3$ and the image is denoted by $y = (y_i, i \in I)$ where y_i denotes

the image intensity at the voxel indexed by i.

Assume that the spatial volume of each voxel is occupied by only one class of tissue. Let the total number of tissue classes in the image be K and each of them be represented by a label from $\Lambda = \{1, 2, \ldots, K\}$. If x_i denotes an instance of a random variable representing the tissue class at the voxel site i, $x_i = k$ indicates that the tissue class k is assigned to the voxel i. A segmentation is then denoted by $x = (x_i, i \in I)$. The process of segmentation is to find x which represents the correct tissue class at each voxel of image y. Our attempt was to find $x = x^*$, which represents optimal segmentation i.e

$$x^* = arg \ \ max_{x \in \Omega} \ \ p(x|y) \tag{5.20}$$

where Ω is the set of all possible segmentations and $p(x|y)$ is the posterior density of the segmentation x given the image y. Since the prior probability of the image $p(y)$ is independent of the segmentation x, from Baye's theorem

$$p(x|y) \propto p(x, y) \ \ = \ \ p(y|x)p(x) \tag{5.21}$$

where $p(y|x)$ is the conditional probability density of the image y given the segmentation x and $p(x)$ is the prior density of x. Our attempt is to find the *maximum a posteriori* (MAP) estimate by modeling $p(y|x)$, the measurement model.

Each tissue class has a signature, or mean intensity and variance at a particular site. For each tissue class, a gaussian distribution is assumed and the entire image can be assumed as a gaussian mixture density. A Gaussian mixture density is a weighted sum of K component densities as depicted in Fig. 5.21 and given by the equation

$$p(\mathbf{y}|\Theta) \ \ = \ \ \sum_{i=1}^{K} \ \ w_i \ \ g_i(\mathbf{y}) \tag{5.22}$$

where $\mathbf{y}$ is a d-dimensional random vector, $g_i(\mathbf{y}), i = 1 \ldots K$, are the component densities and $w_i, i = 1 \ldots K$, are the mixture weights. Each component density is a d-variate Gaussian function of the form

$$g_i(\mathbf{y}) \ \ = \ \ \frac{1}{2\pi^{\frac{d}{2}} |\Sigma_i|^{\frac{1}{2}}} \ \ exp \ \ \{-\frac{1}{2}(\mathbf{y} - \mu_\mathbf{i})^T {\Sigma_i}^{-1} (\mathbf{y} - \mu_\mathbf{i})\} \tag{5.23}$$

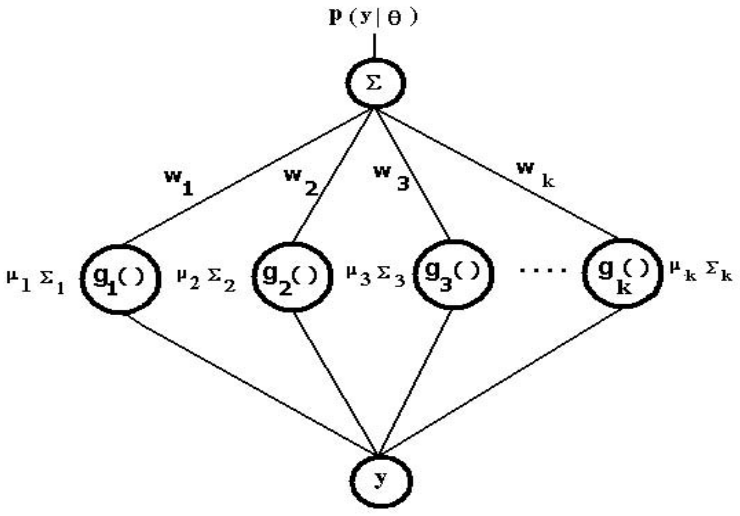

Figure 5.21: Depiction of a K-component gaussian mixture density. (w_i, i=1..,K are the mixture weights and $g_i()$, i=1...K are the component gaussians).

where $\mu_\mathbf{i}$ is the mean vector and Σ_i is the covariance matrix. The mixture weights satisfy

$$\sum_{i=1}^{K} w_i = 1 \tag{5.24}$$

The complete Gaussian mixture density is parameterized by the mean vectors, covariance matrices and mixture weights from all component densities. These parameters are collectively represented by the notation

$$\Theta = \{w_i, \mu_\mathbf{i}, \Sigma_i\} \quad \text{for } i = 1 \ldots K \tag{5.25}$$

In our case, since the input is intensity at a given point i, the dimension is one ($d = 1$), and the number of classes $K = 3$ corresponding to gray matter, white matter and cerebrospinal fluid.

There are two principal motivations for using Gaussian mixture densities to represent MR brain image data. The first is the empirical observation that a linear combination of Gaussian basis functions is capable of representing a large class of sample distributions. One of the powerful attributes of the GMM is its ability to

form smooth approximations to arbitrarily-shaped densities. The second motivation is due to the observation from many MR brain images, that the distribution of different brain tissues approximates a normal distribution.

5.5.2 Maximum Likelihood Parameter Estimation

Given samples from the image, the goal of a segmentation algorithm is to estimate the parameters of the GMM, Θ, which in some sense best matches the distribution of the input samples. There are several techniques available for estimating the parameters of the GMM [67]. The popular and well-established method is maximum likelihood (ML) estimation.

The aim of estimation is to find the parameters that maximize the likelihood of the GMM, given the training data. For a sequence of T training vectors $Y = \{y_1, y_2, \ldots, y_T\}$, the GMM likelihood can be written as

$$p(Y|\Theta) = \prod_{i=1}^{T} p(y_i|\Theta) \tag{5.26}$$

If $p(Y|\Theta)$ is a well behaved, differentiable function of Θ, then $\hat{\Theta}$ can be found by the standard methods of differential calculus. Unfortunately, this expression is a nonlinear function of the parameters Θ and direct maximization is not possible. However, ML parameter estimates can be obtained iteratively using a special case of the expectation-maximization (EM) algorithm [31].

For analytical purposes, it is usually easier to work with the logarithm of the likelihood than with the likelihood itself. Since the logarithm is a monotonically increasing function, the $\hat{\Theta}$ that maximizes the log-likelihood also maximizes the likelihood.

The EM algorithm begins with an initial model Θ, and estimates a new model $\hat{\Theta}$, such that $p(Y|\hat{\Theta}) \geq p(Y|\Theta)$. The new model then becomes the initial model for the next iteration and the process is repeated until some convergence threshold is reached. The EM algorithm is given as follows.

Algorithm:

- Begin

  Initialize:

  $\Theta^0,\ Threshold,\ i\ =\ 0$

  do $i\ \leftarrow\ i+1$

  E step : $compute\ \ Q(\Theta;\Theta^i)$

  M step : $\Theta^{i+1}\ \leftarrow\ arg\ max_\Theta\ \ Q(\Theta;\Theta^i)$

  until $Q(\Theta^{i+1};\Theta^i) - Q(\Theta^i;\Theta^{i-1})\ \leq\ Threshold$

  return $\hat{\Theta}\ \leftarrow \Theta^{i+1}$

- end.

In each EM iteration, the following reestimation formulas are used, which guarantee a monotonic increase in the model's likelihood value:

$$\text{Mixture Weights}: \quad \bar{w_i} = \frac{1}{T}\ \sum_{t=1}^{T}\ p(i|y_t,\Theta) \tag{5.27}$$

$$\text{Means}: \ \bar{\mu_i} = \frac{\sum_{t=1}^{T}\ p(i|y_t,\Theta)\ \ y_t}{\sum_{t=1}^{T}\ p(i|y_t,\Theta)} \tag{5.28}$$

$$\text{Variances}: \quad \bar{\sigma_i}^2 = \frac{\sum_{t=1}^{T}\ p(i|y_t,\Theta)\ \ {y_t}^2}{\sum_{t=1}^{T}\ p(i|y_t,\Theta)} - \bar{\mu_i}^2 \tag{5.29}$$

The *a posteriori* probability for each class i is given by

$$p(i|y_t,\Theta) = \frac{w_i g_i(y_t)}{\sum_{k=1}^{K} w_k g_k(y_t)} \tag{5.30}$$

In our work, as mentioned earlier a *three-tissue gaussian* model was assumed to characterize the gray matter, white matter and cerebrospinal fluid. The EM algorithm was used to estimate the parameters of the gaussian mixture. The threshold points for segmentation into different classes were selected as the intersection points of adjacent gaussian distributions. The segmentation algorithm used is described below.

Algorithm :

- Begin Read image : $orgimg(i,j) = img$

  Convert to data vector: $datvec \leftarrow orgimg(i,j)$

  Compute the histogram : $orghist \leftarrow Histogram(datvec)$

  Find the background pixels from the histogram (peak corresponding to maximum number of elements).

  Assign : $B_{th} \leftarrow$ max value of the background pixels.

  Form a new data vector($\mathbf{y}$) : $newdatvec \leftarrow orgimg($ find $(orgimg > B_{th}))$

  Segmentation Thresholds : $segcent = B_{th}$

  To find the remaining threshold points do:

  Assume a GMM : $p(\mathbf{y}|\Theta) = \sum_{i=1}^{K} w_i \; g_i(\mathbf{y})$

  Number of Clusters : $K = 3$

  Dimension of feature vector : $d = 1$

  Find : $[T,d] =$ size$(newdatvec)$

  The training samples are : $newdatvec$

  Initialize :

  $Means = Random(d,K)$

  $Weights = Random(d,K)$

  $Variances = Random(d,K)$

  Call EM routine : Begin

  Initialize:

  $\Theta^0, \; Threshold, \; i = 0$

do $i \leftarrow i+1$

E step : $compute \;\; Q(\Theta;\Theta^i)$

M step : $\Theta^{i+1} \leftarrow arg\, max_\Theta \;\; Q(\Theta;\Theta^i)$

until $Q(\Theta^{i+1};\Theta^i) - Q(\Theta^i;\Theta^{i-1}) \;\; \leq \;\; Threshold$

return $\hat{\Theta} \leftarrow \Theta^{i+1}$

end.

In each EM iteration reestimation is done using equations 5.27 to 5.29. After convergence, we get the parameters of each gaussian density function, namely, mean, variance and weight.

Compute remaining segmentation Thresholds :

for $\;\; i \;=\; 1 : (K-1)$

find the intensity point (m) where $g_i(Y|\Theta) = g_{i+1}(Y|\Theta)$

$segcent = append \;\; [segcent \;\;\; m]$

end.

Sort : $segcent \;\; \leftarrow$ sort $(segcent)$

Segmentation:

Obtain:

$encimg \;\; =$ find $(orgimg < segcent(1))$

$encimg1 \;\; =$ find $(segcent(1) \leq orgimg < segcent(2))$

$encimg2 \;\; =$ find $(segcent(2) \leq orgimg < segcent(3))$

$encimg3 \;\; =$ find $(orgimg \geq segcent(3))$

- end.

The results of segmentation are shown in Figs. 5.27 to 5.46. In the current algorithm,

the weights, means and variances of GMM are assigned random initial values. Initially, the original images were used as input images. Since the results were not satisfactory, a set of modifications were done. The modifications are

1. Instead of original images, enhanced images were used for segmentation.
2. Instead of using random values, the initial values for the parameters of GMM were estimated using Vector quantization, k-means, or Fuzzy c- means algorithms.
3. Fuzzy c- means based segmentation was tried with original and enhanced images.

Improved segmentation resulted when enhanced images were used. The convergence of EM algorithm was faster when initial estimates of the parameters were done by VQ, k-means or Fuzzy c- means.

5.5.3 Fuzzy c - Means

In the hard clustering process, each data sample is assigned to only one cluster and all clusters are regarded as disjoint gatherings of the data set. In practice, however, there are many cases in which the clusters are not completely disjoint and data could be classified as belonging to one cluster almost as well to another. Such a situation cannot be handled by a crisp classification process; the separation of the clusters becomes a fuzzy notion. The representations of real data structures can then be more accurately handled by fuzzy clustering methods.

The fuzzy c-means (FCM) algorithm is the best known and the most widely used fuzzy clustering technique. This algorithm iteratively minimizes the following criterion function:

$$J(U,V) = \sum_{i=1}^{c} \sum_{k=1}^{n} u_{ik}^{m} \ |x_k - v_i|^2 \tag{5.31}$$

where

- $x_1, \ldots, x_n$ are n input sample vectors;
- $V = \{v_1, \ldots, v_c\}$ are cluster centers;
- $U = [u_{ik}]$ is a $c \times n$ matrix, where u_{ik} is the i^{th} membership value of x_k. The membership values satisfy the following conditions

  $0 \leq u_{ik} \leq 1 \quad i = 1, 2, \ldots, c \; ; \quad k = 1, 2, \ldots, n$

  $\sum_{i=1}^{c} u_{ik} = 1 \quad k = 1, 2, \ldots, n;$

  $0 < \sum_{k=1}^{n} u_{ik} < n \quad i = 1, 2, \ldots, c$
- $m \in [1, \infty)$ is an exponent weighting factor.

The objective function is the sum of the squared Euclidean distances between each input sample and its corresponding cluster center, with the distances weighted by the memberships. The algorithm is iterative and makes use of the following equations:

$$v_i = \frac{1}{\sum_{k=1}^{n} u_{ik}^m} \sum_{k=1}^{n} u_{ik}^m \; x_{ik} \quad i = 1, 2, \ldots, c \tag{5.32}$$

$$u_{ik} = \frac{\left[\frac{1}{|x_k - v_i|^2}\right]^{\frac{1}{m-1}}}{\sum_{j=1}^{c} \left[\frac{1}{|x_k - v_j|^2}\right]^{\frac{1}{m-1}}} \quad i = 1, 2, \ldots, c \; ; \quad k = 1, 2, \ldots, n \tag{5.33}$$

To compute a cluster center, all the input samples are considered and the contributions of the samples are weighted by this membership values. For each sample, its membership value in a particular class depends on its distance to the corresponding cluster center. The weight factor m reduces the influence of small membership values. The larger the value of m, the smaller the influence of samples with small membership values.

The FCM clustering procedure consists of the following steps:

1. Initialize $U^{(o)}$ randomly or based on an approximation; initialize $V^{(o)}$ and calculate $U^{(o)}$. Set the iteration counter $\alpha = 1$. Select the number of class centers c and choose the exponent weight m.
2. Compute the cluster centers. Given $U^{(\alpha-1)}$, calculate $V^{(\alpha)}$ according to equation 5.32.

3. Update the membership values. Given $V^{(\alpha)}$, calculate $U^{(\alpha)}$ according to equation 5.33.

4. Stop the iteration if

$$\max |u_{ik}^{(\alpha)} - u_{ik}^{(\alpha-1)}| \leq \epsilon \tag{5.34}$$

else let $\alpha = \alpha + 1$ and go to Step 2, where ϵ is a pre-specified small number representing the smallest acceptable change in U.

Enhanced images, with the background eliminated, are used as input to the FCM algorithm. Three class segmentation was carried out on the input. The FCM-based segmentation algorithm is described below.

Algorithm

- Begin

  Read the input image: $orgimg(i,j) \leftarrow img$

  Enhance the image using the weighted nonlinear methods or polynomial method, described in section 5.3.

  $enhimg \leftarrow$ Enhance$(orgimg)$

  Separate background from the enhanced image

  $intimg \leftarrow$ find $(enhimg > B_{th})$

  Form a data vector from the intermediate image

  $datvec \leftarrow intimg$

  Call FCM algorithm :

  $cent = 3$

  $finalcent =$ FCM$(datvec, cent)$

  find distance between input samples and $finalcent$

  $[val \quad ind] = dist(finalcent, datvec)$

  Assign the samples to the minimum distance $finalcent$

  $datvec(i) \leftarrow mindist(finalcent, datvec(i))$

Encode the image

$Encimg = \sum_{i=1}^{noclusters} encimg(i)$

where

$encimg(1)$ =find$(enhimg < finalcent(1))$

$encimg(2)$ =find$(finalcent(1) \leq enhimg < finalcent(2))$

$encimg(3)$ =find$(finalcent(2) \leq enhimg < finalcent(3))$

$encimg(4)$ =find$(enhimg \geq finalcent(3))$

- end.

The results obtained using FCM based clustering for different images are given in Figs. 5.27 to 5.46.

5.6 Results and Discussion

In some of the routine scan MR images, it was difficult to identify the different regions due to low contrast. Hence, we first considered enhancing the images. The WNM-1 is a point based method, where each pixel value is modified or weighted by the logarithm of its intensity. In the WNM-2, the value of a pixel is modified by the logarithm of sum of the squares of the pixel intensity, carried over a 3×3 neighbourhood. The WNM-2 not only acts as an enhancement method, but also as a low pass filter due to averaging of the pixels over the neighbourhood. The polynomial method described in section 5.3.3 maps the intensity values nonlinearly.

All the methods have given good enhancement in terms of the contrast, especially for T1-weighted images which is evident from the figures. This is because, in most T1-weighted images, the gray values are distributed in the low range of the gray scale, giving room for enhancement. However, in the case of T2-weighted images, the histogram extends up to the maximum gray level. Thus, the logarithm based methods, which basically stretch the low gray level region of the histogram, are less effective with T2-weighted images. The polynomial method has worked very well with both T1- and T2-weighted images. This is due to two reasons: (i) The enhancement is symmetric around x_c, which

feature is missing in the other two methods. (ii) The choice of x_c gives an extra degree of freedom to select the region on the gray scale where enhancement is necessary. Excellent differential tissue contrast can be obtained by appropriately choosing x_c. Further, the advantage with the polynomial method is that the slope of enhancement can be chosen depending on the need. A gaussian model was assumed for estimating x_c, as a linear combination of appropriate gaussian basis functions is capable of representing a large class of sample distributions and the observation from many MR brain images show that the distribution of different brain tissues approximates a normal distribution.

The scans interpreted as normal by the neuroradiologists were used for segmentation. The skull boundary was removed manually. The remaining matter of the brain was classified as gray matter, white matter and CSF. Although blood vessels may be classified either as gray matter or white matter, the percentage error resulting from the presence of vasculature is negligibly small. Therefore, the three tissue model can be used to represent the intensity distributions of the cerebral images.

Segmentation of MR brain images was carried out on original and enhanced images using the GMM, modified GMMs and fuzzy c-means techniques. The segmentation of the original images had unsatisfactory results due to low contrast between different tissue classes. Especially, segmentation of T2-weighted images was difficult as the histogram (after the removal of the background) was unimodal with a large variance for most of the images. For such images, selection of thresholds to segment into different regions was a difficult task.

Among the enhancement techniques, polynomial based method has given rise to the best segmentation results for both T1- and T2-weighted images. The segmentation obtained with all the five methods are comparable in the case of polynomial enhanced image as input.

Fig. 5.22 shows the histogram of a sample image and the histogram estimated by the GMM using random initialization. It is evident that the approximation by the GMM is not accurate because the separation between the second and third peaks is small. There is considerable overlap between the two corresponding gaussians resulting in more than

half the area of one being enclosed by the other gaussian. This inefficient characterization of the histogram by the GMM leads to poor segmentation, as shown in Fig. 5.29. Since the obtained segmentation with the original images is far from satisfactory, segmentation was attempted on the enhanced images.

Figures 5.23 to 5.26 present the original, enhanced and estimated histograms and the details of the gaussian mixture model along with threshold points used for segmentation. It may be noted that in the above figures, the y-axis scale is chosen to clip the background peak in the histogram, and to highlight the smaller peaks. The enhancement spreads the means of the three peaks, thus facilitating precise fitting of the individual peaks by the gaussians. It was observed that all the estimation methods (GMMs with various initializations) approximated the histograms of the enhanced MR images consistently. This is evident from the sample results shown in Figs. 5.23 to 5.26.

The segmentation results for all the methods, obtained for 5 different slices of both T1- and T2-weighted images for one subject are given in Figs. 5.27 to 5.46. In all the figures, the arrangement of the results are as follows. First row: original image, results of segmentation by GMM with random and k-means initializations. Second row: results of segmentation by GMM with VQ and FCM initializations, and FCM based segmentation. Figs. 5.27 to 5.31 show the results of segmenting the original images, without any enhancement. We see that the segmentation is very poor in all the T2-weighted images, whereas it is acceptable in the case of most T1-weighted images. This is because each of the different variants of GMM has introduced one gaussian in the low intensity region of the histogram, which has incidentally been able to capture the CSF peak lying in the same region in the case of T1-weighted images.

Figs. 5.32 to 5.41 illustrate the results obtained with images enhanced by WNM-1 and WNM-2. As shown by Figs. 5.34 to 5.36, in the case of most T2-weighted images, though FCM based segmentation has succeeded in correctly segmenting the three types of tissues, the other four methods have resulted in only two classes. On the other hand, in the case of T1-weighted images (see 5.32 to 5.34 top panel), the GMM based methods have achieved correct segmentation in every case, whereas the FCM has failed to capture some

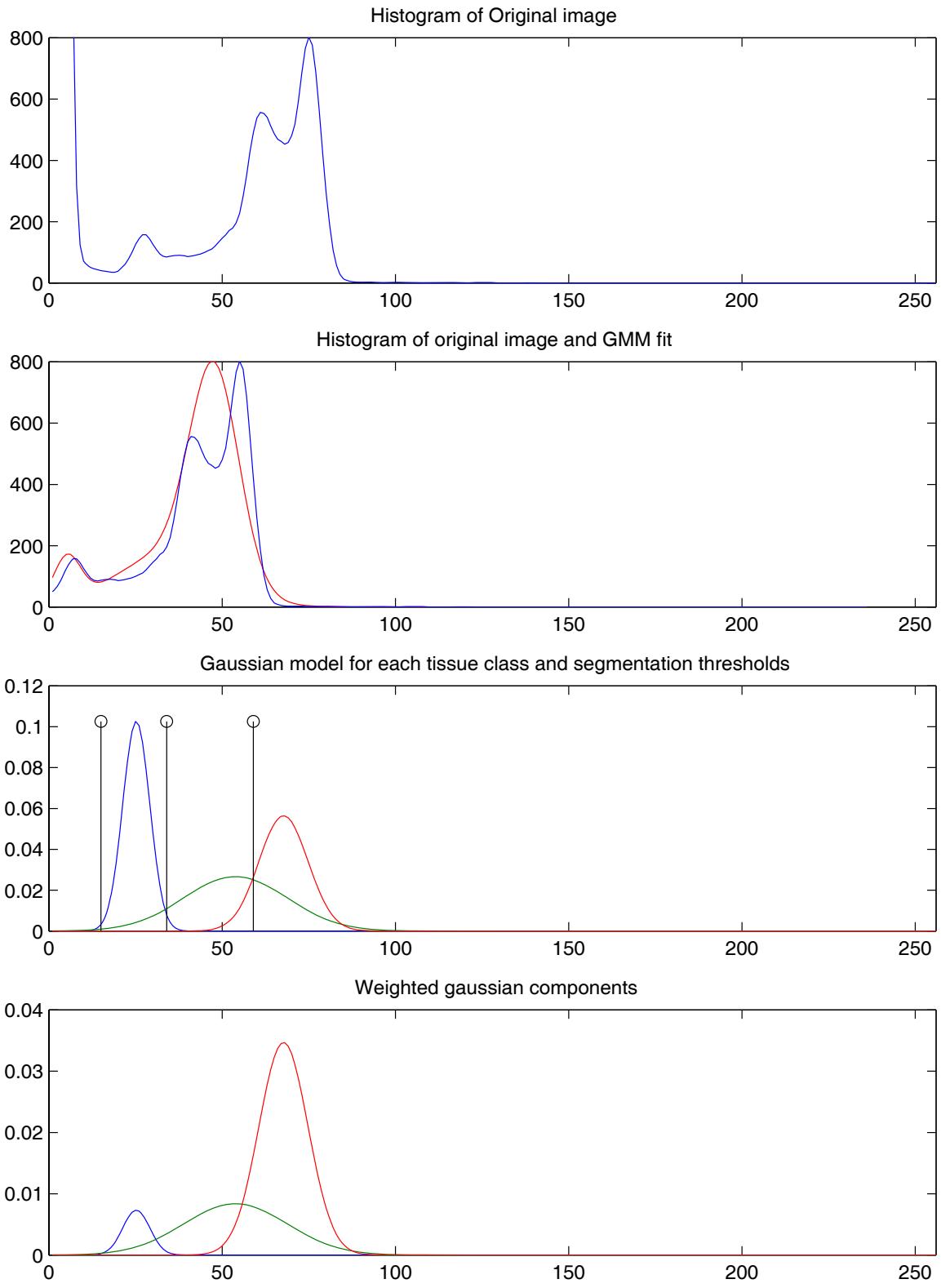

Figure 5.22: GMM, with random initialization, of an original image

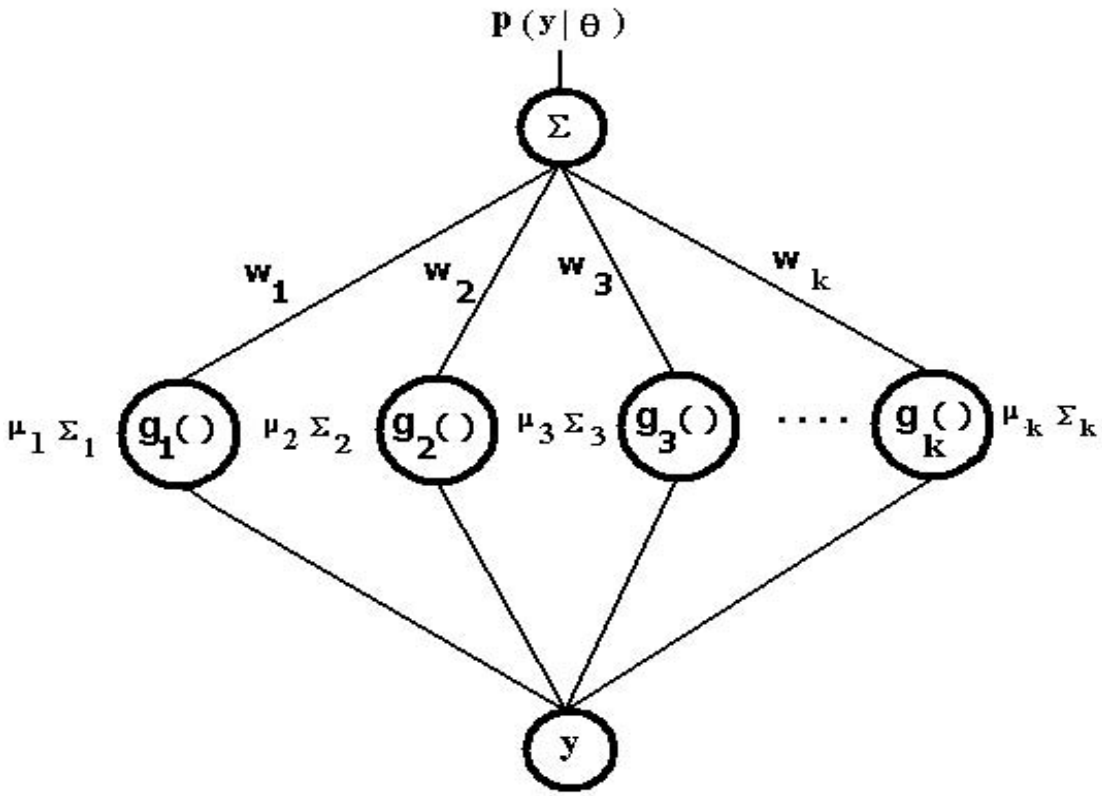

Figure 5.23: GMM with random initialization for polynomial enhanced image

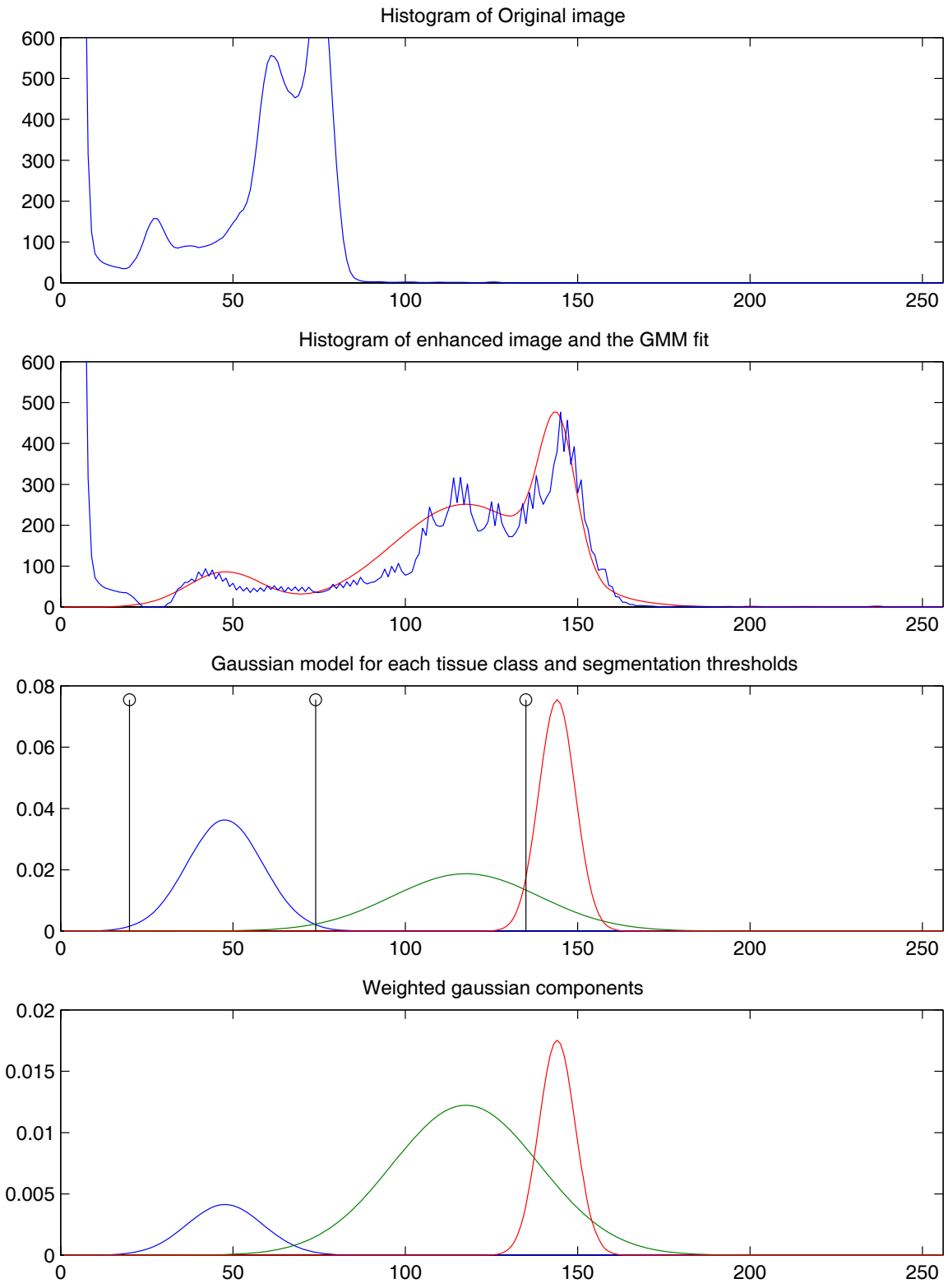

Figure 5.24: GMM with k-means initialization for polynomial enhanced image

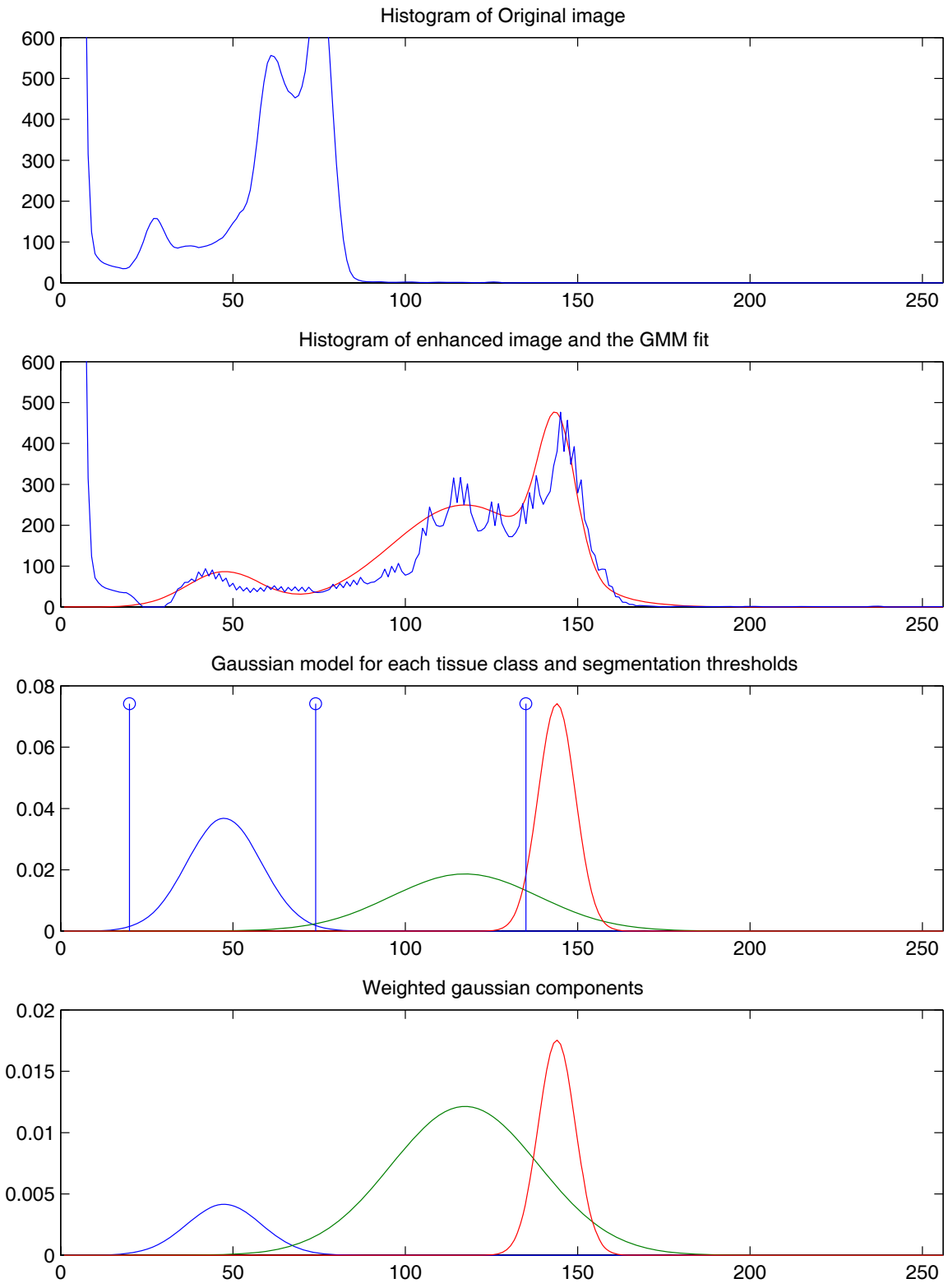

Figure 5.25: GMM with VQ initialization for polynomial enhanced image

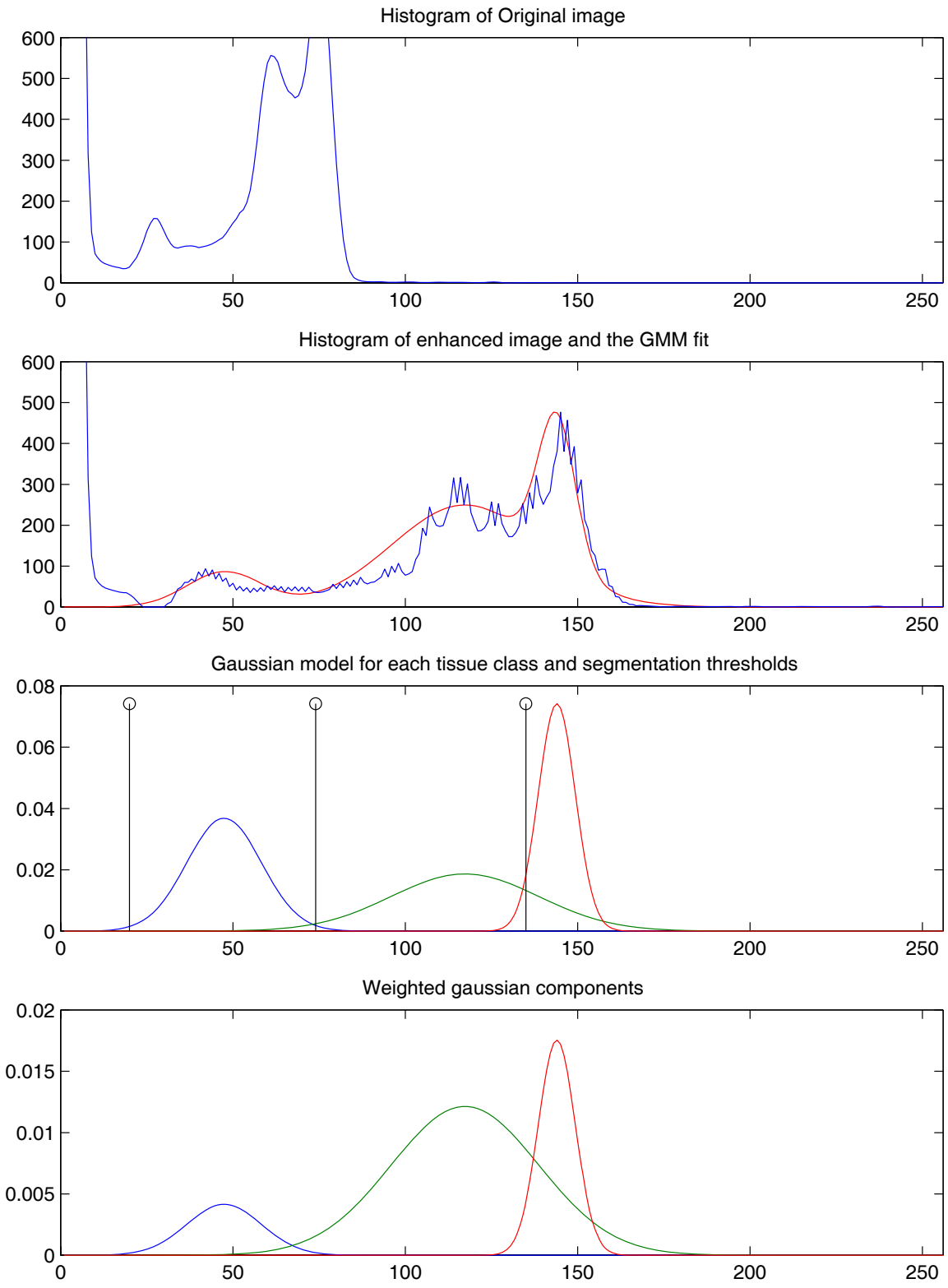

Figure 5.26: GMM with FCM initialization for polynomial enhanced image

of the minor gray regions interspersed with majority white regions. Similar observations can be made regarding the performance of GMM and FCM based methods, in the case of enhancement by WNM-2 too (see Figs. 5.37 to 5.41).

Figs. 5.42 to 5.46 present the segmentation resulting from images enhanced by the polynomial method. It can be clearly seen that with polynomial enhanced images, every segmentation method performs reasonably well. However, it can be observed that the FCM algorithm once again fails to capture some of the gray regions interspersed within white regions. It also fails badly in some of the T2-weighted images as illustrated by 5.46. The bottom panel in the same figure also shows that VQ and FCM based initializations too sometimes fail in the case of T2-weighted images, especially when the number of pixels of any one class of tissue is insignificantly small and the region of the histogram characterizing that class lies within few standard deviations of the nearest major peak (class).

Figs. 5.47 and 5.48 show separately each of the tissue classes, segmented by the various procedures. In both the figures, the results of GMM and its variants, and FCM are shown in separate rows. In one of the T2-weighted images, the noise is identified as one of the classes, whereas the gray and CSF regions have been merged into one. Table 5.4 gives the percentage volume of each tissue as obtained by various segmentation algorithms for the original T1- and T2-weighted images shown in Figs. 5.28 and 5.30 (both bottom panel) and their corresponding enhanced images.

5.7 Conclusions

In this chapter, we have proposed nonlinear enhancement techniques for MR images. WNM-1 is a point based operation, whereas WNM-2 is a neighbourhood operation. In the polynomial method, we have used a third degree polynomial. Most of the images obtained from the neurocenter were of low contrast in which the details of tissues were not clearly visible. The original images were enhanced by the proposed methods. The results of enhancement and validation indicate the polynomial based method as the best. The polynomial method selects x_c adapting to the input images, eliminating the need for

user interaction. Further, it has an extra degree of freedom in the choice of m, the slope of the enhancement curve at x_c. It has worked well for both T1- and T2- weighted images. Hence it is most suitable for enhancement of MR images (both normal and pathological) among the proposed methods. Initial experiments on some x-ray CT images have shown that it may be applicable to other medical imaging modalities too. WNM-1 and WNM-2 have worked well with both T1- and T2- weighted images. However, the differential contrast enhancement among the different tissues especially with T2-weighted images is not as much as given by the polynomial method.

Segmentation of MR images was formulated on the basis of a statistical model, in which a GMM was used. The GMM based segmentation was initially carried out on the original images. Though segmentation of T1-weighted images had acceptable results, the results of T2-weighted images were not satisfactory. We then attempted segmenting the enhanced images to explore the influence of enhancement on segmentation. All the enhancement methods have led to good segmentation results in the case of T1- weighted images. However, in the case of some T2-weighted images, the estimate of the histogram by GMM was poor leading to mix up in tissue classes in segmentation.

Among the enhanced images, the polynomial enhanced images have resulted in good segmentation results for both T1- and T2- weighted images. The convergence of GMM was quite slow. Hence, we modified the GMM by making changes in the initialization process. k-Means, VQ and FCM based initial estimates were employed for the GMM parameters. This resulted in faster convergence of the EM algorithm; however there were no significant changes in the final estimates.

The segmentation results of GMM and its variants were compared with those obtained by FCM. GMM and its variants have performed well with polynomial enhanced images, whereas FCM has fared better in some cases with WNMs. The results of enhancement and segmentation were appreciated by neuroradiologists.

Table 5.4: Percentage volume of each tissue determined by various segmentation algorithms for original and enhanced T1- and T2- weighted images

	CSF	GM	WM
Original Image			
GMM	16.6	53.7	29.7
GMM-kM	16.6	53.7	29.7
GMM-VQ	23.5	40.5	36.0
GMM-FCM	23.5	40.5	36.0
FCM	23.5	40.5	36.0
WNM-1 Image			
GMM	15.0	55.3	29.7
GMM-kM	15.0	55.3	29.7
GMM-VQ	14.4	41.9	43.1
GMM-FCM	23.4	38.2	38.4
FCM	23.4	38.2	38.4
WNM-2 Image			
GMM	16.9	51.0	32.1
GMM-kM	16.9	51.0	32.1
GMM-VQ	14.5	42.0	42.8
GMM-FCM	17.3	50.6	32.1
FCM	17.3	50.6	32.1
Polynomial Image			
GMM	14.0	55.9	30.0
GMM-kM	14.0	55.9	30.0
GMM-VQ	19.0	39.9	41.1
GMM-FCM	19.0	39.9	41.1
FCM	13.9	40.8	41.1

	WM	GM	CSF
Original Image			
GMM	4.1	69.2	26.7
GMM-kM	4.1	69.2	26.7
GMM-VQ	4.1	69.2	26.7
GMM-FCM	4.1	69.2	26.7
FCM	4.1	69.2	26.7
WNM-1 Image			
GMM	3.3	88.2	8.5
GMM-kM	3.3	88.2	8.5
GMM-VQ	3.2	69.9	26.9
GMM-FCM	3.3	69.8	26.9
FCM	3.3	69.8	26.9
WNM-2 Image			
GMM	3.1	70.7	26.2
GMM-kM	3.1	70.7	26.2
GMM-VQ	3.2	69.9	26.9
GMM-FCM	3.1	69.1	27.7
FCM	3.1	69.1	27.7
Polynomial Image			
GMM	25.9	56.6	17.5
GMM-kM	26.2	57.4	16.4
GMM-VQ	28.5	56.6	14.9
GMM-FCM	28.5	56.6	14.9
FCM	33.7	50.4	14.9

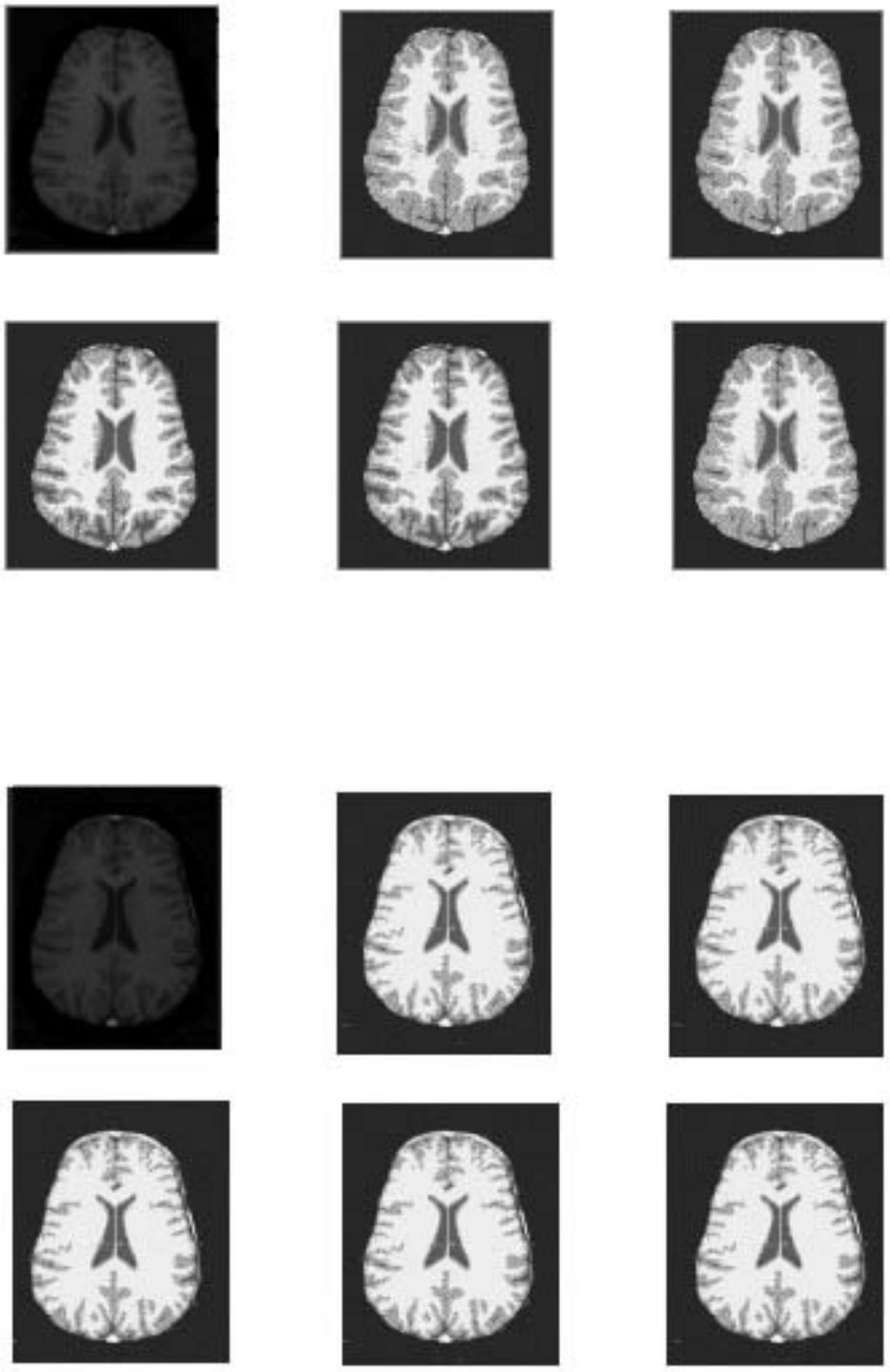

Figure 5.27: Segmentation Results - original images

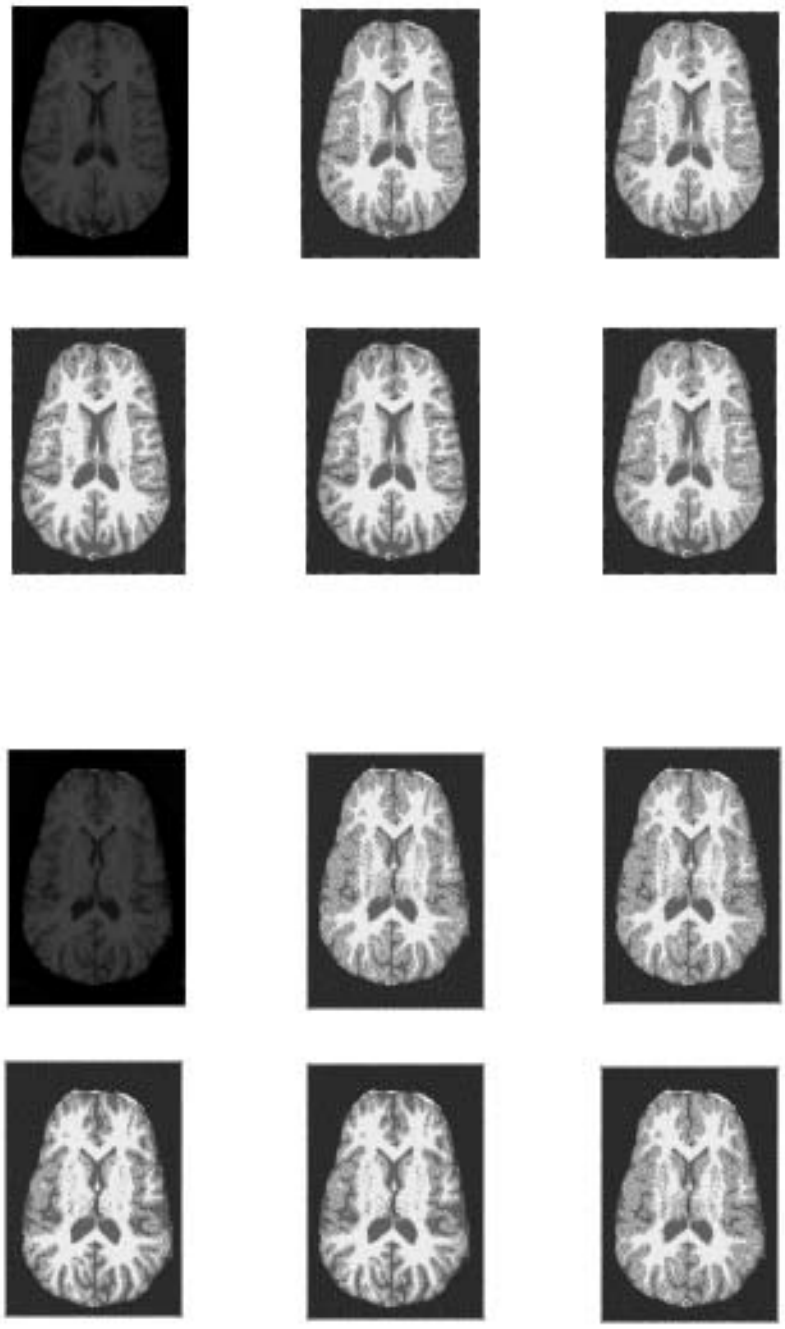

Figure 5.28: Segmentation Results - original images

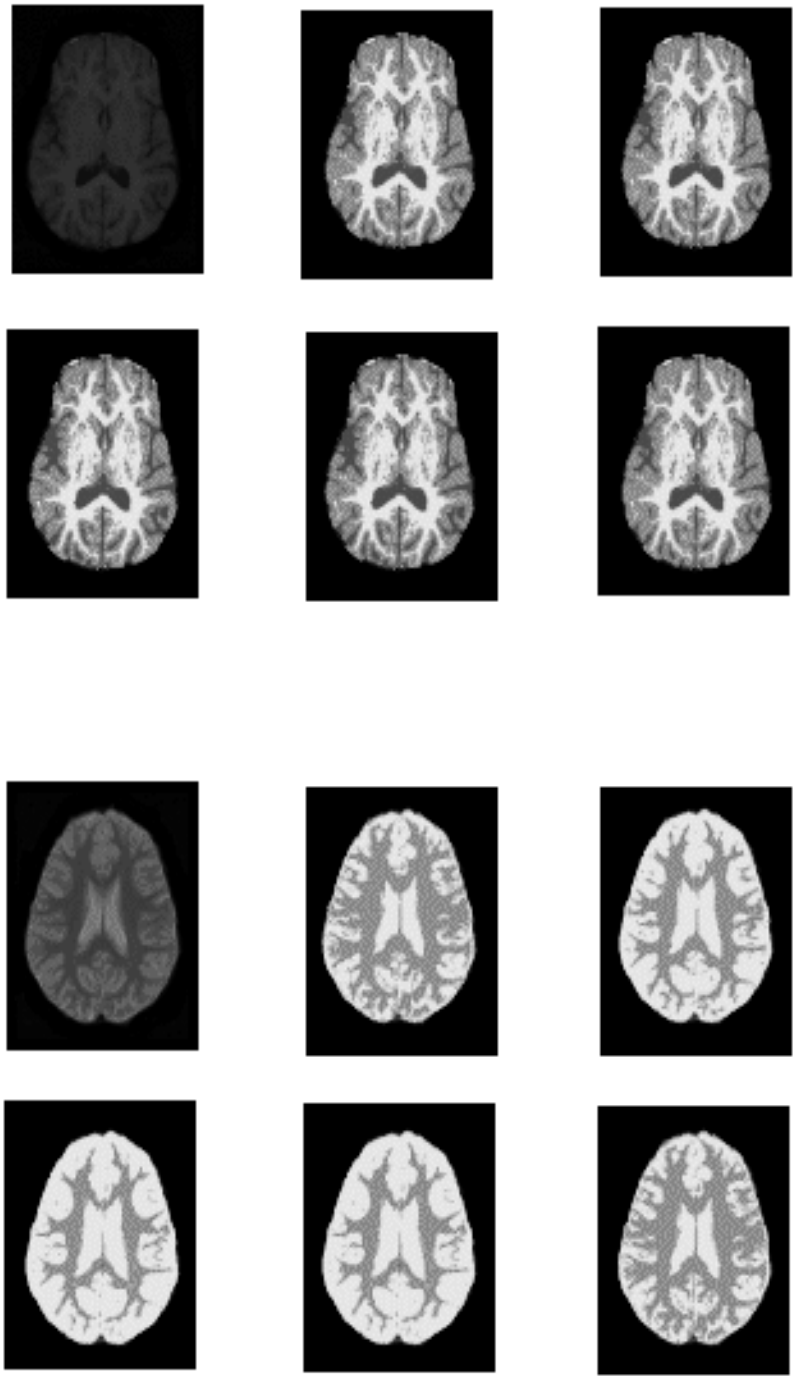

Figure 5.29: Segmentation Results - original images

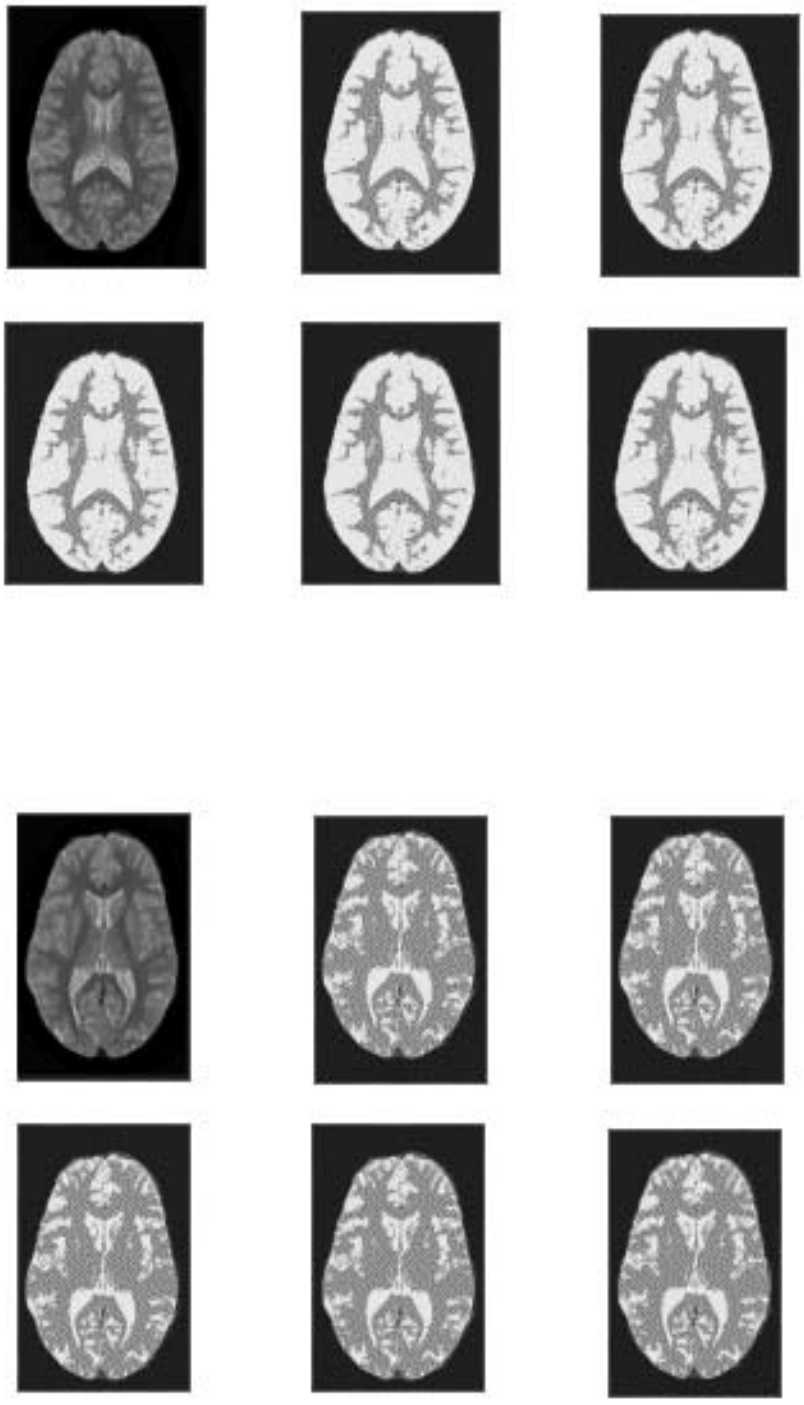

Figure 5.30: Segmentation Results - original images

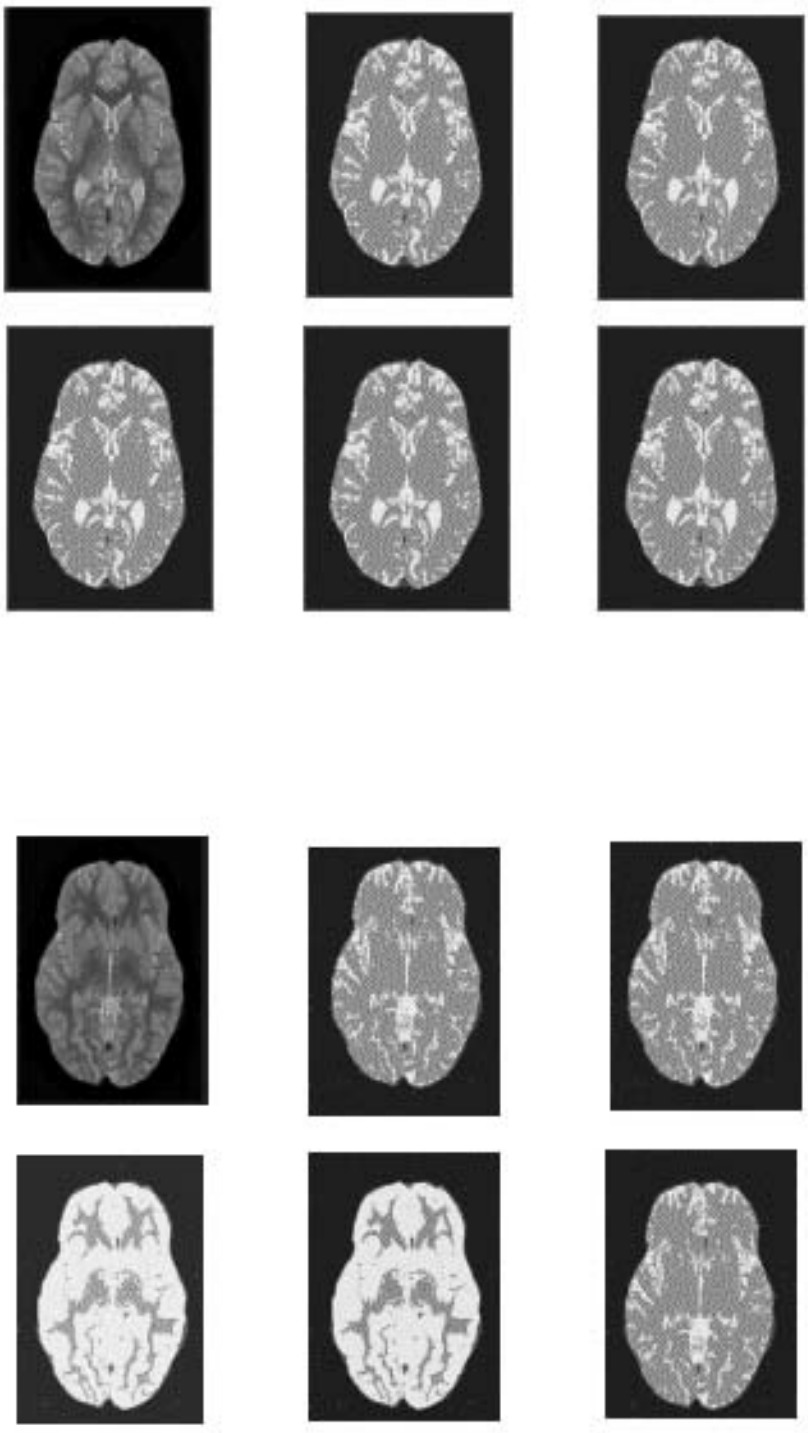

Figure 5.31: Segmentation Results - original images

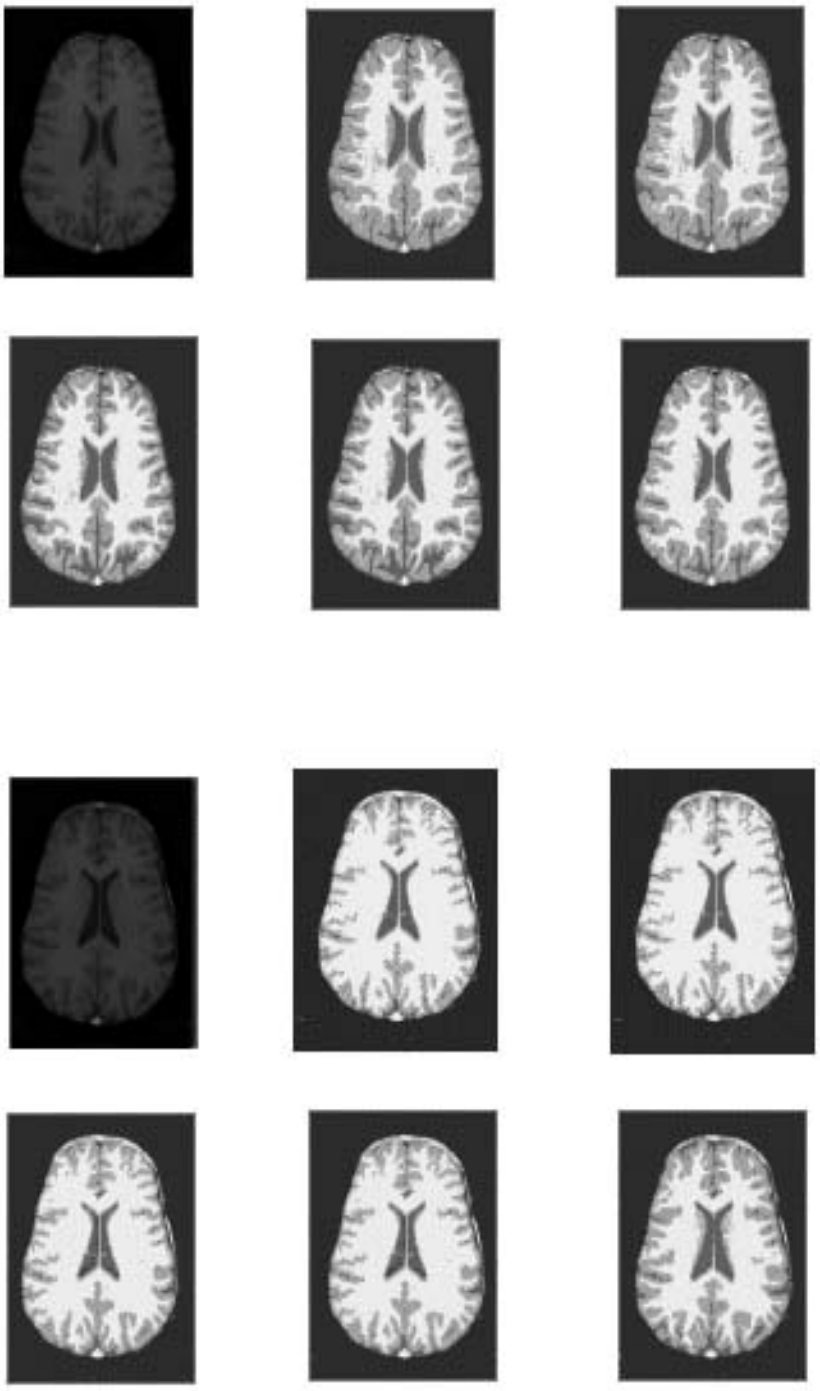

Figure 5.32: Segmentation Results - images enhanced by WNM-1

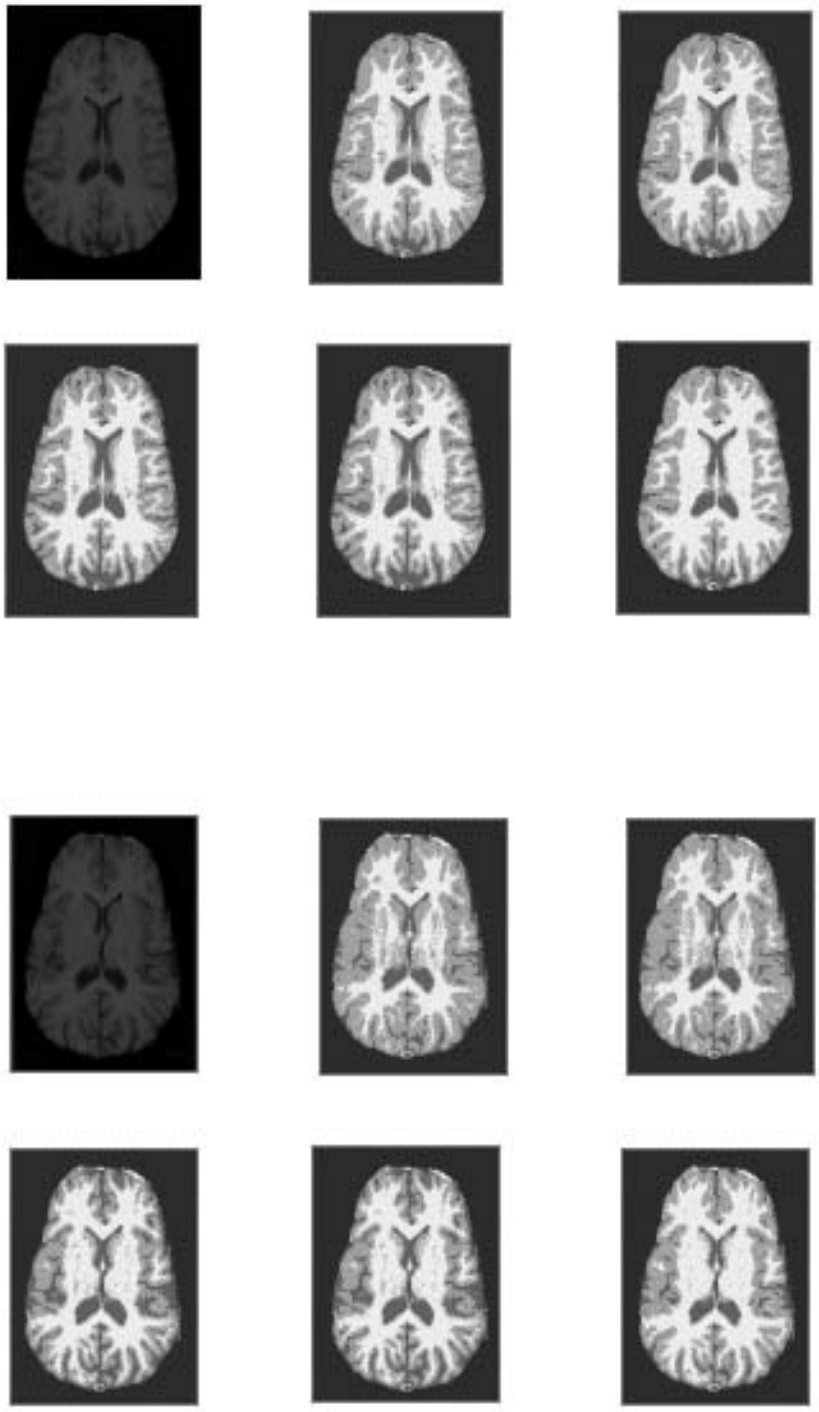

Figure 5.33: Segmentation Results - images enhanced by WNM-1

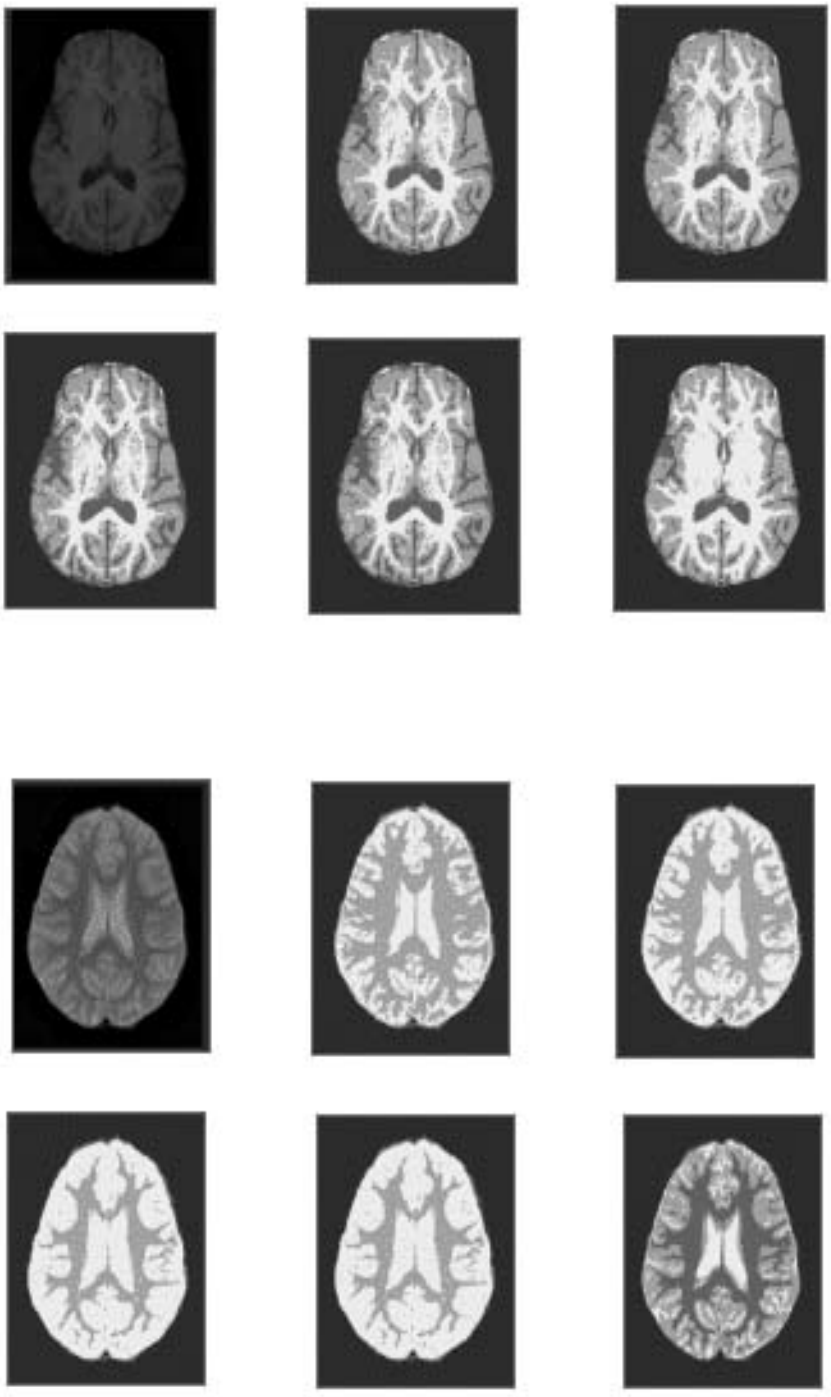

Figure 5.34: Segmentation Results - images enhanced by WNM-1

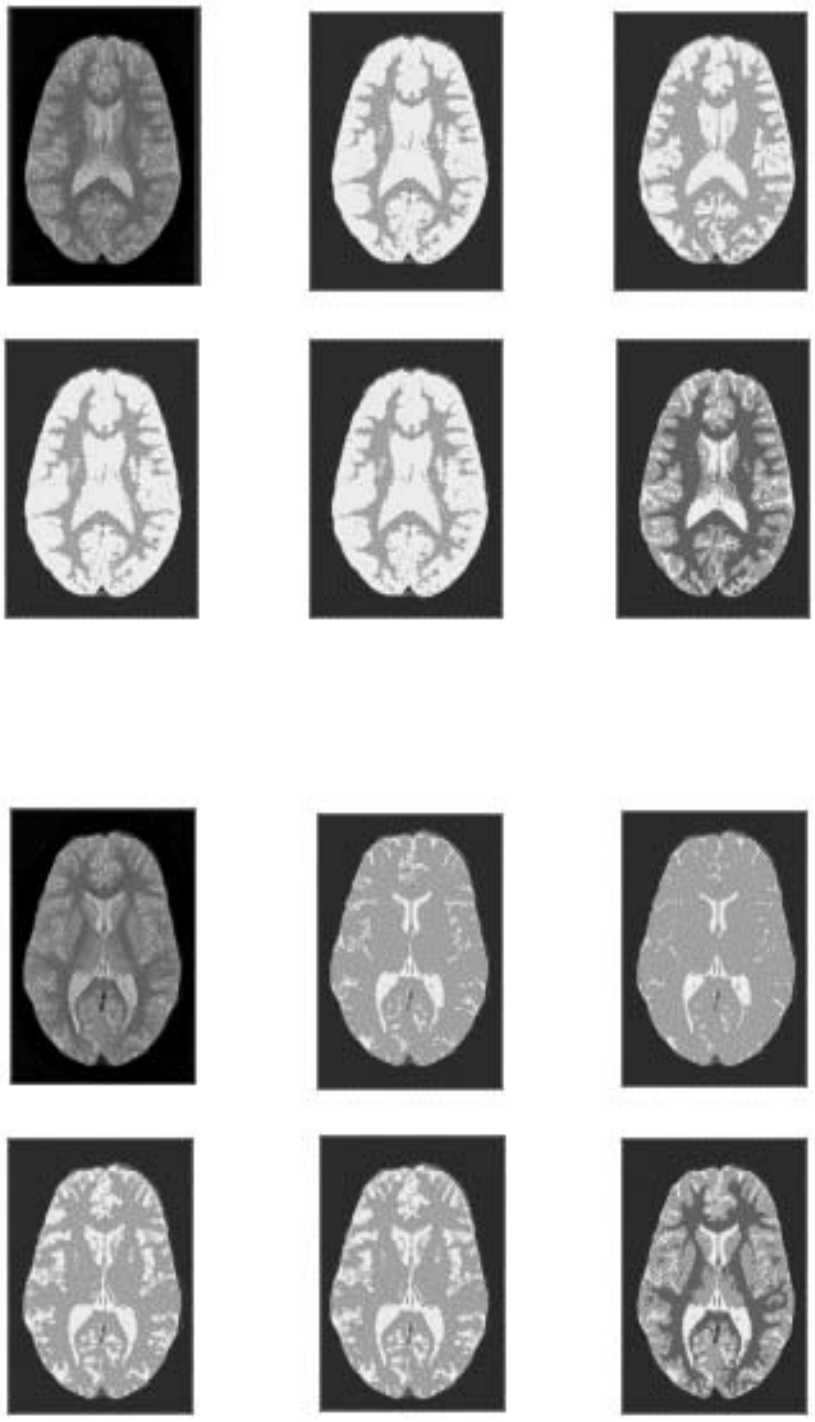

Figure 5.35: Segmentation Results - images enhanced by WNM-1

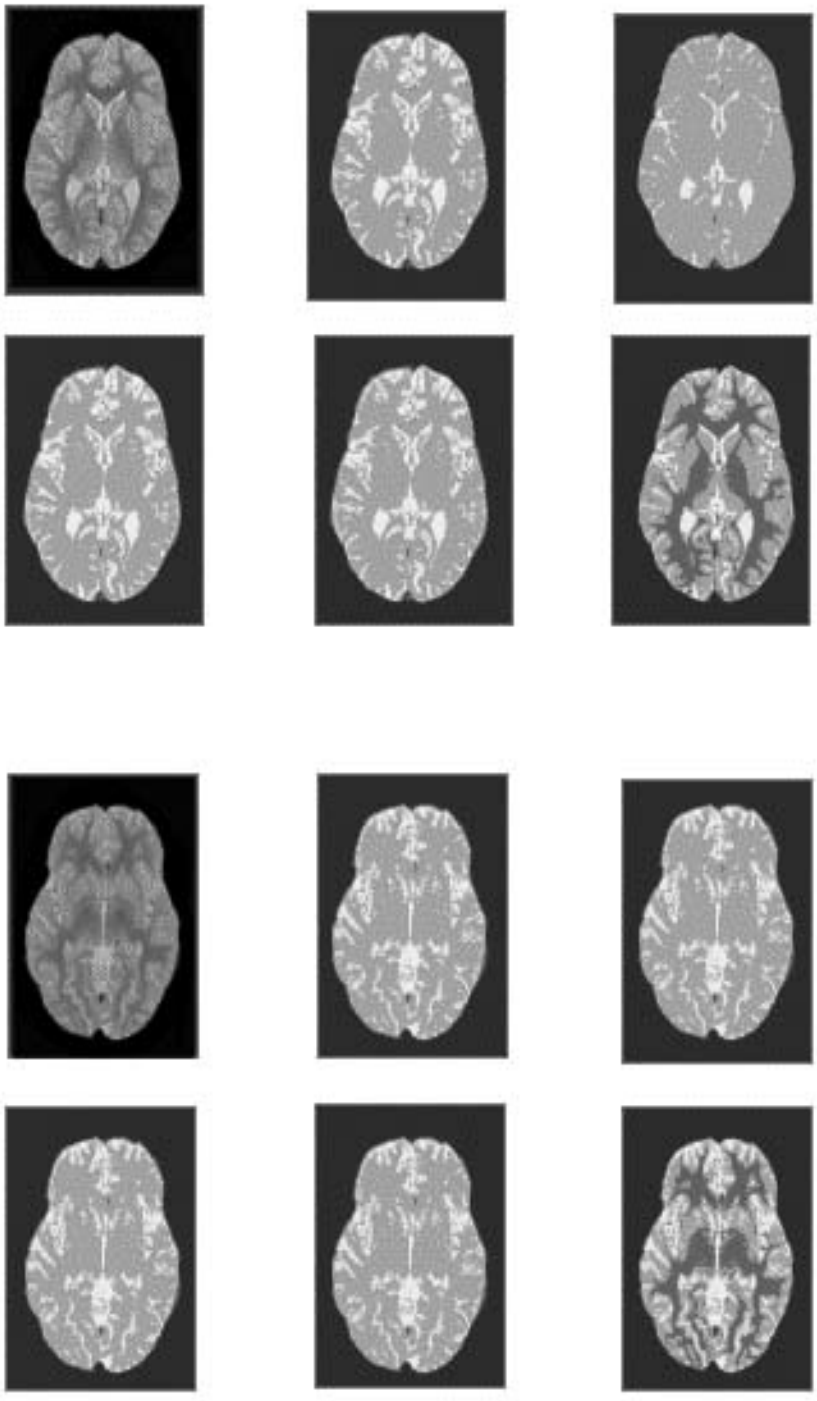

Figure 5.36: Segmentation Results - images enhanced by WNM-1

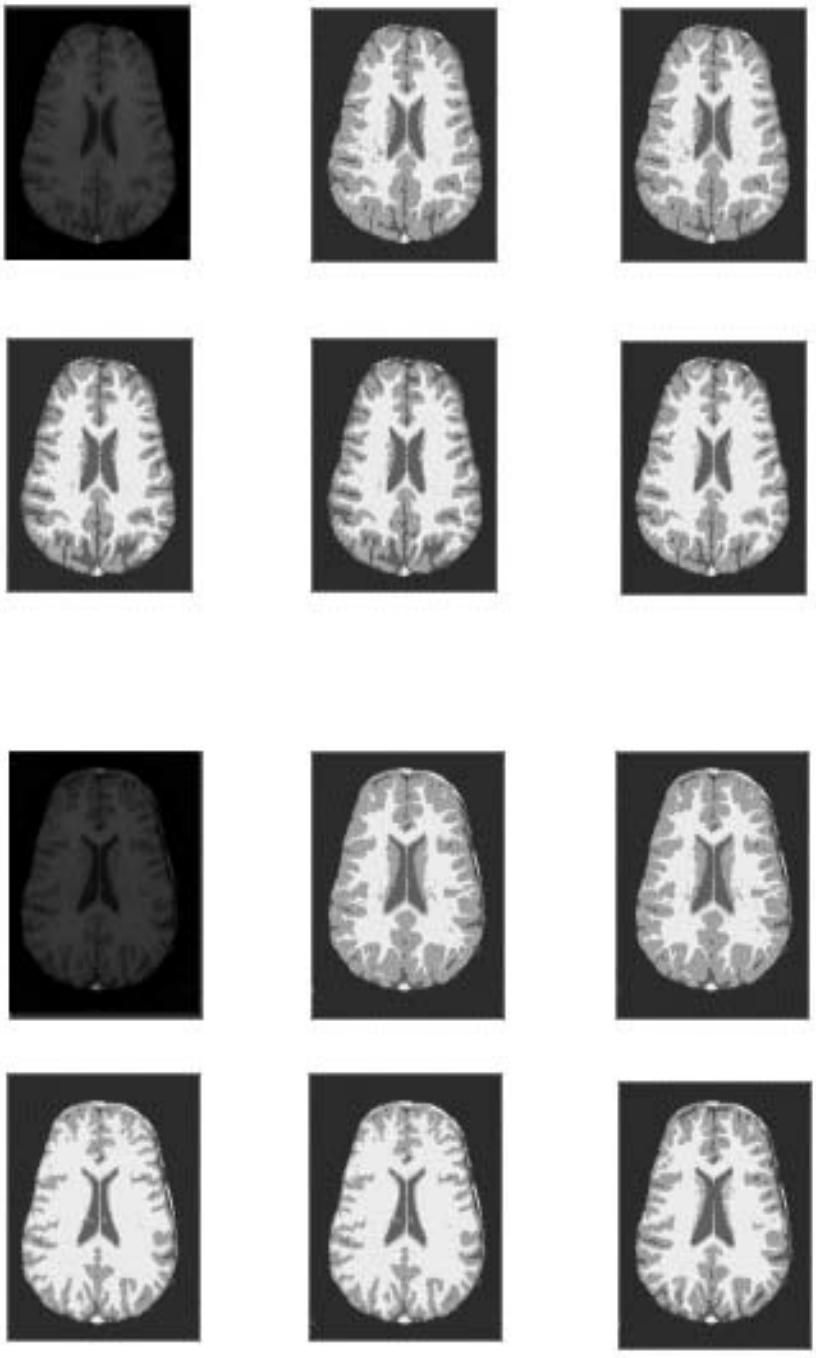

Figure 5.37: Segmentation Results - images enhanced by WNM-2

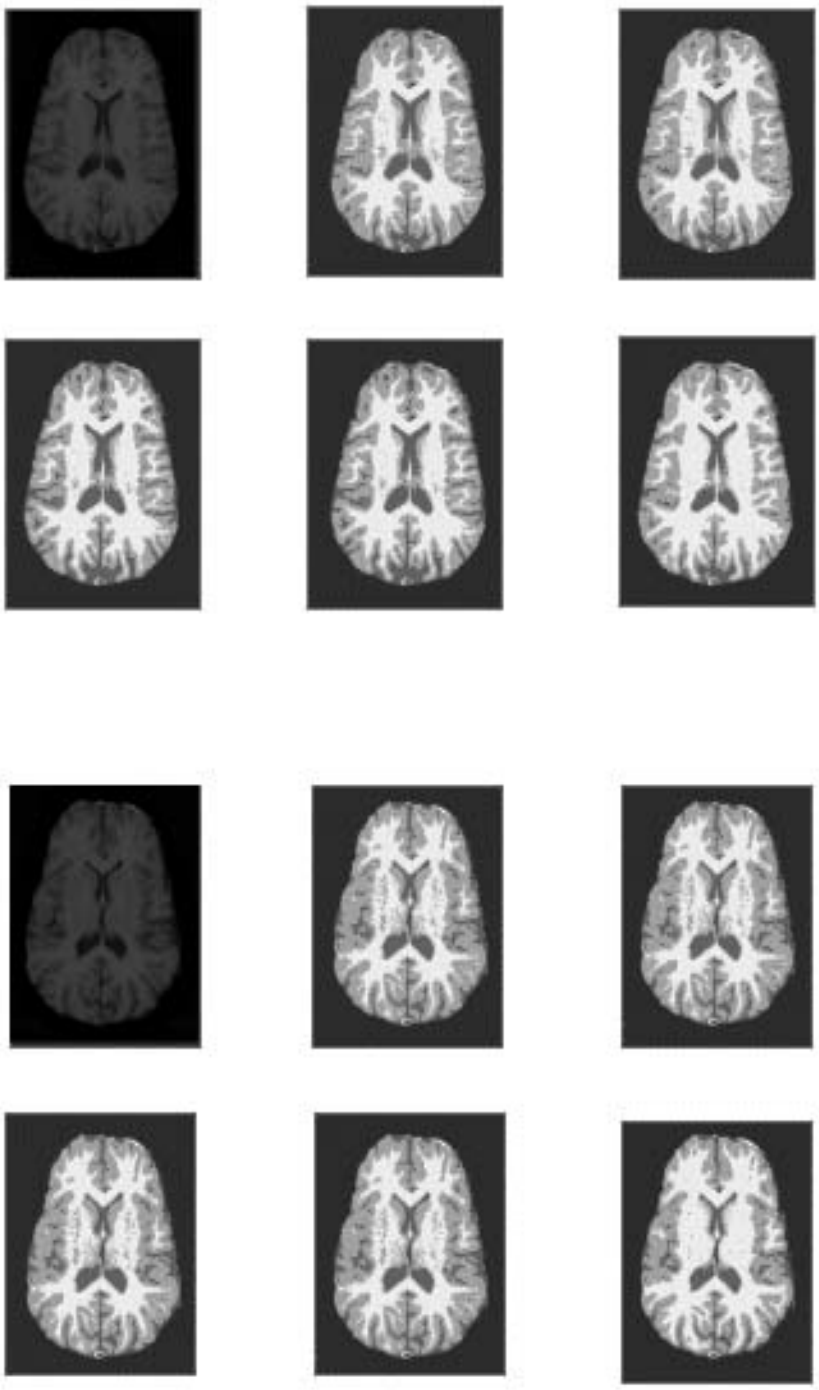

Figure 5.38: Segmentation Results - images enhanced by WNM-2

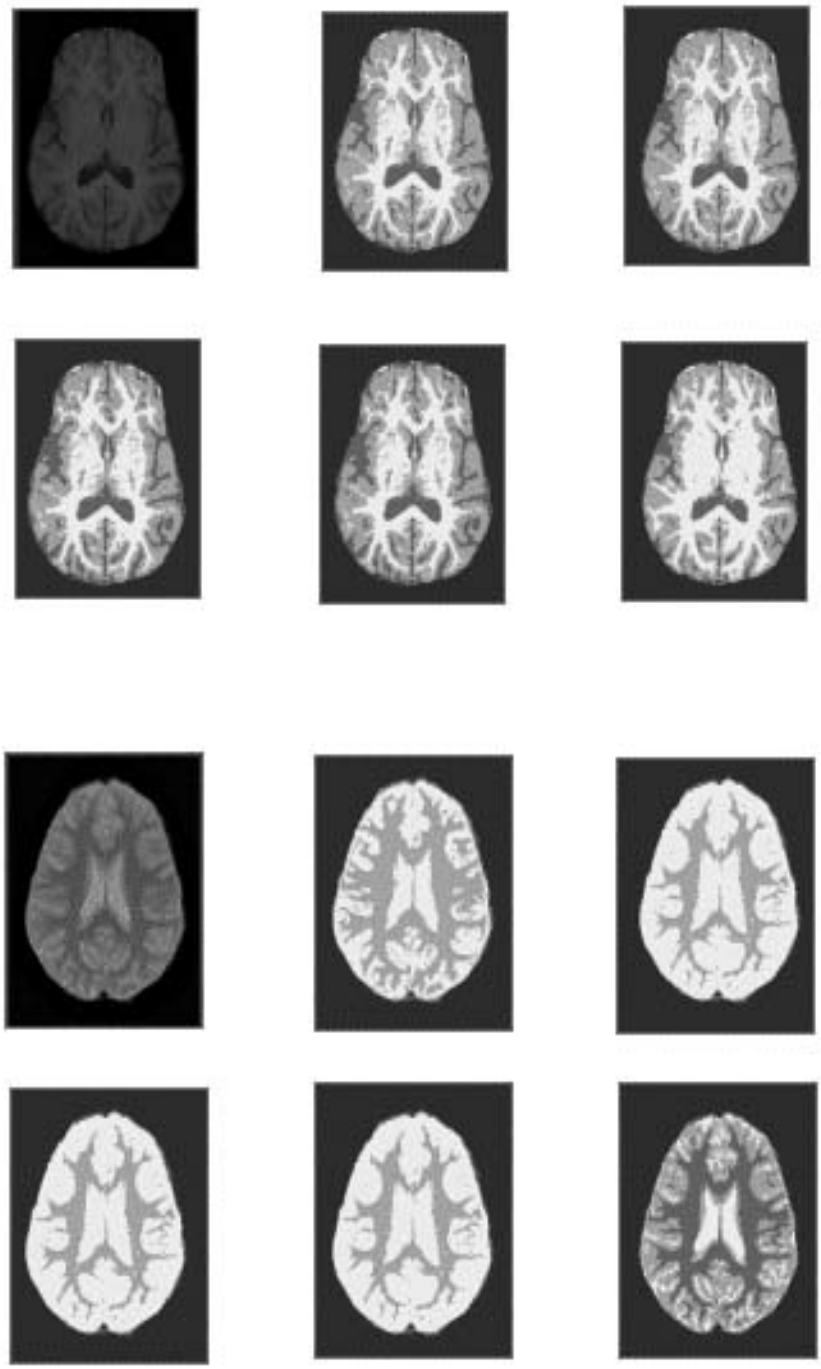

Figure 5.39: Segmentation Results - images enhanced by WNM-2

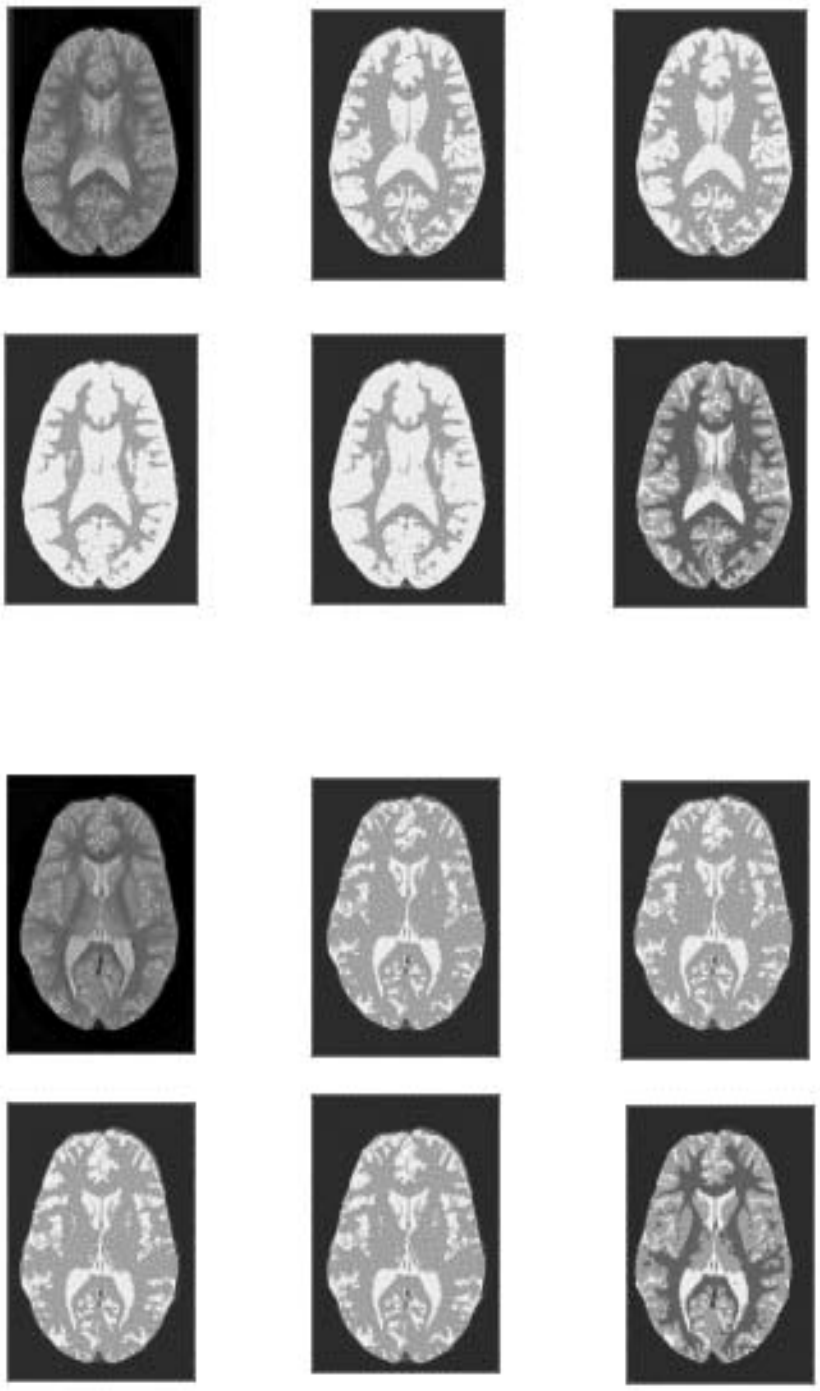

Figure 5.40: Segmentation Results - images enhanced by WNM-2

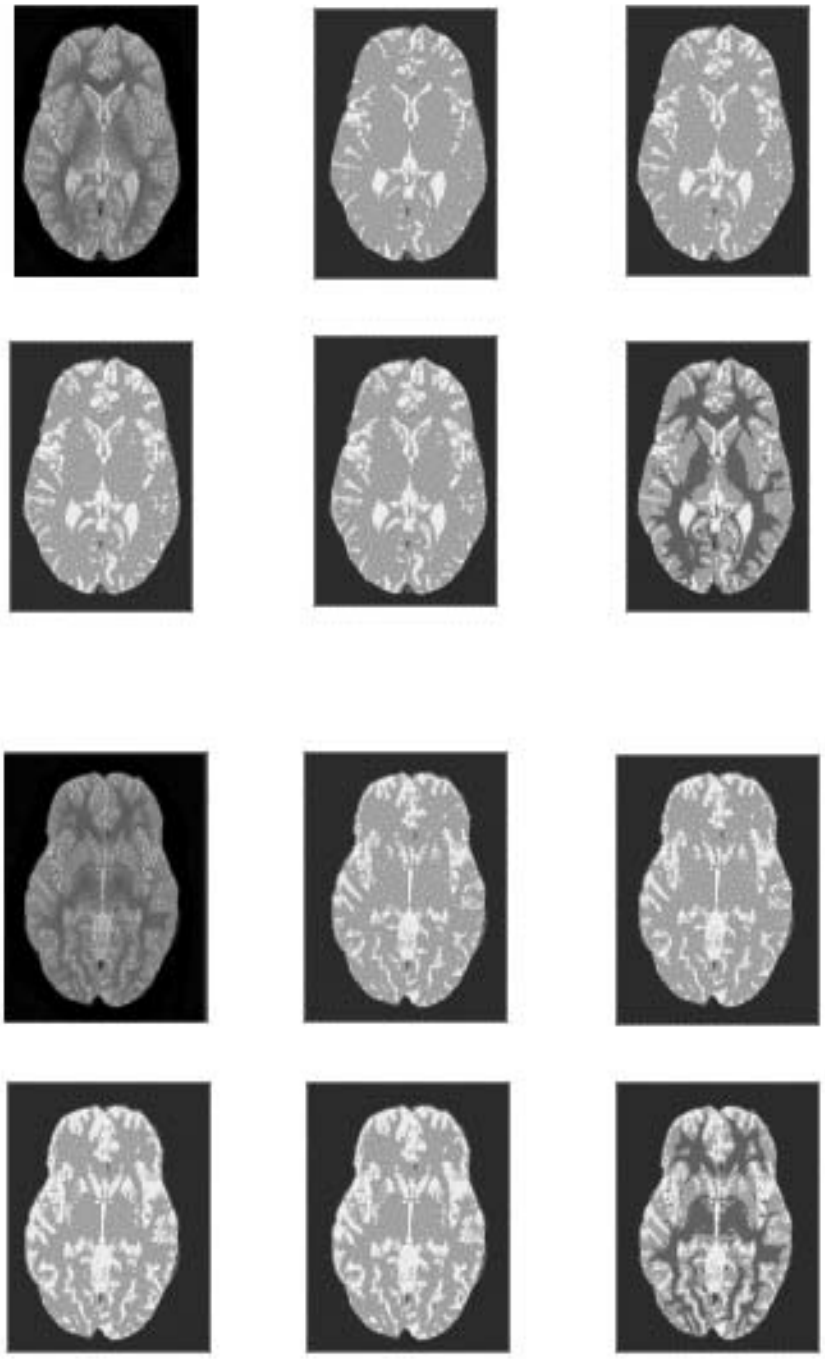

Figure 5.41: Segmentation Results - images enhanced by WNM-2

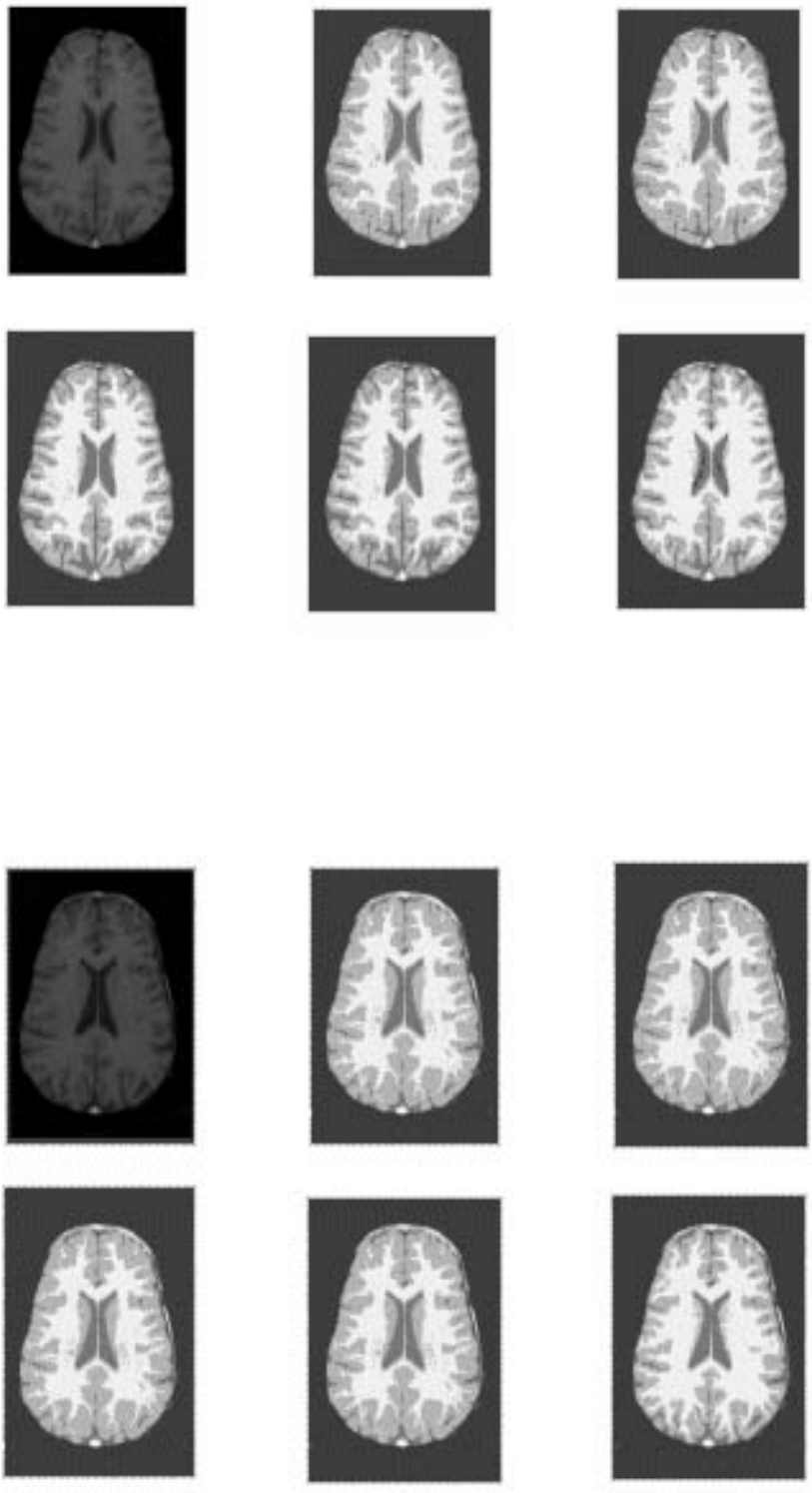

Figure 5.42: Segmentation Results - images enhanced by polynomial method

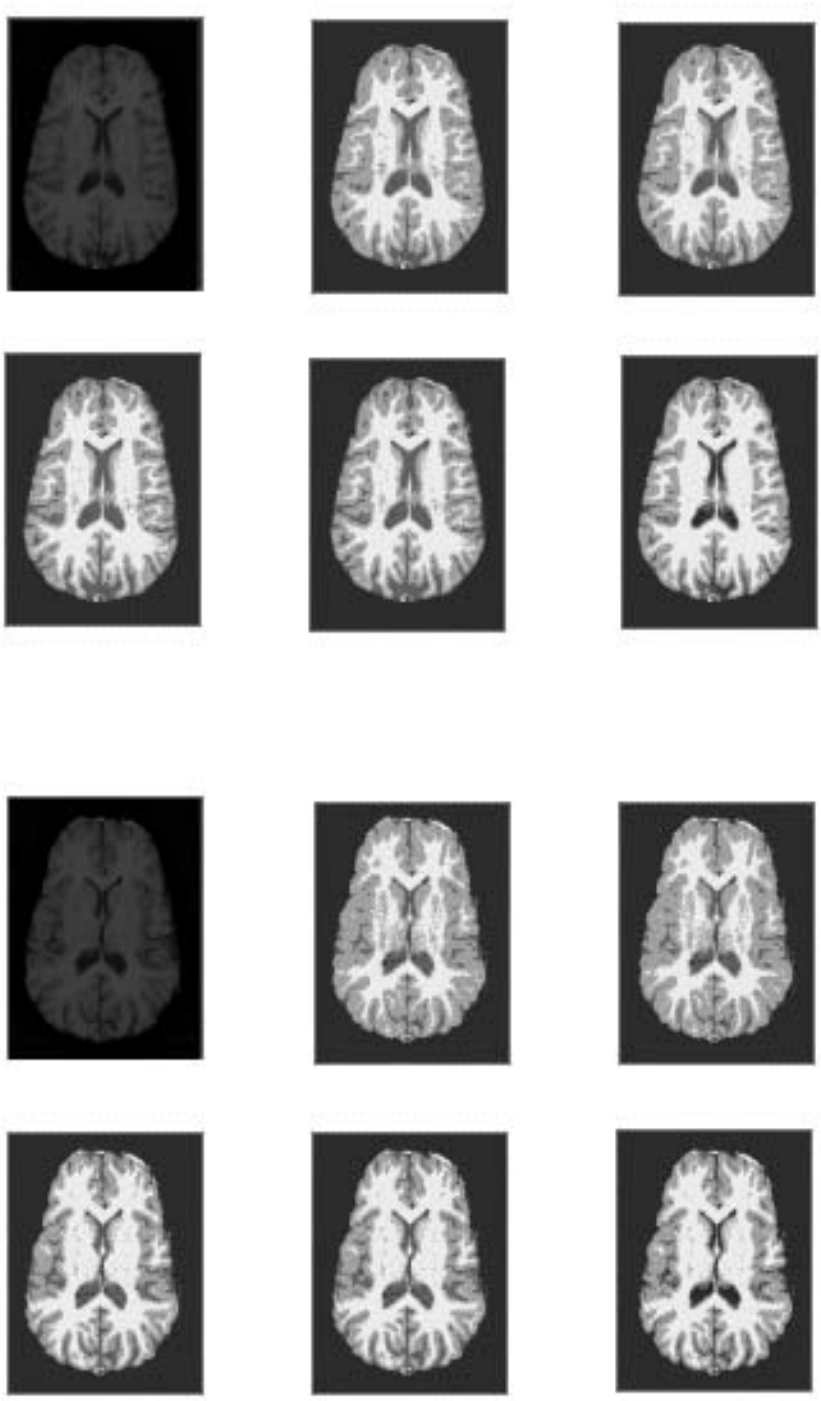

Figure 5.43: Segmentation Results - images enhanced by polynomial method

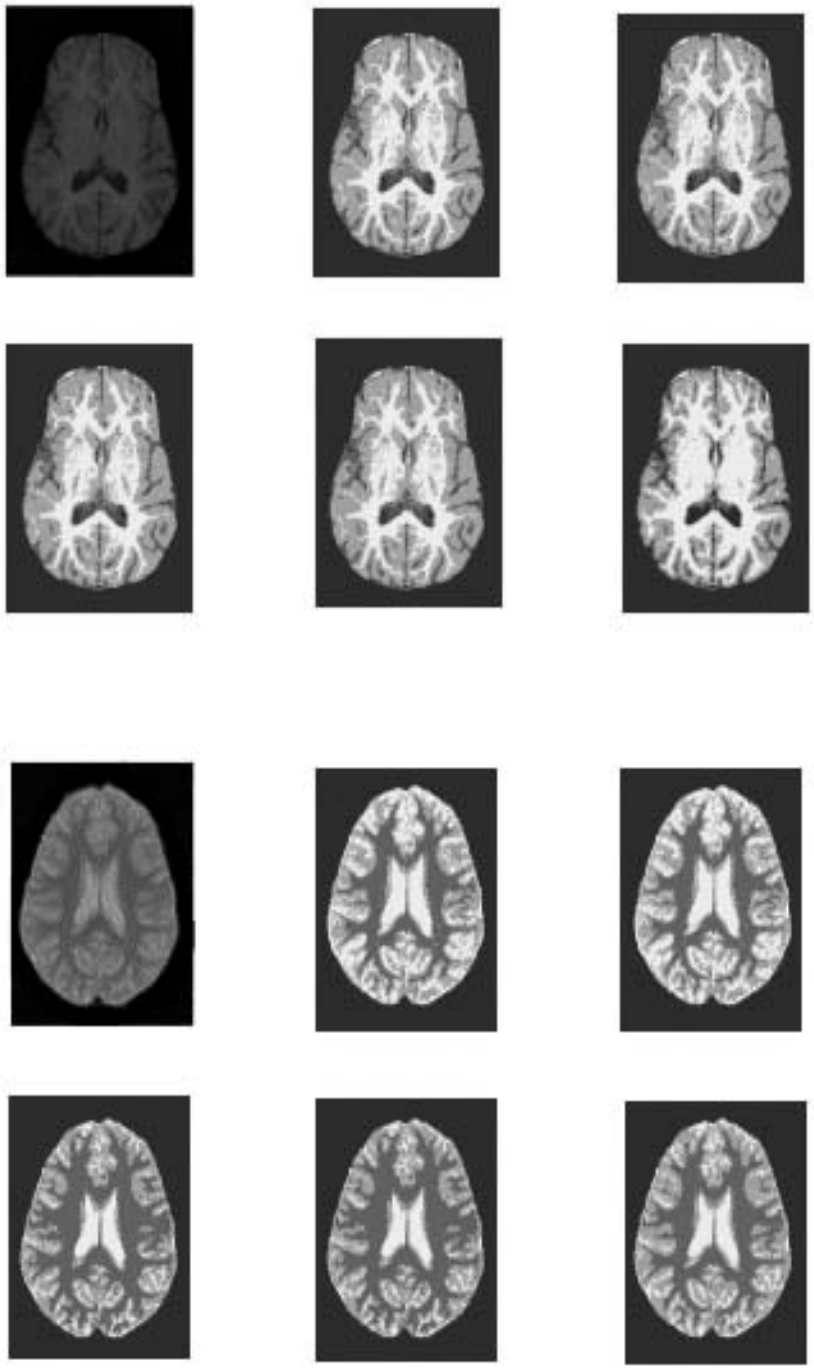

Figure 5.44: Segmentation Results - images enhanced by polynomial method

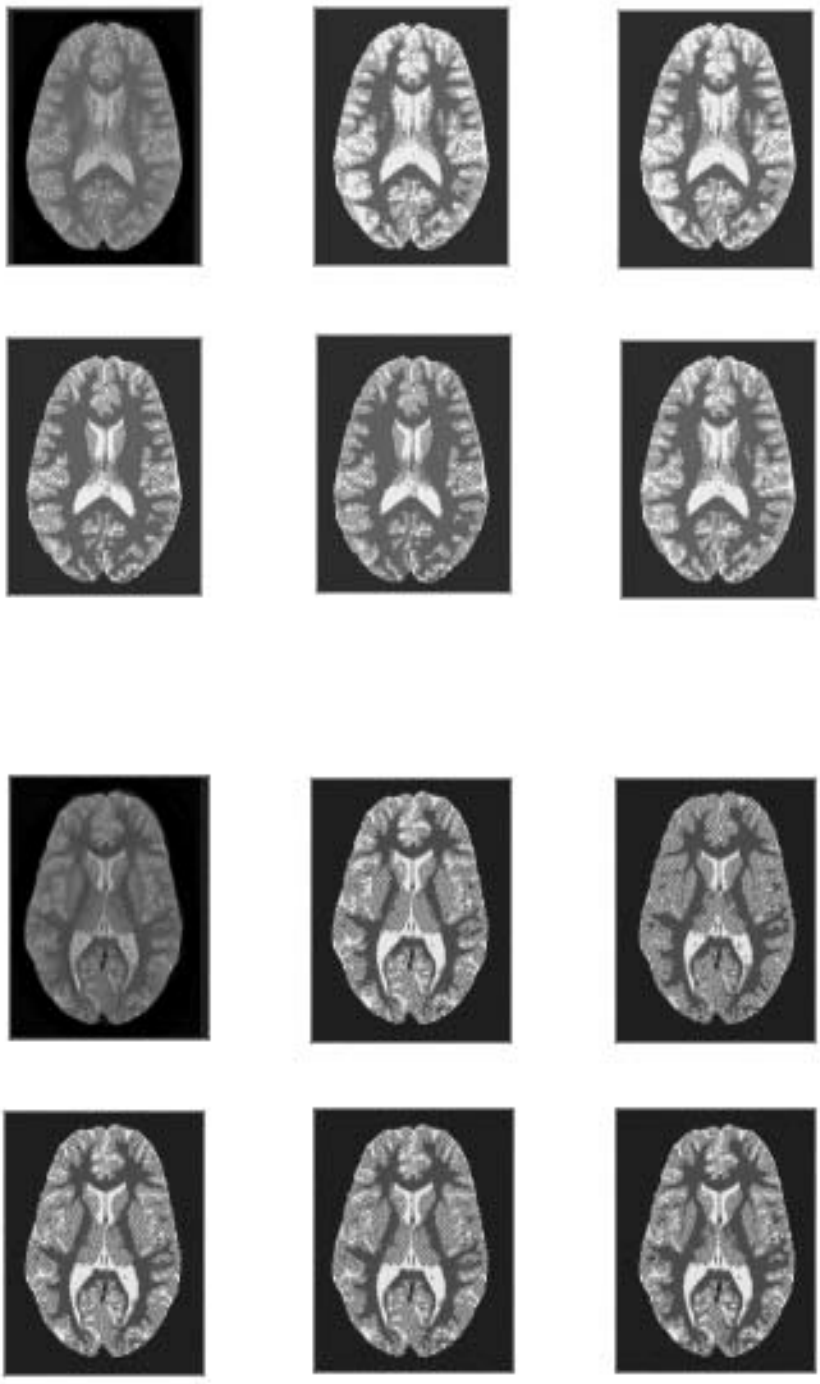

Figure 5.45: Segmentation Results - images enhanced by polynomial method

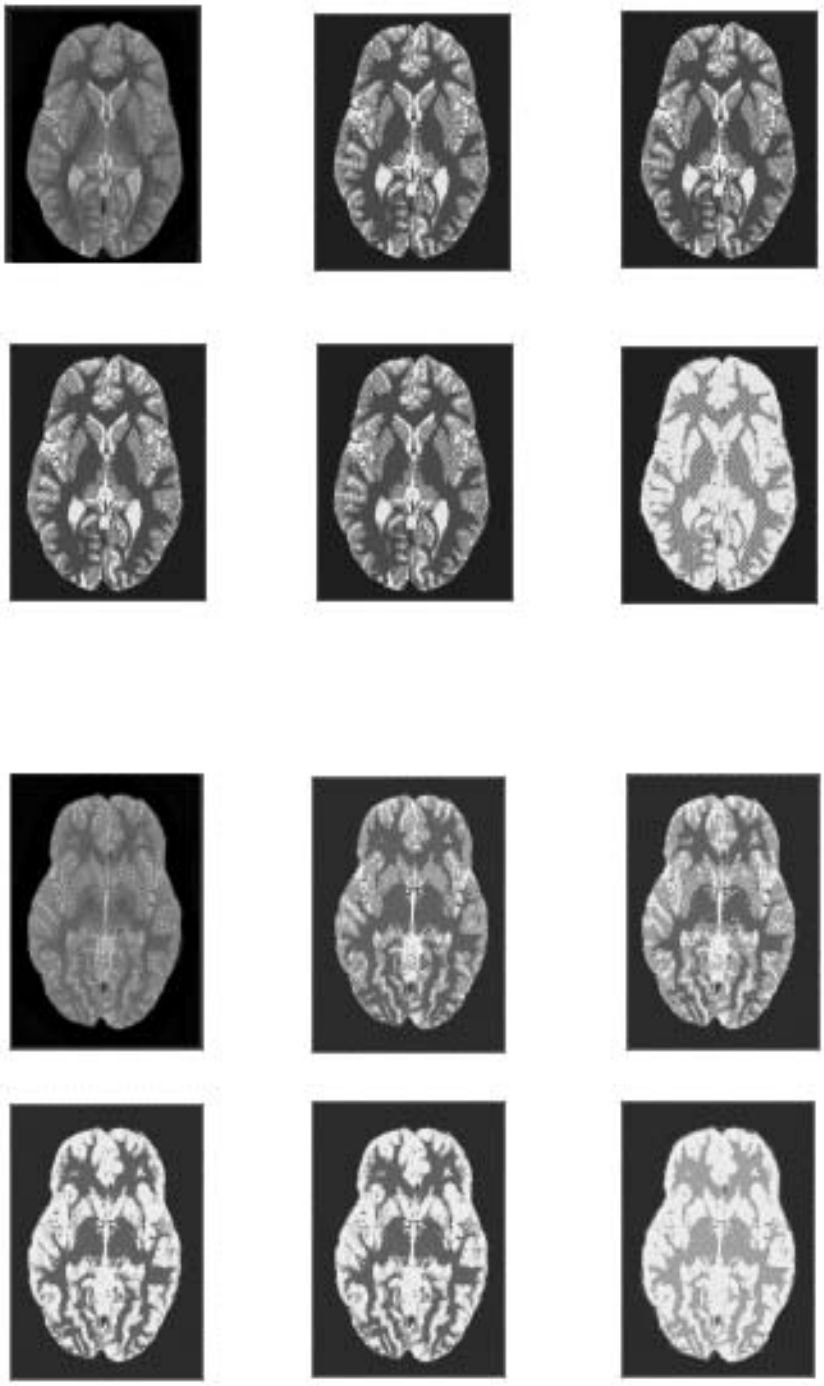

Figure 5.46: Segmentation Results - images enhanced by polynomial method

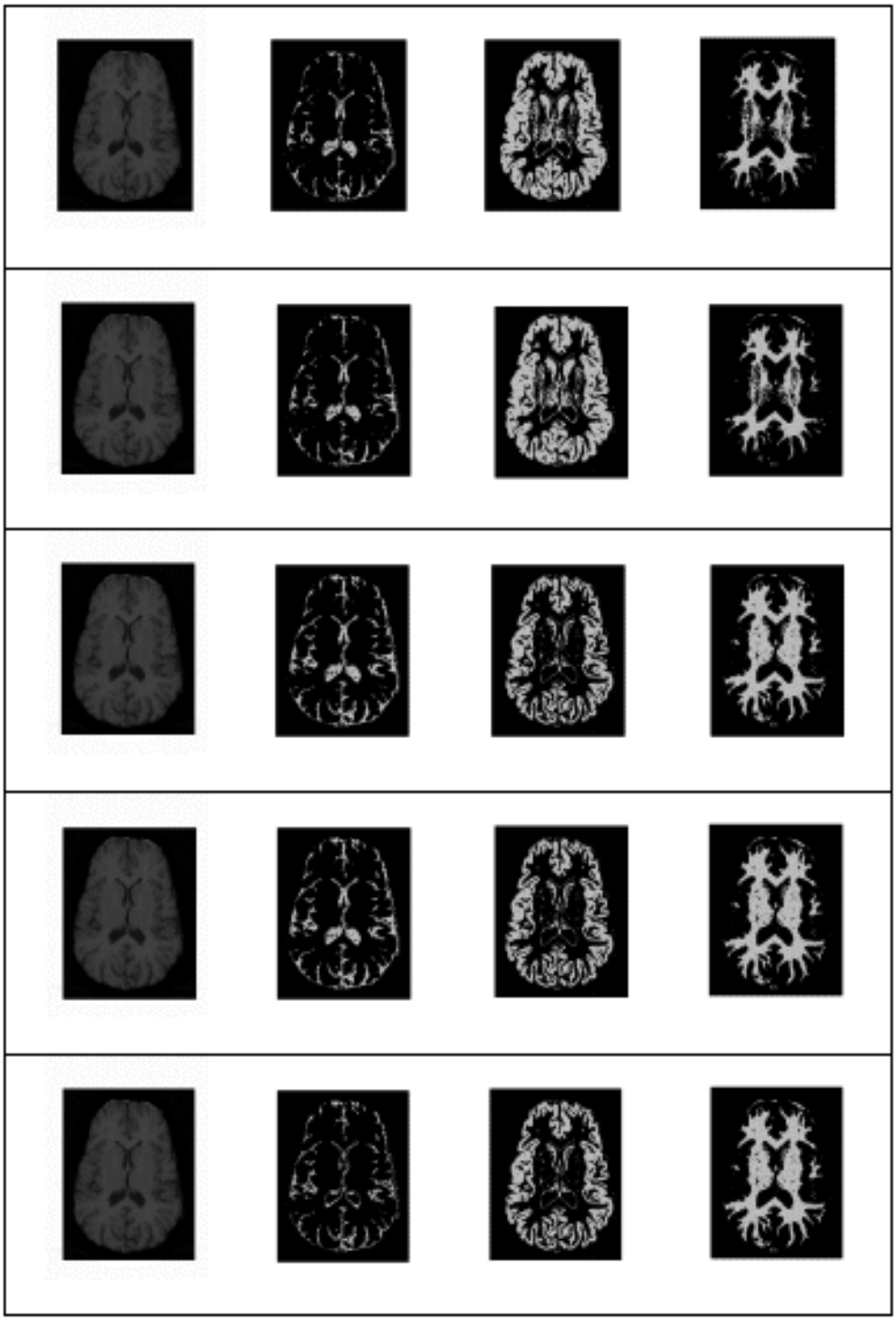

Figure 5.47: Segmentation Results - T1 image by different segmentation methods

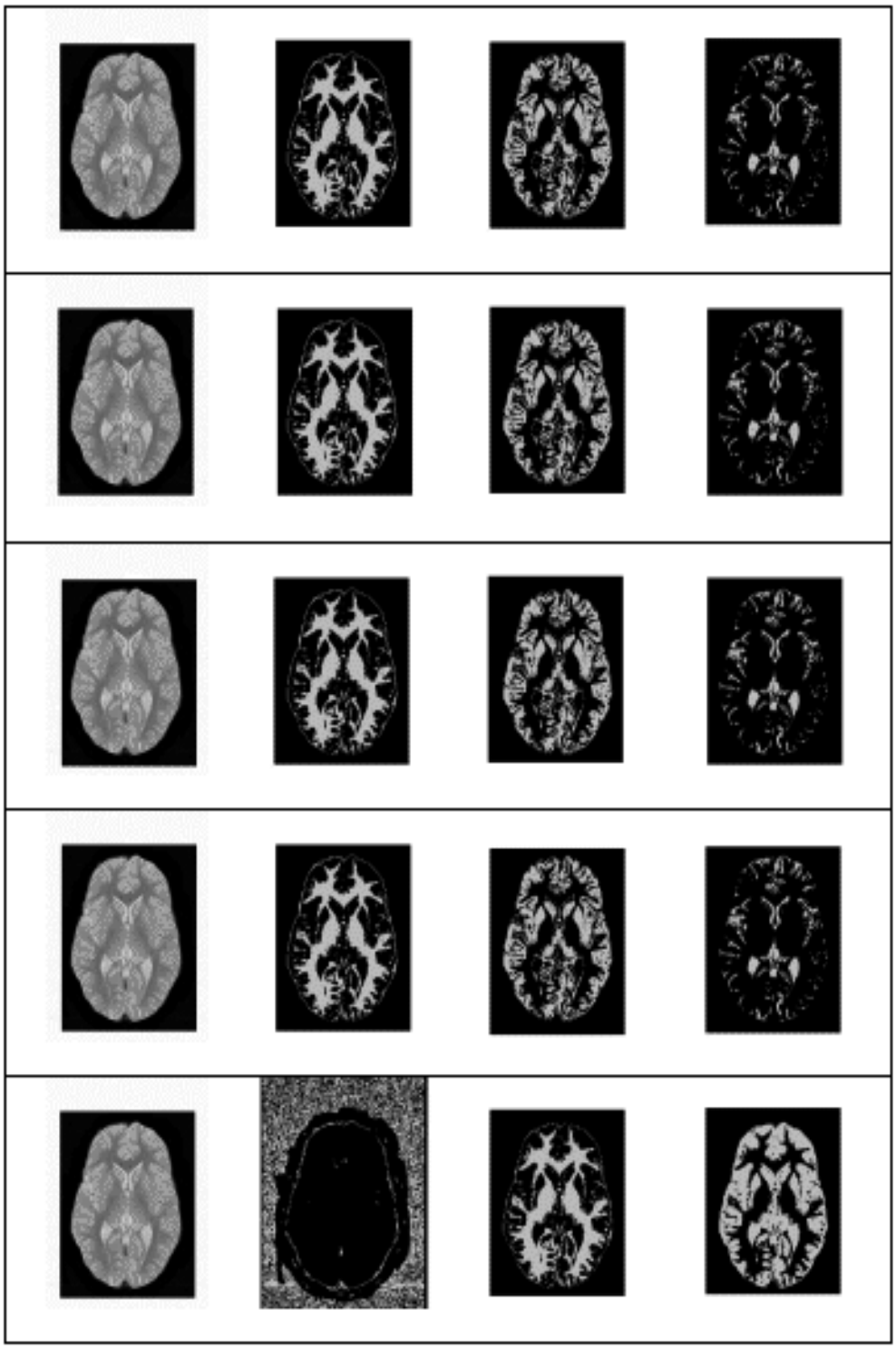

Figure 5.48: Segmentation Results - T2 image by different segmentation methods

Chapter 6

Conclusions

Results of work done on two different medical applications of image processing have been reported. One of the applications is the analysis and prediction of fetal pulmonary maturity and the other is the enhancement and segmentation of MR images. Both of these are expected to facilitate improved diagnosis.

Prediction of fetal lung maturity is a topic of considerable interest and has been extensively researched. Many investigators have used the mean echogenicity as a possible index for analyzing the pulmonary maturity. A large number of studies have been carried out in an attempt to establish a relation between the gestation age and the biochemical components present in the amniotic fluid. We have proposed a novel way of investigating fetal lung maturity using textural features of the sonogram and the results show considerable promise.

Data were collected from different Asian races (Indians, Malayans and Chinese) at intervals of 2 weeks from the gestation age of 24 to 38 weeks at Mediscan Systems, Chennai, India and University of Malaya Hospital, Kuala Lumpur, Malaysia. Data collection involved over 350 subjects and continued for a period of over one and a half years. Various textural features were extracted from the data set and the features relevant for characterizing lung maturity have been identified. Data collection from different races, and at two geographical locations in the world was carried out to test the robustness of the extracted features across the population. The features showed similar trend among the different

races studied. The subjects were thoroughly followed during and after the pregnancy. Our primary motivation was to find features that correlate with gestation age among the normals. Hence, only the data from subjects who had normal pregnancies and deliveries leading to babies with no pulmonary risk were included in our study.

To our knowledge, this is the first ever study that studied the textural features for assessing the pulmonary risk of fetus. The results have potential applications in neonatology in assessing the risk involved in premature delivery in otherwise normal pregnancies, and in facilitating the judicious use of steroid in such cases. Further, the erstwhile gold standard of L/S ratio is no longer held absolutely reliable and has not been used in most centers in India for the past 5 years. If further studies, on fetus with pulmonary immaturity and also normals, lead to results consistent with our study, then this method has the potential to become a new standard involving non-invasive ultrasound, thus eliminating the need for the invasive amniocentesis.

In the second application, elegant techniques have been proposed for the enhancement of real life MR images of both normal and pathological brain. The proposed nonlinear techniques are point, neighbourhood and polynomial based global methods. The enhancement schemes have been tested on more than 150 normal images and several images of patients. Evaluation of the results of enhancement has been conducted by neuroradiologists trained in MR image analysis. The evaluators have found the polynomial method to be the most suitable enhancement technique for MR images of both normal subjects and patients.

Segmentation of original and enhanced images have been carried out using GMM and its variants involving initialization using various clustering techniques. Convergence of the EM algorithm was faster in the case of k-means, VQ and FCM based initializations than for random initialization, without resulting in significant differences in the segmentation thresholds. The segmentation results of both T1- and T2-weighted images by GMM and all its variants tested are comparable in the case of polynomial enhanced images. The effectiveness of the polynomial based enhancement as a preprocessing tool for segmentation by GMM has been proved by testing on normal images, and several images from

patients. In comparison to FCM based segmentation, our proposed modifications to the GMM performed better on the enhanced images.

It is significant that the polynomial based enhancement method can adapt to the characteristics of images with good or bad initial contrast and always leads to better contrast images. The absence of the need for user tuning of the parameters to obtain good enhancement, makes this method viable to be considered as an addition to the standard repertoire of techniques available in any MRI system. Images enhanced by this method also led to better segmentation using the GMM based approaches, thus further improving its utility.

6.1 Significant Contributions of the Thesis

- To our knowledge, this work is the first ever exploration of sonographic textural features from a multi-racial, multi-locale data, for predicting fetal lung maturity.
- Our observations of the variation of lung echogenicity with the gestation age correlates well with earlier studies.
- Analysis of a large number of textural features, and selection of effective features through studies of correlation with gestation age. The consistency of the results by several classifiers indicate the validity of the set of features selected for pulmonary maturity analysis.
- Collection and analysis of a huge amount of controlled multi-racial, multi-locale data (over 350 subjects and from the gestation age of 24 to 38 weeks), which confirms the applicability of the results to a wide population.
- Possibility of our proposed method becoming a new, non-invasive standard, replacing the invasive amniocentesis for the assessment of pulmonary risk.
- Proposing three different methods of enhancing MR images and showing the polynomial based method as the most effective for images from both normal subjects and patients, based on evaluation by experts.

- Polynomial method obviates the need for user selection of parameters, while performing well on both T1- and T2- weighted images from normal and pathological brain.
- The enhancement methods have potential for other imaging modalities too.
- Validity of the proposed methods tested by evaluating on more than 150 images obtained from sections at different depths from more than 40 subjects.
- Employing polynomial enhancement as a preprocessing for segmentation, leading to very good results.
- Based on the results obtained, both of the medical groups collaborating with us have decided to incorporate our techniques in their clinical practice on a regular basis. After an initial period of further evaluation on patients, they would be put to clinical use on a day to day basis.

6.2 Scope for Future Work

- Further investigation combining ultrasound with biochemical tests will help to establish the validity of the method and eliminate the use of invasive tests for fetal pulmonary maturity analysis.
- In the case of MR image segmentation, since the polynomial based enhancement has enabled simple segmentation techniques to perform well, it is meaningful to explore its effectiveness with more sophisticated techniques of segmentation.
- The segmentation can be formulated as a constrained optimization problem by imposing constraints on the GMM parameters based on the knowledge of the gray level distribution of the three different tissues.
- Our studies based on GMM can be extended to the case of patients with specific abnormalities of the brain by suitably modifying the tissue model used in the study.
- The work can be extended to 3-D volumetric studies by studying the distribution of the three types of tissues in contiguous slices.

Bibliography

[1] M. Ashtari, J.L. Zito, B.I. Gold, J.A. Lieberman, M.T. Borenstein, and P.G. Herman. Computerized volume measurement of brain structure. *Investigative Radiology*, 25(7):798–805, July 1990.

[2] A. M. Bensaid, L. O. Hall, J. C. Bezdek, and L. P. Clarke. Fuzzy cluster validity in magnetic resonance images. *Proceedings of SPIE*, 2167:454–464, 1994.

[3] D M Benson and L D Waldroup. Ultrasonic tissue characterization of fetal lung, liver and placenta for the purpose of assessing fetal maturity. *J. Ultrasound in Medicine*, 2:489–494, 1983.

[4] J. C. Bezdek. Review of mri image segmentation techniques using pattern recognition. *Medical Physics*, 20:1033–1048, 1993.

[5] J. A. Bittoun. A computer algorithm for the simulation of any nuclear magnetic resonance imaging method. *Journal of Magnetic Resonance Imaging*, 2:113–120, 1984.

[6] M. Bomans, K. H. Hohne, U. Tiede, and M. Riemer. 3 - d segmentation of mr images of the head for 3-d display. *IEEE Transaction on Medical Imaging*, 9:177–183, 1990.

[7] C. A. Bouman. A multiscale random field model for bayesian image segmentation. *IEEE Transactions on Image Processing*, 3:162–176, 1994.

[8] W. G. Bradley, W. T. C. Yuh, and G. M. Bydder. Use of mtr imaging contrast agents in the brain. *Journal of Magnetic Resonance Imaging*, 3:199 –232, 1993.

[9] M. E. Brandt, T. P. Bohan, L. A. Kramer, and J. M. Fletcher. Estimation of csf, white and gray matter volumes in hydrocephalic children using fuzzy clustering of mr images. *Computerized Med. Imag. Graphics*, 18(1):25–34, 1994.

[10] J. C. Brinholz and E. E. Farrell. Fetal lung development : Compressibility as a measure of maturity. *Radiology*, 157(2):495 – 498, 1985.

[11] R. A. Bronen and G. Sze. Magnetic resonance imaging contrast agents: Theory and application to the central nervous system. *Journal of neurosurgery*, 73:820 – 839, 1990.

[12] M. E. Brummer and R. L. Eisner. Automatic detection of brain contours in mri data sets. *IEEE Transaction on Medical Imaging*, 12 (N2):152–166, 1993.

[13] Christopher J. C. Burges. A tutorial on support vector machines for pattern recognition. *Knowledge Discovery and Data Mining*, 2(2):1–43, 1998.

[14] P. L. Carson, C. R. Meyer, R. A. Bowerman, P. H. Bland, and F.L. Bookstein. Prediction of pulmonary maturity from ultrasound scattering, in tissue characterization with ultrasound. *CRC Press*, pages 169 – 187, 1986.

[15] P D Cayea, D C Grant, P M Doubilet, and T B Jones. Prediction of fetal lung maturity: inaccuracy of study using conventional ultrasound instruments. *Radiology*, 155:473–475, 1985.

[16] E L Charnock and C F Doershuk. Developmental aspects of the human lung. *Pediatr. Clin. North America*, 20:275–292, 1973.

[17] C. C. Chen, J. S. Daponte, and M. D. Fox. Fractal feature analysis and classification in medical imaging. *IEEE Trans. Med. Imaging*, 8:133–142, 1989.

[18] R. Christensen. Entropy minimax sourcebook. *Entropy Ltd.*, 1981.

[19] A. D. Christie. Determination of fetal lung development by ultrasound image analysis. *Technical Report - Dept. of Ultrasound (OB/GYN), Ninewells Hospital, Scotland.*, 1992.

[20] L. P. Clarke, R. P. Velthuizen, S. Phuphanich, J. D. Shellenberg, and J. A. Arrington. Stability of three supervised segnmentation techniques. *Magnetic Resonance Imaging*, 1:95–106, 1993.

[21] L. P. Clarke, R. P. Veltuizen, M. A. Camacho, J. J. Heine, M. Vaidyanathan, L. O. Hall, R. W. Thatcher, and M. L. Silbiger. Mri segmentation : Methods and applications. *Magnetic Resonance Imaging*, 13(3):343–368, 1995.

[22] H. E. Cline, W. E. Lorensen, S. P. Souza, F. A. Jolesz, R. Kikinis, G. Gerig, and T. E. Kennedy. 3d surface rendered mr images of the brain and its vasculature. *Computer Assisted Tomography*, 15:344–351, 1991.

[23] L. Cohen. On active contour models and balloons. *Computer Vision, Graphics and Image Processing*, 53:211–218, 1991.

[24] M.S. Cohen and R.M. Weisskoff. Ultra-fast imaging. *Magnetic Resonance Imaging*, 9(1):1–37, 1991.

[25] R Collobert and S Bengio. On The convergence of SVMTorch, an Algorithm for Large Scale Regression Problems. Technical report, Dalle Molle Institute for Perceptual Artificial Intelligence, Martigny, Switzerland, 2000.

[26] R W. Conners and C A. Harlow. A theoretical comparison of texture algorithms. *IEEE transaction on Pattern Analysis and Machine Intelligence*, 2(3):204–222, 1980.

[27] C. Diane Crawford, W. David Fenton, and W. Price, Islwyn. Ultrasonic tissue characterization of the placenta : Is it of clinical value ? *Journal of Clinical Ultrasound*, 13:533 – 537, 1985.

[28] C. Davatzikos and R. N. Bryan. Using a deformable surface model to obtain a shape representation of hte cortex. *Technical Report, John Hopkins University, Baltimore*, 1996.

[29] B. M. Dawant, M. Ozkan, A. Zijdenbos, and R. Margolin. A computer environment for 2d and 3d quantitation of mr images using neural networks. *Proceedings of the 13th IEEE Engineering in Medicine and Biology Society*, 13:64–65, 1991.

[30] S. Dellepiane. Image segmentation : Errors, sensitivity and uncertainity. *Proceedings of the 13th IEEE Engineering in Medicine and Biology Society*, 13:253– 254, 1991.

[31] A. P. Dempster. Maximum likelihood from incomplete data via the em algorithm. *Journal of the Royal Statistic Society*, Series B 39:1–38, 1977.

[32] RO Duda and PE Hart. *Pattern classification and Scene analysis*. John Wiley and Sons, 1973.

[33] S.A. Dudani. The distance- weighted k-nearest neighbor rule. *IEEE transactions on Systems Man and Cybernetics*, 6(4):325–327, April 1976.

[34] S. James Duncan and Nicholas Ayache. Medical image analysis: Progress over two decades and the challenges ahead. *IEEE transaction on Pattern Analysis and Machine Intelligence*, 22(1):85–106, 2000.

[35] Michael Feingold, James Scollins, Curtis CetrulO, and Doglas Koza. Fetal lung to liver reflectivity ratio and lung maturity. *J. Clinical Ultrasound*, 15:384 – 387, 1987.

[36] A. M. Fried, F. K. Loh, M. A. Umer, K. P. Dillon, and R. Kryscio. Echogenicity of fetal lung : relation to fetal age and maturity. *American Journal of Roentgenol*, 145(3):591–594, 1985.

[37] K.S. Fu and J.K. Mui. A survey on image segmentation. *Pattern Recognition*, 13:3–16, 1981.

[38] B. S. Garra, M. F. Insana, T. H. Shawker, R. F. Wagner, M. Bradford, and M. Russell. Quantitative ultrasonic detection and classification of diffuse liver disease : comparison with human observer performance. *Invest. Radiology*, 24:196 –203, 1989.

[39] W J. Garrett, P S. Warren, and R H. Picker. Maturation of the fetal lung, liver and bowel. *Radiology*, 155:473–475, 1985.

[40] G. Gerig, J. Martin, R. Kikinis, O. Kubler, M. Shenton, and F. A. Jolesz. Unsupervised tissue type segmentation of 3d dual-echo mr head data. *Image Vision Computing*, 10:349–360, 1992.

[41] L Gluck and M V. Kulovich. Fetal lung development : current concepts. *Pediatr. Clin. North Am.*, 20:275–292, 1973.

[42] R. Gonzalez. *Digital Image Processing.* Addison-Wesley, Reading, MA, 2nd edition, 1987.

[43] R. Guillemaud and M. Brady. Estimating the bias field of mr images. *IEEE Transaction on Medical Imaging*, 16:238–251, 1997.

[44] U. Haberkon, I. Zuna, A. Lorenz, H. Zerban, G. Layer, G. van, Kaick, and U. Raeth. Echographic tissue characterization inb diffuse parenchymal liver disease : Correlation of image structure with histology. *Ultrasonic Imaging*, 12:155–170, 1990.

[45] A. M. Hall, L. O. Bensaid, L. P. Clarke, R. P. Velthuizen, M. S. Silbiger, and J. C. Bezdek. A comparison of neural netrwork and fuzzy clustering techniques in segmenting magnetic resonance images of the brain. *IEEE Trans. Neural Networks*, 3(5):672–682, 1992.

[46] R M Haralick. Statistical and structural approaches to texture. In *Proc. of IEEE*, volume 67(5), pages 304–322, 1979.

[47] G. J. Harris, P. E. Barta, L. W. Peng, S. Lee, P. D. Brettschneider, A. Shah, J. D. Henderer, T. E. Schlaepfer, and G. D. Pearison. Mr volume segmentation of gray matter and white matter using manual thresholding : Dependence on image brightness. *Amer. J. Neuroradiol.*, 15:225–230, 1994.

[48] M. H. Hassoun. *Fundamental of Artificial Neural Networks.* MIT, Cambridge, MA, 1995.

[49] Simon Haykin. *Neural Networks : A Comprehensive Foundation.* Prentice Hall, 1999.

[50] R. E. Hendrick and E. M. Haacke. Basic physics of mr contrast agents in the brain. *Journal of Magnetic Resonance Imaging*, 3:137–156, 1993.

[51] H. J. Huisman and J. M. Thjssen. Adaptive texture feature extraction with application to ultrasonic image analysis. *Ultrasonic Imaging*, 20:132–148, 1998.

[52] M. F. Insana, R. F. Wagner, B. S. Garra, D. G. Brown, and T. H. Shawker. Analysis of ultrasound image texture via generalized rician statistics. *Optical Engineering*, 25(6):743–748, 1986.

[53] C. R. Jack, M. D. Bentley, C. K. Twomey, and A. R. Zinsmeister. Mr imaging-based volume measurement of the hippocampal formation and anterior temporal lobe. *Radiology*, 176:205–209, 1990.

[54] E. F. Jackson, P. A. Narayana, J. S. Wolinksy, and T. J. Doyle. Accuracy and reproducibility in volumetric analysis of multiple sclerosis lesions. *Journal of Computer Assisted Tomography*, 17:200–205, 1993.

[55] N. Karssemeijer. A statistical method for automatic labeling of tissues in medical images. *Machine Vision and Applications*, 3:75–86, 1990.

[56] D. Kazakos and P. Kazakos Papantoni. *Detection and Estimation*. Computer Science Press, New York, 1990.

[57] D. N. Kennedy, P. A. Filipek, and V. S. Caviness. Anatomic segmentation and volumetric calculations in nuclear magnetic resonance imaging. *IEEE Transaction on Medical Imaging*, 8(1):1–7, 1989.

[58] M. I. Kohn, N. K. Tanna, G. T. Herman, S. M. Resnick, P. D. Mozley, R. E. Gur, A. Alavi, R. A. Zimmerman, and R. C. Gur. Analysis of brain and cerebrospinal fluid volume with mr imaging : Part1.methods, reilability and validation. *Radiology*, 178:115–122, 1991.

[59] L. Kreel. Medical imaging. *Postgraduate Medical Journal*, 67:334–36, 1991.

[60] K I Laws'. Texture energy measures. In *Proc. of Image understanding Workshop*, volume 0, pages 47–51, 1979.

[61] S.U. Lee and S.Y. Chung. A comparative performance study of several global thresholding techniques for segmentation. *Computer Vision, Graphics and Image Processing*, 52:171–190, 1990.

[62] J. R. Liang, Z.and Macfall. Parameter estimation and tissue segmentation from multispectral mr images. *IEEE Transaction on Medical Imaging*, 13(N3):441–449, 1994.

[63] Z. Liang. Tissue classification and segmentation of mr images. *IEEE Engineering, Medicine and Biology*, 12:81–85, 1993.

[64] K. O. Lim and A. Pfefferbaum. Segmentation of mr brain images into cerebrospinal fluid spaces, white and gray matter. *J. Comput. Assist. Tomogr.*, 13(4):588–593, 1989.

[65] B. B. Mandelbrot. *The Fractal Geometry of Nature*. Freeman, New York, 1982.

[66] D. Marr and E. Hilderth. Theory of edge detection. *Proceedings of the Royal Society, London*, 207:187–217, 1980.

[67] G. J. McLachlan and K. E. Basford. *Mixture Models : Inference and Applications to Clustering*. Marcel Dekker Inc., New York, 1988.

[68] G. J. McLachlan and T. Krishnan. *The EM algorithm and extensions*. John Wiley and Sons, New York, 1996.

[69] J.R. Mittchell, S. J. Karlik, D. H. Lee, and A. Fenster. Computer - assisted identification and quantification of multiple sclerosis lesions in mr imaging volumes in the brain. *Journal of Magnetic Resonance Imaging*, 4:197 –208, 1994.

[70] G. Mittelhauber and F. Kruggel. Fast segmentation of brain magnetic resonance tomograms. *Conf. Comput. Vision, Virtual Reality and Robotics in Medicine*, pages 351–357, 1995.

[71] B. Karayiannis. Nicolaos and Pai Pin-I. Segmentation of magnetic resonance images using fuzzy algorithms for learning vector quantization. *IEEE Transaction on Medical Imaging*, 18(2):172–180, 1999.

[72] M. O' Donnel and W. A. Edelstein. Nmr imaging in the presence of magnetic field inhomogeneities and gradient field nonlinearities. *Medical Physics*, 12:20 –26, 1985.

[73] M. Ozkan and B. M. Dawant. Neural-network based segmentation of multi-modal medical images. *IEEE Transaction on Medical Imaging*, 12:534–544, 1993.

[74] E. Parzen. On estimation of a probability density function and mode. *Annals of Mathematical Statistics*, 33:1065–1076, 1962.

[75] T. Peli and D. Malah. A study of edge detection algorithms. *Computer Graphics and Image Processing*, 20:1–21, 1982.

[76] A. Pentland. Fractal- based description of natural scenes. *IEEE transaction on Pattern Analysis and Machine Intelligence*, 6:667–674, 1984.

[77] J. S. Peterson, J. O. Christoffersson, and K. Golman. Mri simulation using k-space formalism. *Magnetic Resonance Imaging*, 11:557–568, 1993.

[78] R. A. Petrucha, S. H. Golde, and L. D. Platt. Real time ultrasound of the placenta in assessment of fetal pulmonic maturity. *American Journal of Obstetrics and Gynecology*, 142(4):463–467, 1982.

[79] R A. Petrucha, S H. Golde, and L D. Platt. The use of ultrasound in the prediction of fetal pulmonary maturity. *Am. J. Obestetrics and Gynecology*, 144(8):931–934, 1982.

[80] W. E. Phillips, R. P. Velhuizen, J. Phuphanich, S.and Vilora, L. O. Hall, and M. L. Clarke, L. P. Silbiger. Application of fuzzy segmentation techniques for tissue differentiation in mr images of a hemorrhagic glioblastoma multiforme. *Magnetic Resonance Imaging*, 13:277–290, 1995.

[81] R. H. Picker. A scoring system of the morphological ultrasonic assessment of fetal well-being and maturation. In *Proc. 3rd World Federation of Ultrasound in Medicine and Biology*, page 597, Pergamon Press, Oxford, 1983.

[82] M. Podobnik, B. Brayer, and B Ciglar. Ultrasonic fetal and placenta tissue characterization and lung maturity. *Int. Jour. of Gynecology and Obstetrics*, 54:221–229, 1996.

[83] Hecht-Nielsen R. *Neurocomputing*. Addison-Wesley, MA, 1989.

[84] U. Raeth, D. Schlaps, B. Limberg, I. Zuna, A. Lorenz, G. van Kaick, W. J. Lorenz, and B. Kommerell. Diagnostic accuracy of computerised b -scan texture analysis and conventional ultasonography in diffuse parenchymal and malignant liver disease. *J. Clin. Ultras.*, 13:87 –99, 1985.

[85] C. Jagath Rajapakse, N. Jay Giedd, L., and Judith Rapoport. Statistical approach to segmentation of single-channel cerebral mr images. *IEEE Transaction on Medical Imaging*, 16(2):176 – 186, 1997.

[86] R. A. Redner and H. F. Walker. Mixture densities, maximum likelihood and the em algorithm. *SIAM Rev.*, 26(2):195–239, 1984.

[87] A. Renyi. On measures of entropy and information. *Proceedings of the 4th Berkeley Symposium on Mathematics, Statistics and Probability*, pages 547–561, 1960.

[88] Peter A. Rinck. *Magnetic Resonance in Medicine*. Blackwell Scientific Publications, London, 1993.

[89] G. X. Ritter, M. Shrader-Frechette, and J. N. Wilson. Image algebra : A rigorous and translucent way of expressing all image processing operations. *Proceedings SPIE Southeastern Technical Symposium on Optics, Electro-optics and Sensors*, Orlando, FL:116–121, 1987.

[90] G. X. Ritter and J. N. Wilson. *Handbook of Computer Vision Algorithms in Image Algebra*. CRC Press, Boca Raton, FL, 1996.

[91] P. K. Sahoo, S. Soltani, and K. C Wong. A survey of thresholding techniques. *Computer Vision, Graphics and Image Processing*, 41:233–260, 1988.

[92] P.K. Sahoo, S. Soltani, and K.C. Wong. A survey of thresholding techniques. *Computer Vision, Graphics, and Image Processing*, 41:233–360, 1988.

[93] Michael Seul, Lawerence O' Gorman, and Michael J. Sammon. *Practical Algorithms for Image Analysis : Description, Examples and Code*. Cambridge University Press, Cambridge, UK, 2000.

[94] C. E. Shannon. A mathematical theory of communications. *Bell System Technical Journal*, 27:370–423, 1948.

[95] C. E. Shannon and W. Weaver. A mathematical theory of communications. *The University of Illinois Press, Urbana*, 1962.

[96] C Sohn, W Stolz, A S. Gast, and G. Bastert. Ultrasound diagnosis of fetal lung maturity. *Zentralbl Geburtshilfe Perinatol*, 196(23):55–60, 1992.

[97] C Sohn, W Stolz, A S. Gast, and G. Bastert. Ultrasound diagnosis of fetal lung maturity. *Zentralbl Gynakol*, 117(3):138–143, 1995.

[98] C Sohn, W Stolz, A S. Gast, G. Bastert, and von Fournier D. Sonographic diagnosis of fetal lung maturity - a new method. *Zentralbl Gynakol*, 113(20):1114–1121, 1991.

[99] R. M. Summars, L. Axel, and S. Israel. A computer simulation of nuclear magnetic resonance. *Magnetic Resonance Imaging*, 3:363–376, 1986.

[100] Thieme, Meyer Johnson, Herron Silvers, Banjavic, and Carson. Sonographic identification of lung maturation in the fetal lamb. *Invest. Radiology*, 18:18 –26, 1983.

[101] W. Tsai. Moment-preserving thresholding: A new approach. *Computer Vision, Graphics and Image Processing*, 29:377–393, 1985.

[102] M. W. Vannier, T. K. Pilgram, C. M. Speidel, and L. R. Neumann. Validation of magnetic resonance imaging multispectral tissue classification. *Comput. Med. Imaging Graph*, 15:217–223, 1991.

[103] M. W. Vannier, C. M. Speidel, and D. L. Rickman. Magnetic reonance imaging multispectral tissue classification. *News Physiol. Sci.*, 3:148–154, 1988.

[104] V Vapnik. *The Nature of Statistical Learning Theory*. Springer, New York, 1995.

[105] R. P. Vellhuzien and L. P. Clarke. An interface for validation of mr image segmentations. *Proceedings of IEEE Engineering in Medicine and Biology Society*, 16:547–548, 1994.

[106] R. Voss. Random fractals : Characterization and measurement. *Scaling Phenomena in Disordered Systems*, New York, Plenum, 1986.

[107] R. F. Wagner, S. W. Smith, J. M. Sandrik, and H. Lopez. Statistics of speckle in ultrasound b -scans. *IEEE Trans. Sonics Ultras.*, 30:156–163, 1983.

[108] Y. Wang and T. Adali. Quantification and segmentation of brain tissues from mr images : A probabilistic neural network approach. *IEEE Trans. on Image Processing*, 7:1165–1180, 1998.

[109] W. M. Wells and W. E. L. Grimson. Adaptive segmentation of mri data. *IEEE Transaction on Medical Imaging*, 15:429–442, 1996.

[110] A. Witkin, M. Kass, and D. Terzopoulos. Snakes: Active contour models. *International Journal of Computer Vision*, 4:321–331, 1988.

[111] T.Y. Young and K.S. Fu. *Handbook of Pattern Recognition and Image Processing*. Academic Press, Inc., Orlando, FL, 1986.

[112] A. P. Zijdenbos, B. M. Dawant, and R. Margolin. Measurement reliablity and reproducibility in manual and semi-automatic mri segmentation. *Proceedings of the IEEE Engineering in Medicine and Biology Society*, 15:162–163, 1993.

Publications

1. K. N. Bhanu Prakash, A. G. Ramakrishnan, and S. Suresh, " Can Sonogram Predict Fetal Lung Maturity ?", *Proc.* XVIII *Southern Biomedical Engg. Conf.*, Clemson, SC, May 21-23, 1999.

2. K. N. Bhanu Prakash, A. G. Ramakrishnan, S. Suresh and Teresa P Chow, " Fetal Lung Maturity Analysis using Sonogram Textural Features", *Proc. Symposium on BME and Nuclear Medicine*, Mumbai, Jan. 2000, pp., 155-161.

3. K. N. Bhanu Prakash, A. G. Ramakrishnan, S. Suresh and Teresa P Chow, " An Investigation into the Feasibilty of Fetal Lung Maturity Prediction using Statistical Textural Features", *Submitted* to *Ultrasonic Imaging* after first revision.

4. K. N. Bhanu Prakash, A. G. Ramakrishnan, S. Suresh and Teresa P Chow, " Fetal Lung Maturity Analysis using Ultrasound Image Features", *Submitted* to *IEEE Trans. on Information Technology in Biomedicine*, after first revision.

5. K. N. Bhanu Prakash and A. G. Ramakrishnan, " MR Image Enhancement by Nonlinear Techniques", *Communicated to NIPS-2001* to be held during Dec 3-8 2001 in Canada.